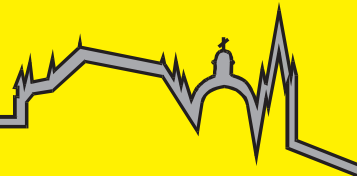


Marek Sebastian Simon

**On the Mechanism of Evaporation-
Determined Arc-Cathode Coupling in
GMA Welding**



Aachener Berichte Fügetechnik
Herausgeber: Prof. Dr.-Ing. U. Reisgen

Band 1/2021

Shaker Verlag

**“On the Mechanism of Evaporation-Determined Arc-
Cathode Coupling in GMA Welding”**

**„Über den Wirkzusammenhang der
Verdampfungsbestimmten Kopplung von Lichtbogen und
Kathode beim MSG-Schweißen“**

Von der Fakultät für Maschinenwesen der Rheinisch-Westfälischen Technischen
Hochschule Aachen zur Erlangung des akademischen Grades eines Doktors der
Naturwissenschaften genehmigte Dissertation

vorgelegt von
Marek Sebastian Simon


Berichter: Univ.-Prof. Dr.-Ing. Uwe Reisgen
Univ.-Prof. Dr.rer.nat. Dirk Uhrlandt

Tag der mündlichen Prüfung: 22.04.2021

Diese Dissertation ist auf den Internetseiten der Universitätsbibliothek online
verfügbar.

Marek Sebastian Simon

**On the Mechanism of Evaporation-
Determined Arc-Cathode Coupling
in GMA Welding**



Aachener Berichte Fügetechnik
Herausgeber: Prof. Dr.-Ing. U. Reisgen

Band 1/2021

Shaker Verlag

Bibliographic information published by the Deutsche Nationalbibliothek

The Deutsche Nationalbibliothek lists this publication in the Deutsche Nationalbibliografie; detailed bibliographic data are available in the Internet at <http://dnb.d-nb.de>.

Zugl.: D 82 (Diss. RWTH Aachen University, 2021)

Copyright Shaker Verlag 2021

All rights reserved. No part of this publication may be reproduced, stored in a retrieval system, or transmitted, in any form or by any means, electronic, mechanical, photocopying, recording or otherwise, without the prior permission of the publishers.

Printed in Germany.

ISBN 978-3-8440-8030-8

ISSN 0943-9358

Shaker Verlag GmbH • Am Langen Graben 15a • 52353 Düren

Phone: 0049/2421/99011-0 • Telefax: 0049/2421/99011-9

Internet: www.shaker.de • e-mail: info@shaker.de

Danksagung

Die vorliegende Arbeit entstand während meiner Tätigkeit als wissenschaftlicher Mitarbeiter am Institut für Schweißtechnik und Fügetechnik der Rheinisch-Westfälischen Technischen Hochschule Aachen mit finanzieller Unterstützung der Deutschen Forschungsgemeinschaft im Rahmen des SFB1120 „Präzision aus Schmelze“.

Zunächst möchte ich Gott danken, da ich durch die Kirche die Werte der Hingabe und der Ordnung gelernt habe, ohne die ich diese Arbeit nicht bewältigen hätte können.

Als nächstes gilt mein besonderer Dank dem Institutsleiter, Herrn Prof. Dr.-Ing. Uwe Reisgen, für seine Bereitschaft, mir die Möglichkeit zur Promotion gegeben zu haben, für die Betreuung meiner Arbeit, für das Vertrauen, das er in mich gesetzt hat und für die Ermutigung, die ich durch ihn erfahren habe. Herrn Prof. Dr.rer.nat. Dirk Uhrlandt danke ich für die sorgfältige Durchsicht der Arbeit, die Übernahme des Koreferates sowie seine ermutigende Beurteilung meiner Arbeit. Außerdem möchte ich auch Herrn Prof. Marek Behr (Ph.D.) für die Übernahme des Vorsitzes der Promotionskommission danken.

Als nächstes danke ich meinem Gruppenleiter Dr.-Ing. Oleg Mokrov sowie meinen beiden Oberingenieuren Dr.-Ing. Alexander Schiebahn und Herrn Rahul Sharma für ihr Vertrauen, sowie für ihre umsichtige Leitung meiner Arbeit und die vielen unschätzbar wertvollen Diskussionen, von denen ich maßgeblich profitiert habe.

Mein außerordentlicher Dank gilt Prof. Mikhail Benilov von der Universität von Madeira, für seinen Willen mich zu unterstützen und für seine Einladung zu einem Forschungsaufenthalt an die Universidade da Madeira.

Außerdem möchte ich mich bedanken bei meinen Kollegen vom SFB 1120 für die fruchtbare Arbeit in den Arbeitskreisen, sowie bei meinen Kollegen am ISF, insbesondere Dr.-Ing. Oleksii Lisnyi, Herrn Andre Schmidt, Herrn Philipp Lozano, Herrn Sobhan Emadmostoufi, Frau Gertrud Baumann sowie Dr.-Ing. Lars Stein, für ihre tatkräftige Unterstützung und Hilfsbereitschaft.

Zu guter Letzt gilt mein Dank meinen Freunden und meiner Familie, insbesondere meinen Eltern, Beata und Stefan Simon, sowie meiner Freundin Nazira Ibrahim für die Unterstützung und Liebe, die ich immer von ihnen erfahren habe.

Aachen im April 2021

Acknowledgements

This thesis was written during my work as scientific assistant at the Welding and Joining Institute at RWTH Aachen University with financial support of the German Research Foundation within the framework of the SFB1120 "Precision melt engineering".

First of all, I would like to thank God, because through the church I have learned the values of devotion and order, without which I would not have been able to accomplish this work.

My special thanks go to the head of the institute, Prof. Dr.-Ing. Uwe Reisgen, for his willingness to give me the opportunity to obtain a doctorate, and supervising of my work, for the trust he placed in me and his encouragement. I would like to thank Prof. Dr.rer.nat. Dirk Uhrlandt for the careful review of my work, for acting as assessor and for his encouraging evaluation. I would also like to thank Prof. Marek Behr (Ph.D.) for assuming the chairmanship of the doctoral committee.

Next, I would like to thank my group leader Dr.-Ing. Oleg Mokrov as well as my two head engineers Dr.-Ing. Alexander Schiebahn and Mr. Rahul Sharma for their trust, as well as for their prudent guidance of my work and many invaluable discussions from which I benefited significantly.

My sincere thanks go to Prof. Mikhail Benilov of the Universidade da Madeira for his willingness to support me in my research and his invitation to a research stay at the University of Madeira.

I would also like to thank my colleagues from SFB 1120 for the fruitful work in the working groups, as well as my colleagues at ISF, especially Dr.-Ing. Oleksii Lisnyi, Mr. Andre Schmidt, Mr. Philipp Lozano, Mr. Sobhan Emadmostoufi, Ms. Gertrud Baumann and Dr.-Ing. Lars Stein, for their active support and helpfulness.

Last but not least I would like to thank my friends and my family, especially my parents, Beata and Stefan Simon, as well as my girlfriend Nazira Ibrahim for the continuous support and overflowing love I have always received from them.

Aachen, April 2021

Excerpts from this work have already appeared in:

MOKROV, O., O. LYSNYI, M. SIMON, U. REISGEN, G. LASCHET, and M. APEL, 2017. Numerical investigation of droplet impact on the welding pool in gas metal arc welding [online]. *Materialwissenschaft und Werkstofftechnik*, **48**(12), 1206-1212. Available from: doi:10.1002/mawe.201700147

MOKROV, O., M. SIMON, R. SHARMA, and U. REISGEN, 2019. Arc-cathode attachment in GMA welding [online]. *Journal of Physics D: Applied Physics*, **52**(36), 364003. Available from: doi:10.1088/1361-6463/ab2bd9

MOKROV, O., M. SIMON, A. SCHIEBAHN und U. REISGEN, 2020. Concept for the calculation of the distribution of heat input in the cathode area by GMA welding [online]. *Welding in the World*, **34**(3), R103. Available from: doi:10.1007/s40194-020-00929-9

MOKROV, O., M. SIMON, R. SHARMA und U. REISGEN, 2020. Effects of evaporation-determined model of arc-cathode coupling on weld pool formation in GMAW process simulation [online]. *Welding in the World*, **64**(5), 847-856. Available from: doi:10.1007/s40194-020-00878-3

MOKROV, O., M. SIMON, P. LOZANO, D. ARNTZ-SCHROEDER, R. SHARMA und U. REISGEN, 2020. Simulation des Lichtbogenansatzes beim MSG-Schweißen. *DVS-Berichte, Band 365 : DVS Congress. Große Schweißtechnische Tagung. DVS CAMPUS. Vorträge der Online-Veranstaltungen vom 14. bis 18. September 2020.* pp. 700 - 706

I Content

I	Content.....	I
II	List of figures.....	V
III	List of tables	X
IV	List of abbreviations.....	XI
V	List of symbols.....	XIV
VI	Abstract	XXII
1	Introduction.....	1
1.1	Gas metal arc welding.....	1
1.2	The arc in GMAW.....	2
1.2.1	Plasma column.....	3
1.2.2	Plasma-electrode boundary layers.....	4
1.2.2.1	Anode layer	4
1.2.2.2	Cathode layer	5
2	State of the art.....	8
2.1	Substitution models used in GMAW process simulation	8
2.2	Cathode layer models derived from plasma physics	10
2.2.1	Models for arc-cathode coupling in diffuse arc attachment with a “hot cathode” at atmospheric pressure in inert gas:.....	10
2.2.1.1	PhD thesis of Kaddani. 1995	11
2.2.1.2	PhD thesis of Wendelstorf. 2000	12
2.2.1.3	PhD thesis by Cayla. 2008	14
2.2.1.4	PhD thesis by Shirvan. 2016	14
2.2.1.5	Benilov Marotta (1995) – „A model of the cathode region of atmospheric pressure arcs”	15
2.2.2	Models for cold cathodes	19

2.2.2.1 PhD thesis Coulombe (1997): Model for evaporating Cu, Fe, Ti cathodes	19
2.2.2.2 Models by Benilov (2015) and Almeida (2013) for vacuum arcs on evaporating Cr or CrCu cathodes.	24
2.2.2.3 Model of Benilov (1993) for “spot attachment” in vacuum arc for copper cathodes	28
2.3 Discussion	30
3 Statement of the problem and goals.....	33
3.1 Preliminary welding experiments (high speed video recordings).....	33
3.1.1 Welding experiments with helium.....	34
3.1.2 Welding experiments with Ar+8%CO ₂	37
3.2 Dialectic argument.....	40
3.2.1 Hypothesis 1: Ion flux due to evaporated atoms, ionized in the near-cathode plasma at constant temperature	42
3.2.1.1 Analysis	42
3.2.1.2 Conclusions	47
3.2.2 Hypothesis 2: Ion flux due to constant metal vapor density in the plasma	48
3.2.2.1 Analysis	48
3.2.2.2 Conclusions	53
3.2.3 Synthesis: proposal of core hypothesis	54
3.3 Conclusion	54
3.4 Goal of the work	55
3.4.1 Problem solving approach.....	55
4 Model description	56
4.1 Model for diffuse arc-cathode attachment	56
4.1.1 Theory of the model of the evaporation-determined arc cathode coupling (EDACC)	56

4.1.1.1 Heat fluxes.....	56
4.1.1.2 Electrical current densities.....	58
4.1.2 Results of the model for the evaporation-determined arc-cathode coupling	61
4.1.2.1 Composition of the heat flux and dominating mechanisms.....	61
4.1.2.2 Dependence of the heat flux and current density on $T_{plasma, bulk}$...	67
4.1.2.3 Dependence of the heat flux and current density on UD	68
4.2 Discussion.....	70
5 Results: Coupling of the EDACC model to the weld pool	72
5.1 Set up for numerical CFD experiments	72
5.1.1 The domain	73
5.1.2 The material	74
5.1.3 The boundaries	76
5.1.3.1 Inlet.....	76
5.1.3.2 Outlet.....	76
5.1.3.3 Top	76
5.1.3.4 Bottom	76
5.1.3.5 Wall.....	76
5.1.3.6 Droplets	77
5.1.3.7 Arc heat and current	77
5.1.3.8 Evaporation	77
5.2 Sensitivity analysis	78
5.2.1 Analysis of the surface temperature field	80
5.2.2 Analysis of the heat flux and current density distributions	83
5.2.3 Analysis of the current density vector fields on the melting isosurface and the electromagnetic force in the weld pool	87
5.2.4 Analysis of the velocity vector fields in the weld pool	91

5.3	Discussion	94
6	Conclusions and Outlook.....	95
7	References	103
A	Appendix: Model for evaporation by Knight (1979)	111

II List of figures

Abbildungsverzeichnis

Figure 1: Schematic of the Gas Metal Arc Welding process [MOK19].....	1
Figure 2: Example for stable voltage wire feed combinations in constant voltage GMA processes [REI15]	2
Figure 3: Calculated ratio of the flux of vaporized atoms to the flux of thermo-field emitted electrons as a function of the cathode surface temperature T_s for different cathode materials, from [COU97]	6
Figure 4: Schematic of the model for cathode region after Kaddani [KAD95].....	12
Figure 5: Schematic of the cathode layer as applied by Wendelstorf [WEN00]	13
Figure 6: Resulting heat flux from [BEN95]. Full curves, broken curves and dotted curves take into account different ionization states of argon.	17
Figure 7: Densities of energy flux, ion current, electron emission, back-diffused electrons, electron temperature, ionization degree ω , the ratio of the energies delivered by the plasma electrons and by the ions rei and the ratio of cooling/heating r_{ch} , for $U = 17V$, from [BEN95].	18
Figure 8: Schematic representation of the cathode region of an emitting cathode exposed to a high pressure arc, from [COU97]	19
Figure 9: Ratio of ion current density to the current density due to thermo-field emission, from [COU97]	21
Figure 10: Ratio of flux of vaporization and flux by thermo-field emission for copper in dependence of electron temperature and saturated vapor pressure from the heated cathode surface, from [COU97]	22
Figure 11: Heat flux to a copper cathode in an atmospheric arc cathode spot, from [COU97].....	23
Figure 12: Current density to a copper cathode in an atmospheric arc cathode spot from [COU97]	24

Figure 13: Ion saturation current for Cr-vapor plasma, $T_e = 8000[K]$, $j_i(d)$: diffusion approach, $j_i(f)$: multi-fluid approach; d : ionization length; λ_D : Debye-length; λ_{ia} : mean free path for collisions between ions and neutrals, from [BEN15].....	25
Figure 14: Schematic of the double sheath approach with ionisation of emitted atoms, from [BEN10]	26
Figure 15: Electric current density j for Cu (solid) and Cr (dashed), for different cathode layer voltages, from [ALM13].....	27
Figure 16: Heat flux from the plasma to the cathode q for Cu (solid) and Cr (dashed) cathode with different cathode layer voltages from [ALM13]	28
Figure 17: Heat flux as resulting for a copper cathode in a vacuum arc, in dependence of cathode layer voltage drop and inverse cathode surface temperature $T_w - 1$, from [BEN93]	29
Figure 18: Transient Current-Voltage recordings for helium shielding gas, with $v_{weld} = 60[cmmin]$. $U_{total, average} = 36[V]$, $I = 193[A]$	34
Figure 19: Identifiable cathode spots (marked with red circles on the right side) in helium, with $v_{weld} = 60[cmmin]$. Aperture 22; UV+ND4 Filter. No spectral filter. 30000fps. $1/30000[s]$ shutter time. [MOK20b]	35
Figure 20: a) calm and smooth weld pool surface in the case with spot attachment, see Figure 19. b) rough weld pool surface at weld pool attachment. Shielding gas: helium, with $v_{weld} = 60[cmmin]$. The arc is burning directly on the melt pool. Aperture 22; UV+ND4 Filter. 436nm spectral filter. 30000fps. $1/1000000[s]$ shutter time. [MOK20b]	36
Figure 21: Appearance of dry islands (marked in red on the right side) in helium with $v_{weld} = 90[cmmin]$, in the phase with "spot attachment". Aperture 22, UV+ND4 Filter. 436nm spectral filter. 30000fps. $1/1000000[s]$ shutter time.	37
Figure 22: Transient Current-Voltage recordings for argon+8%CO ₂ shielding gas, with $v_{weld} = 60[cmmin]$. $U_{total, average} = 28[V]$, $I_{total, average} = 197[A]$	38
Figure 23: Three consecutive moments of the weld pool in Ar+8%CO ₂ at $v_{weld} = 60[cmmin]$. No spots are identifiable, but only an extending "white zone" ahead of the melting front. Aperture 22, UV+ND2 Filter. No spectral filter. 30000fps. $1/1000000[s]$ shutter time. [MOK20b].....	39

Figure 24: Three consecutive close-ups of the "white zone" in Ar+8%CO ₂ at $v_{weld} = 60[cmmin]$. Spots are not identifiable. Aperture 22, UV+ND2 Filter. No spectral filter. 225000fps. $1/225000[s]$ shutter time. [MOK20b]	39
Figure 25: Current density due to field enhanced thermionic emission, with fixed ion current density j_{ion} for the Mackeown formula	41
Figure 26: Heat fluxes according to the assumption of full ionization of the evaporated atoms and their return to the cathode	42
Figure 27: Current density according to the assumption of full ionization of the evaporated atoms and their return to the cathode	43
Figure 28: Ionization degree for the assumption that evaporated iron atoms are ionized at $T_{plasma} = 7000[K]$	44
Figure 29: Heat flux to the cathode, assuming ionization of evaporated iron atoms in LTE at $T_{plasma} = 7000[K]$	45
Figure 30: Current density to the cathode, assuming ionization of evaporated iron atoms in LTE at $T_{plasma} = 7000[K]$	46
Figure 31: Hypothetical surface temperature of a weld pool calculation assuming ionization of evaporated atoms at $T_{plasma} = 6500[K]$. The current as well as the evaporation losses are unrealistically high.	47
Figure 32: Heat flux to the cathode, assuming ionization of a constant density of iron atoms in LTE at $T_{plasma} = 7000[K]$	49
Figure 33: Current density to the cathode, assuming ionization of a constant density of iron atoms in LTE at $T_{plasma} = 7000[K]$	50
Figure 34: Hypothetical surface temperature of a weld pool calculation assuming ionization of a constant density of iron atoms in LTE at $T_{plasma} = 7000[K]$. Losses due to evaporation are significant.	51
Figure 35: Saturated vapor density $n_{vap}(ps)$ compared with the constant iron atom density $n_{Fe} = const$	52
Figure 36: Comparison of ionized atoms at LTE with constant $T_{plasma} = 7000[K]$, once due to constant density and once due to saturated vapor pressure.	53

Figure 37: The ion density in LTE for <i>T_{plasma,local}</i> modified by metal vapor according to Eq.(14), assuming <i>T_{plasma,bulk}</i> = 7000[K], showing the behavior when considering only ionization of atoms from vapor or from the plasma bulk, and their combined influence.....	60
Figure 38: Heat flux according to the model presented in 4.1.1, with <i>UD</i> = 17[V] and <i>T_{plasma,bulk}</i> = 7000[K]	62
Figure 39: Heat flux according to the model presented in 4.1.1, with <i>UD</i> = 17[V] and <i>T_{plasma,bulk}</i> = 12000[K]	64
Figure 40: Comparison of current density due to ions and due to field-enhanced thermionic emission	65
Figure 41: Ionization degree according to the model presented in 4.1.1, with <i>T_{plasma,bulk}</i> = 7000[K]	66
Figure 42: <i>T_{plasma,local}</i> for different <i>T_{plasma,bulk}</i>	66
Figure 43: Heat flux dependency on <i>T_{plasma,bulk}</i> , with indication of the cathode surface temperature with maximum heat flux	67
Figure 44: Current density dependency on <i>T_{plasma,bulk}</i> , with indication of the cathode surface temperature with maximum current density.....	68
Figure 45: Heat flux dependency on <i>UD</i> , with fixed temperature of the plasma bulk <i>T_{plasma,bulk}</i> = 7000[K]	69
Figure 46: Current density dependency on <i>UD</i> , with fixed temperature of the plasma bulk <i>T_{plasma,bulk}</i> = 7000[K].....	70
Figure 47: Computational domain for the weld pool calculation including mesh.....	74
Figure 48: Specific Heat, thermal conductivity and electrical conductivity, as used, from [MOK17] (temperature ranges were extrapolated)	75
Figure 49: Heat flux due to evaporation, according to Knight model [KNI79]	78
Figure 50: Surface temperature field with weld pool depth, width and length indicated, as well as maximum temperature. The black contour line gives the melting isothermal. a) was published in [MOK20b].....	80
Figure 51: Cross Sections with weld pool depth, width and length indicated, as well as maximum temperature.....	81

Figure 52: Comparison between Gaussian (a) and EDACC (b) heat flux distribution for basic case.....	83
Figure 53: Heat flux distribution due to the EDACC model, with total current, total net heating power as well as total heat losses by evaporation indicated, as well as the maximum heat flux indicated. a) was published in [MOK20b].....	84
Figure 54: Current density distribution due to the EDACC model, with total current indicated. a) was published in [MOK20b]	85
Figure 55: Current density vector field on the melting iso-surface, with the maximum current density indicated. Welding direction from left to right.....	89
Figure 56: Electromagnetic force density in the melt pool, with the maximum value indicated. Welding direction from left to right.	90
Figure 57: Flow velocity in the melt pool, with the maximum value indicated. Welding direction from left to right.	92
Figure 58: Flow velocity streamlines in the weld pool, with the maximum velocity indicated	93
Figure 59: Subsonic flow structure, from [KNI79]	111

III List of tables

Tabellenverzeichnis

Table 1: Reference index for the overview of results.....	79
---	----

IV List of abbreviations

Abkürzungsverzeichnis

1D	one dimensional <i>eindimensional</i>
2D	two dimensional <i>zweidimensional</i>
3D	three dimensional <i>dreidimensional</i>
AC-TIG	alternate current tungsten inertgas welding <i>Wechselstrom Wolfram-Inertgas-Schweißen</i>
Ansys CFX	commercial computational fluid dynamics software <i>kommerzielle Fluiddynamik Software</i>
Ar	argon <i>Argon</i>
Ar+++	triple ionized argon <i>dreifach ionisiertes Argon</i>
CFD	computational fluid dynamics <i>rechnergestützte Strömungsdynamik</i>
CMT	“cold metal transfer” - mode of welding operation <i>“cold metal transfer” – eine Schweißtechnik</i>
CO ₂	carbon dioxide <i>Kohlenstoffdioxid</i>
Cr	chromium <i>Chrom</i>
Cu	copper <i>Kupfer</i>

	explosive centre electron emission mechanism
ECTON	<i>Elektronenemissionsmechanismus, der von Mikroexplosionen ausgeht</i>
EDACC	Evaporation Determined Arc-Cathode Coupling <i>Verdampfungsbestimmte Kopplung von Lichtbogen und Kathode</i>
Eq.	Equation <i>Gleichung</i>
ESAB	welding equipment manufacturer <i>Schweißzusatzwerkstoffhersteller</i>
EWM	welding equipment manufacturer <i>Schweißgerätehersteller</i>
Fe	iron <i>Eisen</i>
G3Si1	a welding wire quality <i>eine Schweißdrahtgüte</i>
GMAW/GMA	gas metal arc welding <i>Metallschutzgas Schweißen</i>
He	helium <i>Helium</i>
HTC	heat transfer coefficient <i>Wärmeübergangskoeffizient</i>
LTE	local thermodynamic equilibrium <i>lokales thermodynamisches Gleichgewicht</i>
MHD	magneto-hydrodynamic <i>Magnetohydrodynamik</i>
MSG	<i>Metall-Schutzgas (=GMAW)</i>

ND	neutral density filters <i>Neutraldichtefilter</i>
NEC	net emission coefficient <i>Nettoemissionskoeffizient</i>
O ₂	molecular oxygen <i>molekularer Sauerstoff</i>
OpenFOAM	an open source CFD software package <i>ein quelloffenes Softwarepaket für Strömungsdynamik</i>
PhD	academic degree of Doctor of Philosophy <i>akademischer Doktorgrad</i>
pLTE	partial thermodynamic equilibrium <i>teilweises thermodynamisches Gleichgewicht</i>
Ti	titanium <i>Titan</i>
TIG	tungsten inert gas <i>Wolfram Inertgas Schweißen</i>
UV	ultra violet <i>ultraviolett</i>
V	Volt <i>Volt</i>
W	tungsten <i>Wolfram</i>
WTWD	work piece to wire distance <i>Abstand zwischen Elektrodenspitze und Werkstück</i>
Zr	zirconium <i>Zirkonium</i>

V List of symbols

Formelzeichen

\vec{A}	$\left[\frac{N}{A}\right]$	Magnetic vector potential from [MOK17]
ΔA	$[eV]$	Lowering of the work function
A	$[eV]$	Work function (4.5[eV] for iron)
A_{eff}	$[eV]$	Effective work function (work function with Schottky correction)
\vec{B}	$\left[\frac{N \cdot s}{C \cdot m}\right]$	Magnetic field vector from [MOK17]
β_A	$[K^{-1}]$	Thermal expansivity coefficient from [MOK17]
c_{ion}	$\left[\frac{m}{s}\right]$	Ion speed of sound
d	$[m]$	Thickness of the welded plate in the CFD simulations
d	$[m]$	Ionization length in [BEN15]
d_{wire}	$[m]$	Diameter of the wire
e	$[C]$	Elementary charge
ε_0	$\left[\frac{A \cdot s}{V \cdot m}\right]$	Vacuum permittivity
E_f	$\left[\frac{V}{m}\right]$	Electric field at the cathode surface
E_{ion}	$[eV]$	Ionization energy
E_{ion}	$[eV]$	First ionization energy
\vec{g}	$\left[\frac{m}{s^2}\right]$	Gravitational acceleration from [MOK17]
γ	$[-]$	Ratio of specific heats
Γ_{vap}	$\left[\frac{1}{m^2 s}\right]$	Rate of vaporization as used in [COU97]

h	$[J \cdot s]$	Planck constant
h	$[J]$	Enthalpy from [MOK17]
H	$\left[\frac{J}{mol}\right]$	Heat of vaporization
H_{vap}	$\left[\frac{J}{mol}\right]$	Condensation enthalpy
I	$[A]$	Total current
j	$\left[\frac{A}{m^2}\right]$	Current density
\vec{j}	$\left[\frac{A}{m^2}\right]$	Current density vector in [MOK17]
$j_{diffuse}$	$\left[\frac{A}{m^2}\right]$	Estimated current density for diffuse arc attachment
j_e	$\left[\frac{A}{m^2}\right]$	Current density due to back-diffused electrons in [BEN95]
j_{em}	$\left[\frac{A}{m^2}\right]$	Current density of field-enhanced thermionic or thermo-field emission
j_{em}	$\left[\frac{A}{m^2}\right]$	Current density due to field-enhanced thermionically emitted Electrons in [BEN95]
j_{em}	$\left[\frac{A}{m^2}\right]$	Current density due to thermo-field emission in [COU97]
$j_i^{(d)}$	$\left[\frac{A}{m^2}\right]$	Ion current density in diffusion approach in [BEN15]
$j_i^{(f)}$	$\left[\frac{A}{m^2}\right]$	Ion current density in multi-fluid approach in [BEN15]
j_i	$\left[\frac{A}{m^2}\right]$	Current density due to ion flux in [BEN95]
j_{ion}	$\left[\frac{A}{m^2}\right]$	Current density due to ions in [COU97]

j_{ion}	$\left[\frac{A}{m^2}\right]$	Current density due to ions
j_{spot}	$\left[\frac{A}{m^2}\right]$	Current density in the cathode spot
$j_{tot}(p_{max})$	$\left[\frac{A}{m^2}\right]$	Total current density at maximal vaporization pressure in [COU97]
j_{total}	$\left[\frac{A}{m^2}\right]$	Total current density
J_{em}	$\left[\frac{1}{m^2}\right]$	Particle flux of thermionically emitted electrons in [BEN95]
J_i	$\left[\frac{1}{m^2}\right]$	Ion particle flux in [BEN95]
J_{vap}	$\left[\frac{1}{m^2 s}\right]$	Flux of evaporated atoms in [BEN93]
J_{vap}	$\left[\frac{kg}{m^2 s}\right]$	Evaporated mass flux
k_B	$\left[\frac{J}{K}\right]$	Boltzmann constant
$k_{ionization}$	$\left[\frac{m^6}{s}\right]$	Ionization rate as used in [BEN95]
$k_{recombination}$	$\left[\frac{m^6}{s}\right]$	Recombination rate as used in [BEN95]
l_{Debye}	$[m]$	Debye length
l_{ion}	$[m]$	Length scale of ionization collisions
l_{therm}	$[m]$	Length scale of electron energy relaxation
λ	$\left[\frac{W}{m \cdot K}\right]$	Thermal conductivity from [MOK17]
λ_D	$[m]$	Debye-length in [BEN15]
λ_{ia}	$[m]$	Mean free path for collisions between ions and neutrals in [BEN15]
λ_u	$[m]$	Length of electron energy relaxation

λ_{vap}	$[m]$	Length of thermal influence of the metal vapor
μ_0	$\left[\frac{kg \cdot m}{s^2 \cdot A^2}\right]$	Magnetic vacuum permeability, also in [MOK17]
M_{Fe}	$\left[\frac{kg}{mol}\right]$	Molar mass of iron
\dot{m}	$\left[\frac{kg}{s}\right]$	Mass rate
m_{Fe}	$[kg]$	Atomic mass of iron
m_e	$[kg]$	Electron mass
m_{ion}	$[kg]$	Ion mass
n_0	$\left[\frac{1}{m^3}\right]$	Metal vapor particle density in the plasma bulk
n_{Ar}	$\left[\frac{1}{m^3}\right]$	Argon particle density
n_{Fe}	$\left[\frac{1}{m^3}\right]$	Iron vapor particle density
n_e	$\left[\frac{1}{m^3}\right]$	Electron particle density
n_i	$\left[\frac{1}{m^3}\right]$	Particle density of ions in [BEN15]
n_{ion}	$\left[\frac{1}{m^3}\right]$	Ion particle density
n_{ions}	$\left[\frac{1}{m^3}\right]$	Ion particle density
$n_{plasma,bulk}$	$\left[\frac{1}{m^3}\right]$	Particle density in the plasma bulk
n_{vap}	$\left[\frac{1}{m^3}\right]$	Density due to the saturated vapor pressure
N_A	$\left[\frac{1}{mol}\right]$	Avogadro constant

N_L	$\left[\frac{1}{m^3}\right]$	Loschmidt number
ν	$[Pa\ s]$	Viscosity
ω	$[-]$	Ionization degree in [BEN95]
p	$[Pa]$	Pressure, also in [MOK17]
p_{amb}	$[Pa]$	Ambient pressure
p_{atm}	$[Pa]$	Atmospheric pressure
p_{vap}	$[Pa]$	Saturated vapor pressure
P	$[W]$	Heat power
φ	$[V]$	Potential in [BEN15]
q	$\left[\frac{W}{m^2}\right]$	Heat flux
q_{cond}	$\left[\frac{W}{m^2}\right]$	Heat flux carried into the cathode
$q_{diffuse}$	$\left[\frac{W}{m^2}\right]$	Estimated heat flux for diffuse arc attachment
q_{em}	$\left[\frac{W}{m^2}\right]$	Heat flux due to electron emission
q_{evap}	$\left[\frac{W}{m^2}\right]$	Heat flux due to evaporation
q_{ion}	$\left[\frac{W}{m^2}\right]$	Heat flux due to ions
q_{max}	$\left[\frac{W}{m^2}\right]$	Maximum heat flux
q_{rad}	$\left[\frac{W}{m^2}\right]$	Heat flux due to radiation
q_{total}	$\left[\frac{W}{m^2}\right]$	Net heat flux
r_*	$[m]$	Radius of the cathode spot in [BEN95]
r_{HS}	$[mm]$	Radius of the heat source
r_{ch}	$[-]$	Ratio of cooling/heating in [BEN95]

$r_{droplet}$	$[m]$	Radius of the droplet
r_{ei}	$[-]$	Ratio of the energies delivered by the plasma electrons and by the ions in [BEN95]
R	$\left[\frac{kg \cdot m^2}{s^2 \cdot mol \cdot K} \right]$	Ideal gas constant
ρ	$\left[\frac{kg}{m^3} \right]$	Mass density from [MOK17]
ρ_{iron}	$\left[\frac{kg}{m^3} \right]$	Mass density of iron
ρ_k	$\left[\frac{kg}{m^3} \right]$	Mass density at the edge of the Knudsen layer
ρ_{wire}	$\left[\frac{kg}{m^3} \right]$	Mass density of the wire
$\overrightarrow{S_{droplet,u}}$	$\left[\frac{kg}{m^2 s^2} \right]$	Momentum source by droplets from [MOK17]
$S_{droplet,h}$	$[W]$	Enthalpy source by droplets from [MOK17]
σ	$\left[\frac{S}{m} \right]$	Electrical conductivity from [MOK17]
T	$[K]$	Temperature from [MOK17]
T_h	$[K]$	Heavy particle temperature
T_{amb}	$[K]$	Ambient temperature
$T_{boiling,copper}$	$[K]$	Boiling temperature of copper
$T_{boiling,iron}$	$[K]$	Boiling temperature of iron
$T_{droplet}$	$[K]$	Temperature of the droplet
T_e	$[K]$	Electron temperature
T_{e*}	$[K]$	Characteristic electron temperature in the near-cathode layer in [BEN95]
T_i	$[K]$	Ion temperature
T_{ion}	$[K]$	Ion temperature in [COU97]

T_k	[K]	Temperature at the edge of the Knudsen layer
T_{max}	[K]	Maximum temperature
T_{min}	[K]	Minimum temperature
$T_{plasma,bulk}$	[K]	Temperature of the plasma bulk
$T_{plasma,local}$	[K]	Local plasma temperature of the near-cathode plasma
T_{plasma}	[K]	Plasma temperature
T_{ref}, p_{ref}	[K], [Pa]	Temperature and pressure in reference state for CFD simulation
$T_{s,max}(q > 0)$	[K]	The maximum cathode surface temperature where the heat flux is still positive
T_s	[K]	Cathode surface temperature
$T_s(q_{max})$	[K]	The cathode surface temperature where the heat flux is at maximum
T_{vap}	[K]	Temperature of the vapor
$T_{w,max}(q > 0)$	[K]	The maximum cathode surface temperature where the heat flux is still positive
T_w	[K]	Cathode surface temperature as used in [BEN95] and [BEN15] and [ALM13]
$T_w(q_{max})$	[K]	The cathode surface temperature where the heat flux is at maximum
t	[s]	Time from [MOK17]
$t_{8/5}$	[s]	Measure for cooling time from 800°C to 500°C, as used in welding to determine formation of microstructure
v_{Bohm}	$\left[\frac{m}{s}\right]$	Bohm velocity
v_e	$\left[\frac{m}{s}\right]$	Electron velocity

v_{ion}	$\left[\frac{m}{s}\right]$	Ion velocity
v_{weld}	$\left[\frac{m}{min}\right]$	Welding velocity
v_{wire}	$\left[\frac{m}{min}\right]$	Wire feed velocity
x, y, z	$[m], [m], [m]$	Coordinates in the simulation domain
x_0	$[m]$	X-coordinate of center of the arc
y_0	$[m]$	Y-coordinate of center of the arc
\vec{u}	$\left[\frac{m}{s}\right]$	Flow velocity from [MOK17]
u_k	$\left[\frac{m}{s}\right]$	Bulk flow velocity at the edge of the Knudsen layer
U	$[V]$	Cathode layer voltage drop in [BEN95]
U_D	$[V]$	Cathode voltage drop
U_a	$[V]$	Anode voltage drop
V_c	$[V]$	Cathode voltage drop in [COU97]
Z_{Fe}	$[-]$	Partition function of iron atoms
Z_{Fe+}	$[-]$	Partition function of singly ionized iron ions
Z	$[-]$	Charge number of ions

VI Abstract

In gas metal arc welding (GMAW) process simulation, it is desired to predict the energy transferred to the process as well as the weld pool geometry. For this reason, the coupling of the arc to the welded material is of high interest, both at the cathode and anode. Although there exists a substantial body of work on the coupling of the arc to the cathode, the present models cannot be applied in the conditions of GMAW welding, as they give unphysical results. In particular, the current models usually result in very high cathode surface temperatures, i.e. above boiling temperature of the metals. After relevant experiments are presented and discussed, it is concluded that the current state of the art does not reflect the observations and that therefore a new approach needs to be developed. Furthermore, a dialectic argument is developed, namely that the coupling of the arc to the cathode in diffuse attachment of GMAW must be strongly determined by evaporation. The argument concludes that the current transfer is mainly carried by metal ions that are evaporated from the cathode surface and ionized in the near cathode plasma, and that this current transfer must be limited to below boiling temperature. The core hypothesis is that this limit results from a decrease of the ionization degree, due to cooling of the near cathode plasma by the cold metal vapor. Based on this argument, a mathematical model for the Evaporation-Determined Arc-Cathode Coupling (EDACC), is introduced in detail. The properties of the model are then analyzed by applying it to a simplified computational fluid dynamics (CFD) weld pool simulation and it shows that the model is in line with the observed cathode surface temperatures below boiling. Finally, also an outlook is given on possible applications of this new understanding of the arc-cathode coupling, as well as a discussion of open questions and current limitations of the model.

Kurzfassung

Bei der Prozesssimulation des Metall-Schutzgasschweißens ist es das Ziel, die auf den Prozess übertragene Energie sowie die Schweißbadgeometrie vorherzusagen. Aus diesem Grund ist die Kopplung des Lichtbogens an den geschweißten Werkstoff sowohl an der Kathode als auch an der Anode von herausragendem Interesse. Obwohl es einen umfangreichen Bestand an Arbeiten zur Kopplung des Lichtbogens an die Kathode gibt, können die vorliegenden Modelle unter den Bedingungen des MSG-Schweißens nicht angewendet werden, da sie unphysikalische Ergebnisse liefern. Insbesondere führen die aktuellen Modelle in der Regel zu sehr hohen Kathodenoberflächentemperaturen, d.h. oberhalb der Siedetemperatur der Metalle. Nachdem einschlägige Experimente vorgestellt und diskutiert wurden wird deutlich, dass der derzeitige Stand der Technik mit den Beobachtungen nicht in Einklang zu bringen ist und daher ein neuer Ansatz entwickelt werden muss. Weiterhin wird ein dialektisches Argument entwickelt, nämlich, dass die Kopplung des Lichtbogens an die Kathode unter den Bedingungen von diffuser Anbindung beim Metallschutzgasschweißen, als stark verdampfungsabhängig aufgefasst werden muss. Das Ergebnis dieser Argumentation ist die Schlussfolgerung, dass die Stromübertragung hauptsächlich von Metallionen getragen wird, die von der Kathodenoberfläche verdampft und im kathodennahen Plasma ionisiert werden, und dass diese Stromübertragung unterhalb des Siedepunkts begrenzt sein muss. Als Kernhypothese wird dann vorgeschlagen, dass diese Begrenzung durch eine Abnahme des Ionisationsgrades infolge der Abkühlung des kathodennahen Plasmas durch den kalten Metaldampf erfolgt. Auf dieser Argumentation aufbauend wird ein mathematisches Modell für die verdampfungsbestimmte Kopplung von Lichtbogen und Kathode (EDACC) eingehend vorgestellt. Die Eigenschaften des Modells werden dann in der Anwendung auf eine vereinfachte CFD-Schweißbadsimulation analysiert, und es zeigt sich, dass das Modell die beobachteten Kathodenoberflächentemperaturen unterhalb des Siedepunkts reproduziert. Schließlich werden noch ein Ausblick auf mögliche Anwendungen dieses neu gewonnenen Verständnisses über die Lichtbogen-Kathoden-Kopplung gegeben, sowie offene Fragen und gegenwärtige Begrenzungen des Modells diskutiert.

"Truth is much too complicated to allow anything but approximations"

- John von Neumann, 1947

1 Introduction

1.1 Gas metal arc welding

Gas metal arc welding (GMAW) is an arc welding process, with an electrical arc burning between a continuously fed wire electrode and the base material, see Figure 1. To protect the weld pool from the influence of the atmosphere, a shielding gas is provided. Judged by the amount of filler material sold, it is the most widely used welding process in the industry. [REI15]

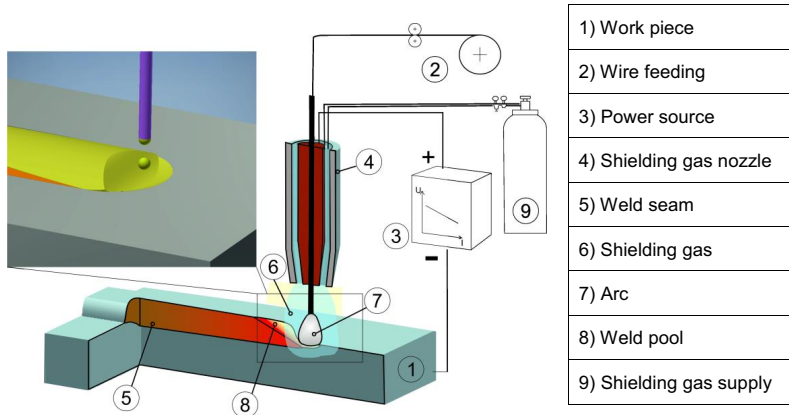


Figure 1: Schematic of the Gas Metal Arc Welding process [MOK19]

Abbildung 1: Schematische Darstellung des Metallschutzgasschweißverfahrens [MOK19]

To run a stable process, the welding power sources usually operate with a constant voltage characteristic, which gives rise to several GMAW process regimes: Short arc, Spray arc, High-power short arc, Rotating arc, High-power spray arc and Transitional ranges, see Figure 2. Here, mainly the Short arc and the Spray arc should be highlighted. In the Short arc mode, at lower currents and lower voltages (18[V] – 22[V]), the metal transfer from the wire electrode to the base metal occurs in the form of direct contact, where molten droplets form until they connect to the weld pool surface. Upon contact, the droplets are pinched off the wire electrode immediately by electromagnetic and surface tension forces, while creating a short circuit. The arc burns, extinguishes and ignites again in alternation and the most suitable shielding gas is pure CO₂, according to [REI15]. In the spray arc, at medium currents and voltages

(28[V] – 32[V] for steel), the wire is melted faster and the electromagnetic pinch forces detach small droplets from the wire, until even an almost continuous stream of metal is reaching the weld pool from the wire, while the arc burns continuously. For this mode, commonly inert gas or inert gas mixtures with CO₂ are used. For industrial applications, usually pulsed processes are being used. Here, the droplet detachment is triggered by a high current pulse, which allows more control over heat and mass input into the weld pool.

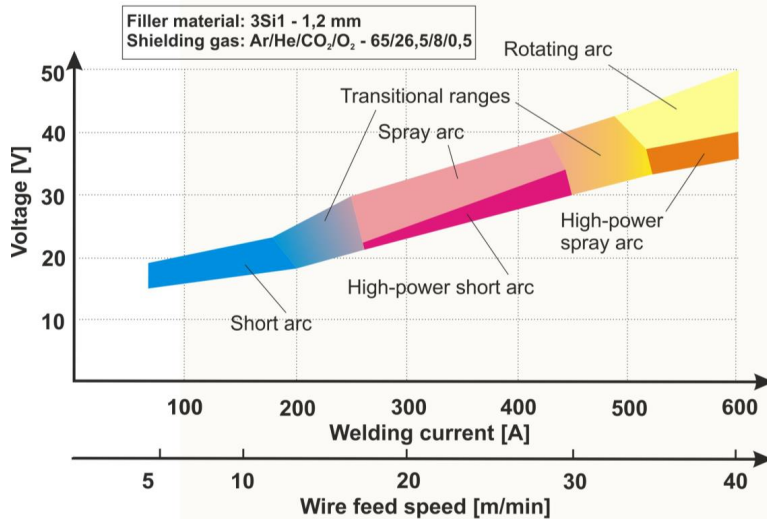


Figure 2: Example for stable voltage wire feed combinations in constant voltage GMA processes [REI15]

Abbildung 2: Beispiel für stabile Kombinationen von Spannung und Drahtvorschub, in MSG-Prozessen mit konstanter Spannung [REI15]

Although there have been experiments of GMAW in space [PAT72] or under water, usually the process is performed at atmospheric pressure.

1.2 The arc in GMAW

As the arc is the primary tool in the GMAW process, it is necessary to describe its structure in more detail. Unless in the case of a very short arc, as is the situation in temporal proximity to a short circuit, the electrical arc can usually be divided into three

distinctive zones: the plasma column, the anode boundary layer and the cathode boundary layer. While it is in the plasma column that the plasma is heated and maintained, it is in the boundary layers that the heat to the wire and to the work piece is generated and therefore these areas are of primary importance in the modelling of the GMAW process. Furthermore, the boundary layers determine not only the amount of heat, but they also determine the current density distribution and therefore the electromagnetic fields and forces in the entire process zone, as well.

1.2.1 Plasma column

In recent years a well-founded numerical [HER10], [SCH10a], [SCH10b] as well as experimental [ZIE07], [ROU10], [MUR10], [KOZ13] body of evidence has been established, which shows that the plasma column of the GMAW arc is heavily influenced by metal vapors. This is due to the sensitivity of the plasma transport properties, thermodynamic properties and radiation properties of inert gas plasmas to the presence of metal vapors [CRE15]. Especially the electrical conductivity, [CRE13] and the net emission coefficient (NEC) [GLE10] at lower plasma temperatures are very strongly influenced by metal vapors, even at concentrations of fractions of percent.

The source of metal vapors is commonly attributed to the anode [HA10], which in a standard GMAW process is located at the filler wire tip. Although the cathode (the work piece) is also evaporating, it is not considered the main source of metal vapors. This is due to the higher temperature at the anode and due to the direction of the Lorentz forces occurring in the GMAW arc plasma. It has been found that the direction of flow in the plasma gas is usually directed towards the work piece (except in situations with high vaporization rates [SCH10b]) and therefore the evaporation originating from the weld pool is driven out of the arc.

The most pronounced effect of the metal vapors on the structure of the arc is that at the center of the arc, a metal vapor plasma core is forming, which has a decidedly lower temperature than the surrounding argon plasma, cf. [ZIE07], [ROU10], [MUR10], [KOZ13], [SCH10a], [SCH10b], [NOM17]. The concentration found for the metal vapors varies from $\frac{n_{Fe}}{n_{Ar}} = 10^{-4}\%$ [VAL10] over 10-30% in [NOM17], 10-50% (iron mass fraction) in [KOZ13] and 45-70% (iron mol fraction) in [ROU10], to 70-100% (iron mass fraction) [SCH10a], [SCH10b]. The recent work of [NOM17] also features a 3D measurement of temperature and metal vapor concentration using a multidirectional spectroscopic method. It shows that the electron number density as well as the

temperature of the arc is not distributed axisymmetrically, while the iron vapor is concentrated in the arc center, close to the anode wire droplet. It is interesting to note, that the effect of a temperature minimum at the center does not appear in pure CO₂ shielding gas, according to [ZIE07], while it does appear in [NOM17]. As the work of [ZIE07] performs a line measurement through the arc at the cross-section with the wire position, it might be the main reason, that the temperature minimum does not become apparent in [ZIE07], as in this work, axis-symmetry is assumed.

Finally, it is necessary to state that the arc is usually assumed to be in local thermodynamic equilibrium (LTE), e.g. [LOW10], which means that the temperature of the heavy particles equals the temperature of the electrons. This assumption seems to be reasonably justified over a radius of up to 5mm in typical GMA arcs with pure argon shielding gas, as found in [VAL11].

1.2.2 Plasma-electrode boundary layers

1.2.2.1 Anode layer

As the anode boundary layer was not object of the investigation of this work, just a few general facts are included for completion. It is now sufficiently well known that the voltage drop at the anode U_a might be negative in GMA welding, depending on the anode temperature, see [KRI10b] or [KHR18]. This means that the electrons do not lose kinetic energy, when passing through it from the plasma to the anode, but that they will actually gain energy, so that it can be understood as the plasma converting its thermal energy into electrical energy. This remarkable effect occurs due to the different particle mobility of electrons and ions. As the ions have a higher mass, their velocity at a higher temperature in the LTE plasma is much smaller than that of the electrons. This leads to the effect of the electrons having a higher probability to be at the boundary of the plasma, than the ions, and the plasma generally having net-negative potential at the plasma boundary, in relation to the plasma center. This leads to the effect of the electrons being pushed towards the anode by the thermal enthalpy of the plasma.

Another important feature is to understand the heating mechanism at the anode. In [SEM16] it is shown that the major mechanism of heating of the anode is due to the

electrons releasing the work function of the anode material upon being absorbed back in the anode metal.

Finally, as was mentioned before, the properties of the anode layer are heavily influenced by evaporation in GMA welding. Here, two conditions are especially distinguished: the first, where the anode surface temperature is lower than the boiling point, so that the evaporation progresses in a saturated mode (“diffuse mode”) and the second where the surface temperature is higher than the boiling point, so that the evaporation progresses in a much more intense way (“convective mode”) [KRI10b].

1.2.2.2 Cathode layer

As the special dimensions of this layer are very small and any direct measurement has not yet been accomplished, theoretical considerations about this physical phenomenon are of great importance for the understanding of the processes involved. But firstly, for physical description of the cathode layer, several cases need to be distinguished. The first categorization concerns the temperature of the cathode and therefore there is a distinction between a “hot cathode” and a “cold cathode”. The main difference between these types of cathodes is, that in the case of a “hot cathode”, the cathode surface reaches temperatures, where the occurring current density can be largely explained by the so-called field-enhanced thermionic or thermo-field emission. Field-enhanced thermionic or thermo-field emission is a type of electron emission that occurs when a metal surface is heated to a high temperature and an electric field is applied to the surface [NOT56]. In many publications this type of emission is also simply referred to as thermionic emission, while still considering the Schottky effect, i.e. the lowering of the effective work function by an electric field. In GMAW arc discharges, this electric field is being provided by the power source, as a potential between the wire electrode and the work piece, but it is greatly enhanced in a small area close to the cathode, the so-called cathode layer or cathode sheath. There, at a distance of a few Debye-lengths, ions are accumulated in the plasma, due to the before mentioned difference in particle mobility between electrons and ions, which generate strong gradients of the electric potential to the negatively charged cathode [LAN29]. However, the temperatures necessary to generate current densities as they are being observed in arc welding, at the electric field strength that can be expected in such case, are higher than $\geq 3500[K]$ [BEN07]. This means that only cathodes made from highly refractory material, like tungsten can operate as these types of “hot cathodes”, as for more

volatile materials, like e.g. steel or copper, the heat losses by evaporation would prohibit reaching such high temperatures, which are much larger than their respective boiling temperatures (e.g. $T_{\text{boiling,iron}} = 3134[\text{K}]$, $T_{\text{boiling,copper}} = 2835[\text{K}]$).

This is the reason, why cathodes made from non-refractory material, like iron or copper are called “cold cathodes”. Although of everyday practical use, for example in the case of GMAW, the mechanism of current generation at the arc-cathode interface is not very well understood and therefore the body of works concerned with their theoretical treatment is much less extensive than in the case of “hot cathodes”. In [COU97], the distinction between non-refractory (“cold”) and refractory (“hot”) is based on the ratio of the rate of vaporization Γ_{vap} and rate of thermo-field emission $\frac{j_{\text{em}}}{e}$ (see Figure 3).

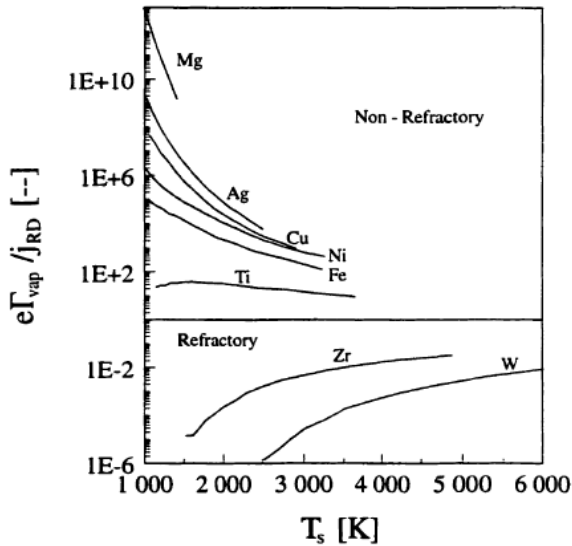


Figure 3: Calculated ratio of the flux of vaporized atoms to the flux of thermo-field emitted electrons as a function of the cathode surface temperature T_s for different cathode materials, from [COU97]

Abbildung 3: Berechnetes Verhältnis des Teilchenstromes der verdampften Atome zum Teilchenstrom der thermofeld-emittierten Elektronen als Funktion der Kathodenoberflächentemperatur T_s für verschiedene Kathodenmaterialien, aus [COU97]

Those materials where the flux of vaporized particles dominates are categorized as non-refractory (“cold”), e.g. Cu or Fe, while those materials where the flux of thermo-field emitted electrons dominate, e.g. W or Zr, are categorized as refractory or (“hot”).

The next distinction concerns the mode of current transfer, as the arc can be attached to the cathode by microscopic spots of very high current density, the so-called “spot mode”, or rather diffusely in a so-called “diffuse mode”. Especially the high current densities of up to $j_{spot} \sim 10^{13} [\frac{A}{m^2}]$ occurring in the spots are not yet sufficiently explained, especially for cold cathodes. One possible explanation of the mechanism is the ECTON (explosive electron emission) approach, which assumes very high local field strengths, due to protrusions of extreme aspect ratio [MES05]. However, this theory is usually applicable only to vacuum arcs with solid surfaces, where these kinds of protrusions could form. Another possible explanation is offered by [COU97] for solid cathodes, where thermo-field emission due to high densities of ionized metal vapor is responsible, but these high densities require pressures much higher than atmospheric pressure. However, spots also occur on liquid cathodes, for example on the melt pool of an AC-TIG (alternate current tungsten inert gas) welding process of aluminum in atmospheric pressure argon or helium shielding gas, e.g. [LE 19].

Additionally, under some conditions, there also seems to exist a form of diffuse attachment (also known as “spotless” mode of current transfer), see [BEN14] and [BEN15], or as will be shown later in the preliminary works. There, no spots are apparent and the current is spread over the whole area, with current densities being much lower ($j_{diffuse} \sim 10^5 - 10^8 [\frac{A}{m^2}]$) than in the “spot mode” [BEN15].

Finally, also the ambient pressure will characterize the mechanisms of the discharge. For example, a vacuum arc will differ from an arc at atmospheric pressure, as in a vacuum arc, the plasma needs to be created from the material that is eroded from the cathode spots. In atmospheric pressure arcs, a plasma of significant density will be present close to the cathode, giving rise to interactions and conditions, which are absent in the vacuum arc.

2 State of the art

2.1 Substitution models used in GMAW process simulation

In GMAW process simulation it is acknowledged, that the processes responsible for the generation of heat flux and current density in the cathode region are still not thoroughly understood and therefore, usually simplified substitution models are being applied.

The most common simplification of the cathodic heat source in GMAW process simulation is the assumption of an axisymmetric or elliptical Gaussian distributed heat source, following the approach of Rykalin and Rosenthal [RYK57] for arc welding processes (initially TIG) and taking the total power as the product of current and voltage, as it is still being used e.g. in the recent works of [OGI18] or [JEO18]. As the processes in the arc follow a stochastic pattern to a certain degree, the assumption of a Gaussian normal distribution seems to follow naturally. Also the mathematical simplicity of the description offered many advantages in the analytical calculation of the temperature field, especially for the calculation of the $t_{8/5}$ time, in times before computer simulation was possible. However, this approach has a very obvious drawback, as it provides the highest heat flux concentrated at the center, where the highest temperature is. This leads to very strong local overheating, that means surface temperatures considerably higher than boiling temperature and therefore in principle to strong losses due to evaporation. However, in the works by [OGI18] and [JEO18], heat losses by evaporation were not considered.

In the following, the more advanced models for heat and current distribution in GMAW as found in the literature are presented and roughly analyzed.

In the model of Xu, Hu and Tsai [XU09], the heat flux at the cathode is modelled by an effective thermal conductivity between the plasma and the cathode which is a parameter to be calibrated by an experiment. The approach is strongly simplified and does not capture the basic physics of the situation, i.e. neither the ion fluxes nor the electron emission cooling. So, while it can be calibrated to accommodate all occurring situations, the effective thermal conductivity will strongly differ under differing conditions, thereby having only weak predictive power and no insight in the true mechanisms of the process. Also, the effect of the cathode layer on the current density is neglected. The current density is calculated from boundary conditions on the wire and the bottom of the base metal, according to current continuity and Ohm's law, all

while taking the electrical conductivity as a constant over the entire domain. The resulting current density distribution appears to be axisymmetric.

In the model of Murphy [MUR11], the “LTE diffusion model” for the heat flux according to Lowke and Tanaka [LOW08] is used, where the electron emission is attributed to the impact of excited atoms onto the cathode surface. There, a statement is made about thermal ionization with reference to a previous paper by Lowke and Quartel [LOW97a], which deals with an argon plasma at 15000[K]. It is stated, that thermal ionization cannot be responsible for the electron generation, because then the sheath voltages would be too large by orders of magnitude. However in the relevant works [LOW97a] and [LOW97b], it is stated that ionization is likely to contribute to the electron current in the cathode sheath, either by photoionization [LOW97a] or thermal ionization [LOW97b], which is an apparent contradiction. Most likely [LOW08] is referring to ionization by the electric field. The actual model that is used by Murphy is then a very simple expression for the electrical power as a product of the current density with the cathode fall voltage, which was derived from experiments. However, the electrical current density is here again calculated from the boundary conditions, i.e. a current density at the wire cross section and a zero potential at the bottom of the work piece. Here, the electrical conductivity is given in a rough temperature dependence, independently for liquid and solid metal. The definition of the electrical conductivity of the plasma remains unclear in this work. Therefore, the cathode layer is not considered when establishing the current density distribution on the weld pool surface. However, the resulting distribution of the current density appears to be not axisymmetric, when applied to an asymmetrical weld pool shape.

In the PhD thesis of Hertel [HER16], the approach of Lowke and Tanaka [LOW08] is used as well. Here, also another approach is used, where the electrical conductivity on the surface is determined by the average temperature between the last element of the calculation mesh of the electrode and the first element of the mesh of the plasma region. With adjusting the element size in this critical region to a suitable value, a good agreement can be achieved with more complex cathode layer models. However, the resulting element size turns out to be quite coarse, so that the capturing of flow processes close to the electrodes is heavily impaired. Alternatively, the author suggests a method following [XU09], which allows to formulate jump conditions between the electrode temperature and plasma temperature, however with the cathode surface temperature derived analytically and fixed for this calculation. The

current density is calculated according to the boundary conditions on the wire cross section and the bottom of the base metal, but also taking into account the electrical conductivity of the plasma gas, including metal vapors.

2.2 Cathode layer models derived from plasma physics

2.2.1 Models for arc-cathode coupling in diffuse arc attachment with a “hot cathode” at atmospheric pressure in inert gas:

Interaction of a “cold cathode” with the arc plasma, as is the case in GMAW, is less understood than its interaction with a “hot cathode”, therefore the body of work on the modelling of the interaction of an arc with a “hot cathode” is more extensive. Usually these attempts apply a magneto-hydrodynamic (MHD) solution for the plasma phase and couple it to a thermal and electrostatic solution for the solid thermo-field emitting tungsten electrodes, while explicitly considering the special conditions at the interface between plasma and electrode. In general, the effects of metal vapor are not considered except in one case [KAD95], but in this case the effects are restricted to the thermodynamic and the transport properties (i.e. thermal and electrical conductivity) of the plasma phase, as well as in the energy balance of the space charge sheath.

The general principle of the arc cathode coupling consists mainly of the following mechanisms:

- 1) the ions of the plasma form a space charge sheath in front of the cathode, due to the higher mobility of the electrons, compared to that of the ions (at thermal equilibrium, i.e. equal kinetic energies the ratio of velocities follows the inverse of the square-root of the ratio of particle masses $\frac{v_e}{v_{ion}} = \sqrt{\frac{m_{ion}}{m_e}}$ with $m_{ion} \gg m_e$);
- 2) the ions generated in the cathode layer or in the plasma reach the cathode surface and heat the cathode surface, by depositing their kinetic energy, gained in the voltage drop of the space charge sheath, and the ionization energy to the cathode surface;
- 3) due to the heat and the electric field of the space charge sheath, the cathode emits electrons, which are accelerated and contribute to ionize the plasma.

The following will give a review over some of the most prominent approaches, as documented extensively in PhD theses, and highlight their perceived characteristics. After that, the ground breaking model of Benilov and Marotta [BEN95] is discussed, as it serves as the theoretical basis for most modelling approaches concerned with modelling the cathode layer of a “hot cathode”.

2.2.1.1 PhD thesis of Kaddani. 1995

In the thesis of Kaddani [KAD95] the arc between a tungsten cathode and a copper anode in an argon atmosphere at atmospheric pressure, as encountered in TIG (Tungsten inert gas) welding, is modelled in 2D and 3D. There the interaction of the arc with the electrodes is modelled as well as the influence of the copper and tungsten vapors on the plasma properties in the arc column is taken into account. As the thesis was published in the same year as Benilov and Marotta’s ground-breaking paper on the modelling of the cathode layer [BEN95] was published, it uses a different approach to model the cathode layer. The used approach was developed by Hsu [HSU83] and Delalondre [DEL90], where the ionization zone is described as a region of non-equilibrium (i.e. two temperatures, one for electrons one for ions). The cathode region is considered as consisting of three parts: the surface, the space charge sheath and the ionization zone, see Figure 4. The most critical condition is the energy balance in the space charge sheath, considering the heat losses by tungsten evaporation. The current densities due to electrons and ions in the cathode sheath are given in terms of the electric field and the electrical conductivities, considering an argon-tungsten plasma. The electric field in the cathode sheath was expressed as a function of the total current density, the gradients of the electron and ion partial pressures, as well as the electrical conductivities of electrons and (tungsten and argon) ions. The cathode voltage drop was fixed at $U_D = 4 [V]$.

The conditions of the ionization zone serve here as a boundary condition for the space charge sheath. The assumptions used to close the system of equations for the ionization zone are that the temperature of the heavy particles (i.e. ions and atoms) is equal to that of the wall and that the electron current density is defined by the total current density and the ion current density. It is remarkable, that the latter one differs from all other models as the electron current density can usually be given in terms of the well-established Richardson-Dushman formula.

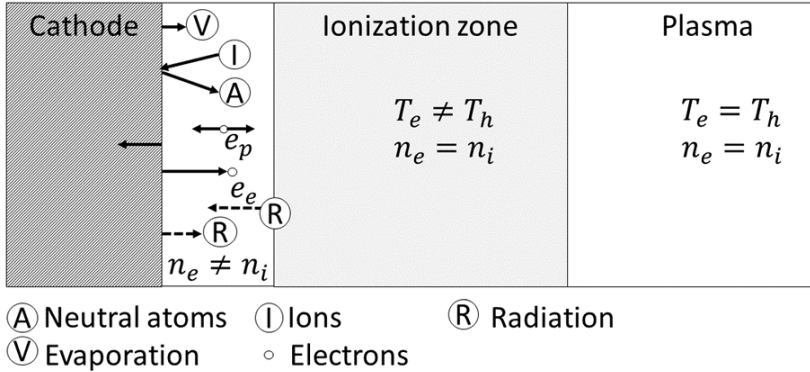


Figure 4: Schematic of the model for cathode region after Kaddani [KAD95]

Abbildung 4: Schematische Darstellung des Modells für den Kathodenbereich nach Kaddani [KAD95]

2.2.1.2 PhD thesis of Wendelstorf. 2000

In the PhD thesis of Wendelstorf [WEN00] a self-consistent (ab initio) quantitative modelling in 2D of an arc discharge with a tungsten cathode in different gases at a range of pressures is presented. The coupling between the arc plasma and the cathode is developed as a 1D description in detail (see Figure 5), strongly referencing the work of Benilov and Marotta [BEN95]. The plasma is considered to be in partial local thermodynamic equilibrium (pLTE). The electron emission from the cathode is described by the Richardson formula [RIC03], the electric field in the space charge layer is determined by the Mackeown formula [MAC29]. The cathode voltage drop is derived from the electron energy balance (referencing [BEN95]) in the space charge sheath.

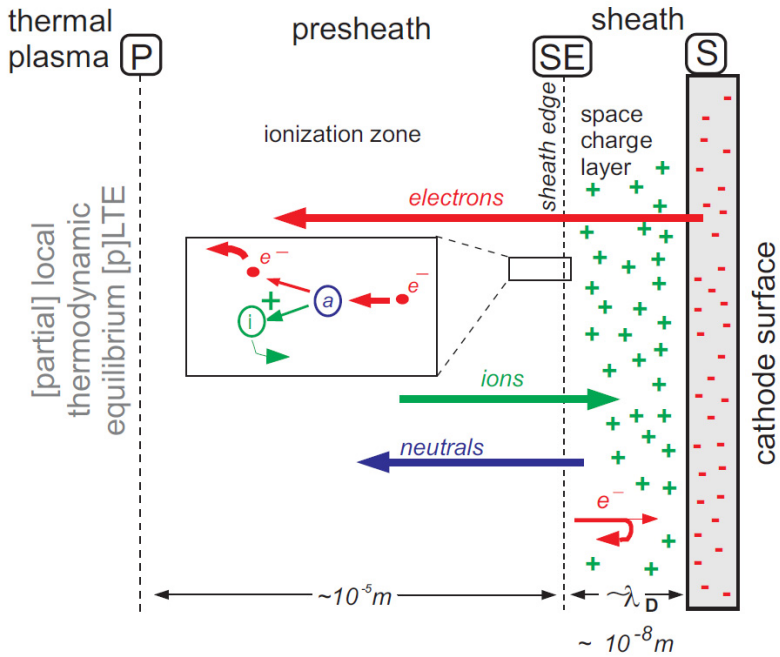


Figure 5: Schematic of the cathode layer as applied by Wendelstorf [WEN00]

Abbildung 5: Schematische Darstellung der Kathodenschicht, wie sie bei Wendelstorf angewendet wurde [WEN00]

The space charge sheath receives the pre-sheath voltage drop as well as the ion density on the sheath edge from the ionization zone, which again is calculated according to the model of Hsu [HSU83]. The ion current density is taken as the ion density at the sheath edge traveling with the Bohm velocity. The heat flux to the cathode surface then considers: ion heating, emission cooling, thermal radiation cooling, electron back diffusion heating, neutrals heat conduction and back flow of recombined ions. On the other side at the interface between pre-sheath and plasma, heating by the emitted electrons and Joule heating in the pre-sheath, as well as losses by ionization and back diffused electrons are considered. It should be noted that this model takes into account pLTE plasma only when calculating the voltage drop at the pre sheath and also, that in this approach there seems to be a net output of heat from the cathode layer to the plasma.

2.2.1.3 PhD thesis by Cayla. 2008

In the PhD thesis of Cayla [CAY08] a model for the interaction of an argon arc with a tungsten cathode is developed on the basis of the model by Benilov [BEN95]. However, the author notices some discrepancy between his implementation and the values presented in [BEN95]. It is notable, that the characteristic values derived from this model are always given as a function of the electron temperature of the plasma. It is also noteworthy, that the cathode voltage drop U_D , derived for comparably low electron temperatures varies widely, depending on the cathode surface temperature T_W ($U_D \ll 1[V]$ for $T_W = 5000[K]$ to $U_D = 30[V]$ for $T_W = 3000[K]$). Plasma electron temperatures of lower than $10000[K]$ are not considered at all. Here again, the constituting equation is the energy balance between the space charge sheath and the ionization zone. However, in contrast to [BEN95], the ionization degree is calculated in terms of a two-temperature plasma approach by [VAN89], where the Saha equation is generalized for a two temperature plasma, to depend in the first approximation only from the electron temperature. Also, the densities for ionization levels of argon up to Ar^{+++} are considered, while holding the Dalton equation for the pressure. This leads to much higher ion densities and ion fluxes than in [BEN95]. As another distinguished feature, the model considers secondary electron emission that seems to dominate over field-enhanced thermionic emission at low plasma electron temperatures. However, as a total value, the current density of the secondary electron emission is still comparably low ($< 10^4 [\frac{A}{m^2}]$) at these plasma electron temperatures.

2.2.1.4 PhD thesis by Shirvan. 2016

The thesis by Shirvan [JAV16] is explicitly concerned with the modelling of the cathode-plasma interaction in TIG welding arcs. A self-consistent model for the cathode layer was developed on the basis of the model of Cayla [CAY08] and implemented as a boundary condition in an OpenFOAM simulation. As a special feature it takes into account the distribution of an activator (e.g. thorium) over the surface of the cathode. The cathode layer model consists again of several sublayers, each constituting their own kind of dominant physics. It considers a space charge sheath, a Knudsen layer, an ionization layer and finally also the plasma. As an output it delivers the sheath voltage drop, the net heat flux to the cathode as well as the electron temperature at the sheath/pre-sheath interface. The two defining sets of equations are one for the number densities of argon ions and electrons and the other for the energy balance and

current continuity. Here, the resulting plasma temperatures are finally compared with experimental values, reaching good agreement. The electric field in this approach was calculated using the approach by [BEN95], from the Poisson equation and the Bohm criterion. For the electron emission two types of mechanisms were compared, namely the Richardson-Dushman formula with Schottky correction (field-enhanced thermionic emission) and the Murphy-Good formalism (thermo-field emission).

2.2.1.5 Benilov Marotta (1995) – „A model of the cathode region of atmospheric pressure arcs”

As became apparent in the analysis presented in 2.2.1.2-2.2.1.4, most models concerned with modelling the arc-cathode interaction with tungsten cathodes are based on the ground breaking paper by Benilov and Marotta [BEN95]. The model gives parameters of the layer as a function of the voltage drop and the local value of the cathode surface temperature. Several combinations for cathode material and plasma gas, among them tungsten/argon or thoriated-tungsten/argon, as used in TIG welding are presented. One of the primary concerns of the paper was to give a self-consistent model of the near-cathode layer, including the prediction of the radius of the cathode spot for atmospheric pressure arcs, by the means of a model for vacuum arcs [BEN93], which will be discussed in 2.2.2.3. First an analysis is performed of the length scales of the three layers of the region, which are characterized by particular deviations from LTE, i.e. $T_e \neq T_h$ (electron temperature differs from heavy particle temperature), $k_{ionization} \neq k_{recombination}$ (the ionization rate differs (is greater) than the recombination rate), $n_e \neq \sum n_{ions}$ (deviation from quasi-neutrality). These length scales are respectively: the length of electron energy relaxation, the recombination length and the Debye radius. It is important to note however, that it is assumed that the ionization degree of the plasma close to the near-cathode layer is comparable to unity, which is the case in a TIG-plasma, where the plasma temperatures reach values of $> 2.5 \cdot 10^4 [K]$. It is then supposed that the characteristic temperature in the layer is at $10^4 [K]$, which is in between the cathode surface temperature $T_w \sim 4000 [K]$ and the plasma temperature. It follows that, for the conditions considered, the thickness of the cathode layer is determined by the layer of thermal relaxation $l_{therm} \sim 100 \mu m$, the thickness of the ionization zone is determined by the ionization length $l_{ion} \sim 10 \mu m$ and thickness of the space charge sheath is determined by the Debye-length $l_{Debye} \sim 0.02 \mu m$ (compare to Figure 4 or Figure 5). It is stated there, that the establishment of a positive space

charge sheath in front of the cathode is necessary, because else the flux of electrons diffusing from the bulk plasma to the cathode would be much higher than both, the field-enhanced thermionic emission and the flux of ions moving from the plasma to the cathode. This would cause the unphysical situation where current was directed from the plasma to the cathode (so it would be reversed). The space charge sheath is considered as collisionless. The electrostatic potential in the sheath is determined by the Poisson equation, which is dependent on the electron and ion number densities. Both these densities can be derived from their values at the sheath edge. The resulting electric field at the cathode surface conforms with the Mackeown formula [MAC29] for $eU_D \gg k_B(T_e + T_i)$. It should be noted, that it is stated, that the dependence of the voltage drop $U_D(T_e)$ on electron temperature, quite strong for $T_e < 1.5 \cdot 10^4 [K]$. For the energy balance on the cathode surface, contributions from the ion flux, from the back diffused electrons from the plasma, as well as losses from the electrons emitted from the cathode are considered. Leading to the defining equation:

$$q = J_i \left[k_B \left(2T_i + \frac{ZT_e}{2} - 2T_w \right) + ZeU_D + E_{ion} - ZA_{eff} \right] + J_e (2k_B T_e + A_{eff}) - J_{em} (2k_B T_w + A_{eff}) \quad (1)$$

Where J_i is the ion flux, J_e is flux of back diffused plasma electrons, J_{em} is the flux of field-enhanced thermionically emitted electrons, T_i is the ion temperature, T_e is the electron temperature, T_w is the temperature of the cathode surface, Z is the charge number of ions, U_D is the cathode voltage drop, E_{ion} is the ionization energy, A_{eff} is the effective work function, e is the elementary charge and k_B is the Boltzmann constant. This means, that the contribution due to the ion flux considers a thermal component, an energy gain due to the cathode voltage drop, and the release of the ionization energy, minus the work function at the ion recombination at the cathode surface. The contribution due to back diffused plasma electrons considers a thermal component as well as the work function that would be released at the entry of the electron into the material, and the contribution of the field-enhanced thermionically emitted electrons considers a heat loss due to a thermal component and the work function, necessary to exit the cathode.

To obtain the aforementioned value for the ion number density at the sheath edge, a numerical solution of a multi-fluid equation for the ionization layer with constant electron temperature, constant and equal temperatures of neutrals and singly charged

ions is applied. It should be mentioned that this solution is only applicable, if the ionization degree would stay between $0.6 - 1$, as for values below this range, the plasma in the ionization layer cannot stay in static equilibrium. However, this limitation is neglected, for simplicity reasons. To obtain the aforementioned value for the electron number density at the sheath edge, the energy balance in the ionization layer is solved. The gains in the energy balance are constituted by the flux of energy brought in by emitted electrons accelerated in the space charge sheath and the work of the electric field over the electrons inside the layer. The losses in the energy balance are constituted by the flux of the energy carried away by the electrons, leaving the ionization layer for the sheath or the bulk plasma and by losses due to ionization.

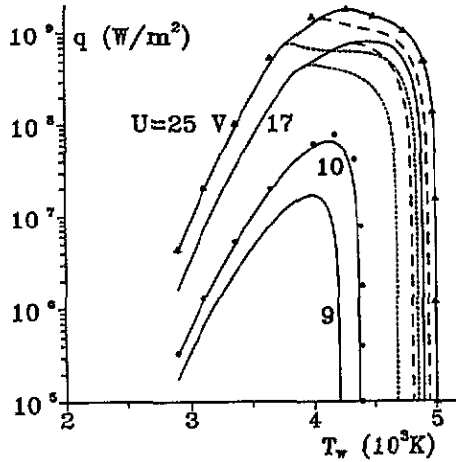


Figure 6: Resulting heat flux from [BEN95]. Full curves, broken curves and dotted curves take into account different ionization states of argon.

Abbildung 6: Resultierende Wärmestromdichte aus [BEN95]. Durchgehende Linien, unterbrochene Linien und gepunktete Linien stehen für die Berücksichtigung verschiedener Ionisationszustände des Argons.

As a result it is possible to obtain the heat flux to the cathode in dependence of voltage drop and cathode surface temperature $q(U, T_w)$, see Figure 6. It is important to note, that this result means, that the heat flux will be very strong for surface temperatures of $T_w > 4000[K]$, which means that the cathode layer will not stop heating the cathode until the maximal temperature is achieved. It should be noted, that for low cathode temperatures ($T_w = 4000[K]$) and low electron temperatures $T_e < 10000[K]$, the

contribution by the back diffused electrons becomes more significant. In Figure 7, taken from the work, it becomes apparent that all current densities j_i, j_e and j_{em} are monotonically increasing, with cathode surface temperature.

Finally it is stated, that the presented model of the near-cathode layer is independent of a solution in the arc column. This requires the assumption that the energy flux coming from the arc column does not play a decisive role in the energy balance of the layer.

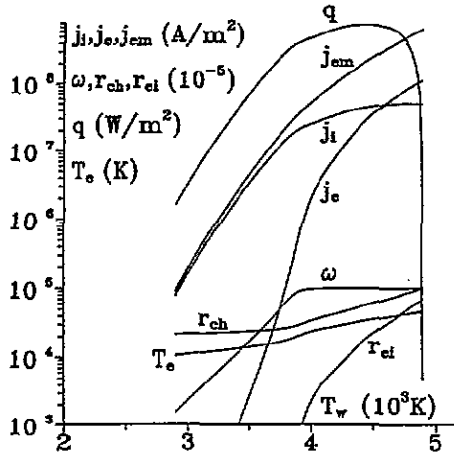


Figure 7: Densities of energy flux, ion current, electron emission, back-diffused electrons, electron temperature, ionization degree ω , the ratio of the energies delivered by the plasma electrons and by the ions r_{ei} and the ratio of cooling/heating r_{ch} , for $U = 17[\text{V}]$, from [BEN95].

Abbildung 7: Wärmestromdichte, der elektrischen Stromdichte durch Ionen, durch Elektronenemission, sowie durch rückdiffundierte Elektronen, Elektronentemperatur, Ionisationsgrad ω , das Verhältnis r_{ei} der von den Plasmaelektronen und von den Ionen zugeführten Energien und das Verhältnis von Kühlung/Heizung r_{ch} , für $U=17[\text{V}]$, aus [BEN95].

The resulting quantities of heat flux $q(U, T_w)$ and current density $j(U, T_w)$ can be precomputed as they do not depend on the total arc current or the shape of the cathode. With these, the temperature distribution inside the cathode body can be calculated and from there, the radius of the spot or the total heat power and total current can be calculated, but in general, for currents of $I \sim 200[\text{A}]$, the radius of the

cathode spot is found to be $0.3[mm] < r_s < 0.7[mm]$. It should be also noted that the characteristic electron temperature in the near-cathode layer $1.7 \cdot 10^4[K] < T_{es} < 4.3 \cdot 10^4[K]$, seems quite high. The results were compared with experimental data and the agreement has been found to be reasonable.

2.2.2 Models for cold cathodes

2.2.2.1 PhD thesis Coulombe (1997): Model for evaporating Cu, Fe, Ti cathodes

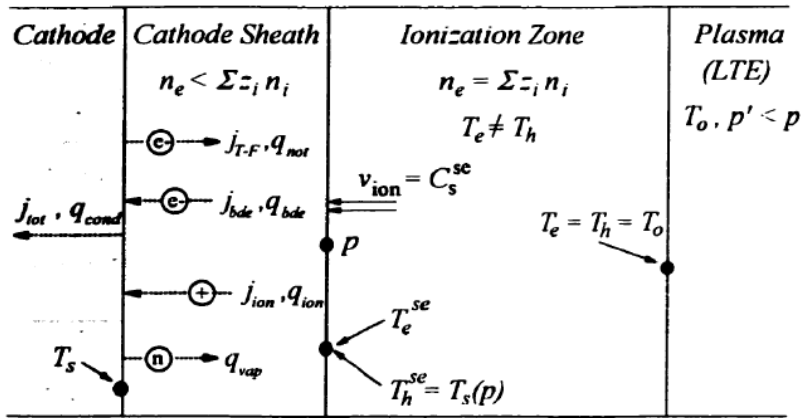


Figure 8: Schematic representation of the cathode region of an emitting cathode exposed to a high pressure arc, from [COU97]

Abbildung 8: Schematische Darstellung des Kathodenbereichs einer emittierenden Kathode eines Hochdrucklichtbogens, aus [COU97]

When considering the arc cathode coupling with a „cold cathode“, the body of work is much less extensive. However, there are a few works, concerned with the topic. One of the most important works in this field is the PhD thesis by Coulombe [COU97]. In this work, a physical model describing the electric arc attachment on solidified electron emitting non-refractory “cold cathodes” at atmospheric pressure is developed based on works [RET96] and [ZHO94], and applied to Cu, Fe and Ti cathodes. It is able to explain current densities of $j_{total} \sim 10^{10} \left[\frac{A}{m^2} \right]$, i.e. the conditions for the occurrence of “spot attachment” (several rapidly moving spots, constricted over $5 - 20 \mu m$ each). The structure of the model of the cathode region can be seen in Figure 8.

It compares thermionic (Richardson-Dushman), field-enhanced thermionic (Richardson-Schottky) and thermo-field emission (Murphy-Good), which depend on the strength of the electric field that has been build up by the space charge sheath. It is argued that the high current densities originate from the strong enhancement of the electric field due to high ion densities in the space charge sheath, which originate from vaporized atoms from the cathode surface that have been ionized. The deviation from LTE in the cathode region is considered, fixing the ion temperature at the temperature of the cathode surface $T_{ion} \approx T_w$ at the sheath edge, as a collisionless sheath is assumed. The electric potential is calculated by the Poisson equation and the electric field at the cathode surface is calculated by a method originally developed by Mackeown [MAC29] and later extended by Prewett and Allen [PRE76], each taking into account fluxes of ions, emitted electrons and back-diffusing electrons. The cooling by thermo-field emission is modelled in more detail than in [BEN95], by considering the Nottingham effect. However, this effect leads to a significant difference only for high electric fields and comparably low cathode surface temperatures. Therefore, it is stated to play a fundamental role mostly in the arc ignition process.

The essential criteria for self-sustaining arc operation are defined to be:

- The flux of emitted electrons must be larger than the flux by ions, i.e. $\frac{j_{ion}}{j_{em}} < 1$.
This constraint is considering that ionization in the cathode region is due to emitted electrons (by thermo-field emission), and each electron can ionize one atom at most, since at the considered energy range (10 – 20[eV]) only single-ionization upon electron impact occurs.
- The heat flux balance by electrons and ions must be positive to have a heating effect on the cathode surface, i.e. $q_{cond} > 0$

For the ionization degree, a generalized form of the Saha equation is applied, taking into account only electron temperature, but accounting for a lowering of the ionization potential and an increase in total plasma pressure, both due to a high density of charged particles in the cathode region. The cathode sheath voltage drop for a copper cathode was fixed to be 15[V], from experimental measurements.

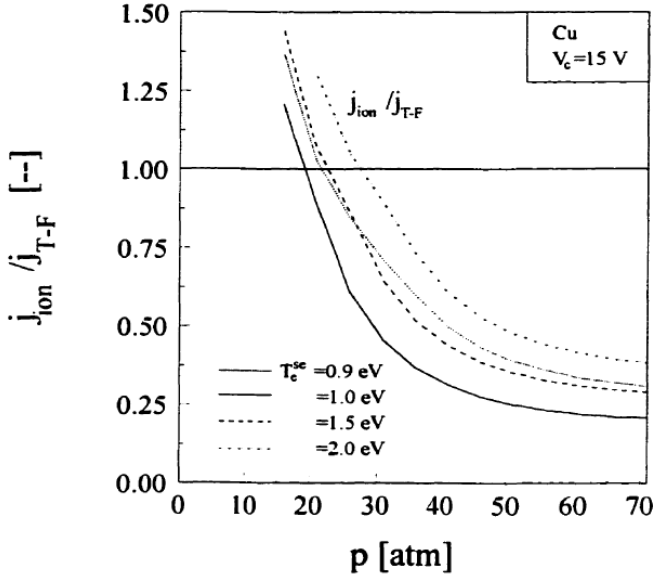


Figure 9: Ratio of ion current density to the current density due to thermo-field emission, from [COU97]

Abbildung 9: Verhältnis der Ionenstromdichte zur Stromdichte aufgrund von Thermofeldemission, aus [COU97]

The first criterion is only satisfied for temperatures with vapor pressures $p_{vap} > 19 [atm]$, see Figure 9, which indicates the necessity for strong vaporization of the cathode surface, which will then provide a sufficient ion density to sustain thermo-field emission. It is interesting to note, that the model finds that at high pressures, the thermo-field emission exceeds the flux of vaporization, fulfilling the criteria to be categorized as a “hot cathode, compare Figure 10 with Figure 3. However, it should be also noted, that the temperatures necessary to achieve such high local pressures are indicated in Figure 10 below the pressure ticks, and all of them are much in excess over boiling temperature of Cu, i.e. that for this model, boiling temperature is strongly exceeded. The resulting heat fluxes to the cathode are depicted in Figure 11, and besides showing very high values of heat flux $q \approx 10^{10} \left[\frac{W}{m^2} \right]$, again the temperatures, which can be deduced from the necessary pressures are much in excess of boiling temperatures. Figure 12 shows the resulting heat fluxes for a copper cathode with a

voltage drop of $V_c \triangleq U_D = 15[V]$. It should be noted that the current density is monotonically increasing.

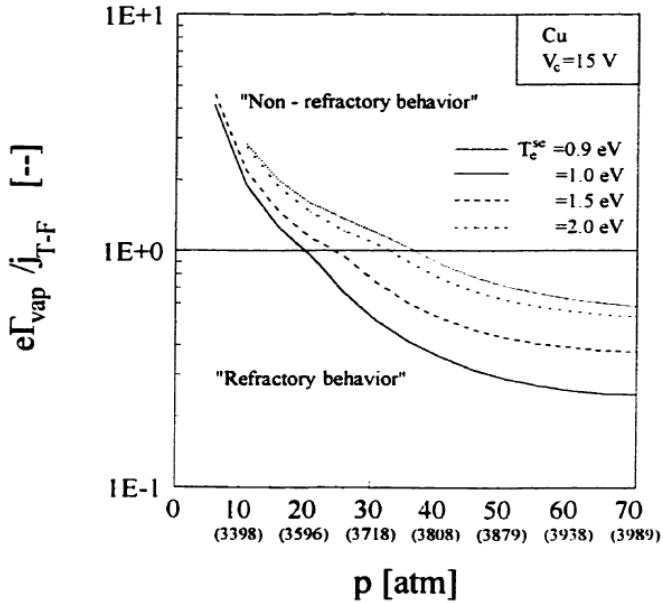


Figure 10: Ratio of flux of vaporization and flux by thermo-field emission for copper in dependence of electron temperature and saturated vapor pressure from the heated cathode surface, from [COU97]

Abbildung 10: Verhältnis des Teilchenstromdichte aufgrund Verdampfung und der Teilchenstromdichte durch Thermofeldemission für Kupfer in Abhängigkeit von Elektronentemperatur und dem Sättigungsdampfdruck der erhitzten Kathodenoberfläche, aus [COU97]

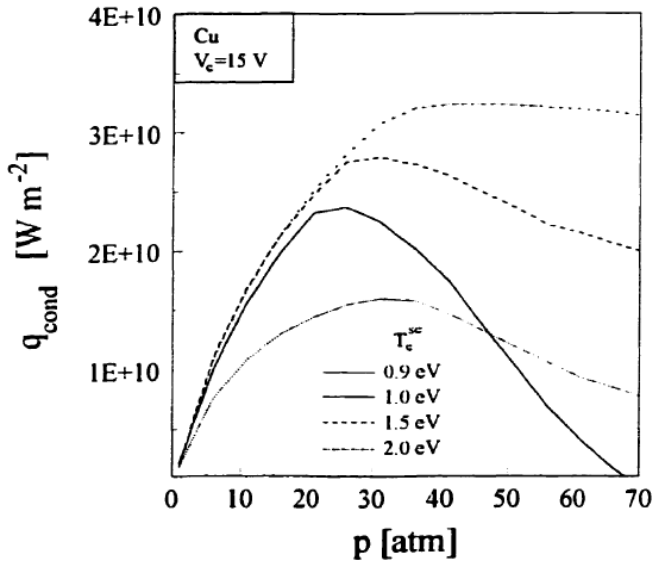


Figure 11: Heat flux to a copper cathode in an atmospheric arc cathode spot, from [COU97]

Abbildung 11: Wärmestromdichte an eine Kupferkathode in einem atmosphärischen Lichtbogenkathodenfleck, aus [COU97]

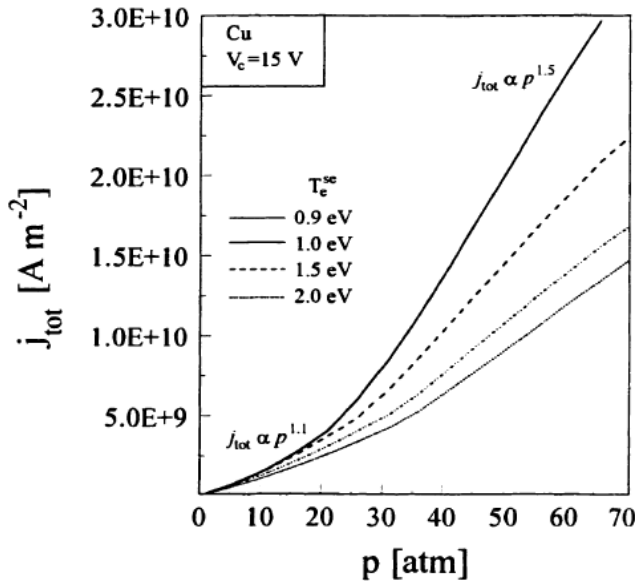


Figure 12: Current density to a copper cathode in an atmospheric arc cathode spot from [COU97]

Abbildung 12: Elektrische Stromdichte an eine Kupferkathode in einem atmosphärischen Lichtbogenkathodenfleck, aus [COU97]

In the further analysis, for Fe cathodes, also a surface temperature in excess of $T_s > 3780[K]$ is predicted, as well as current densities $j_{tot}(p_{max}) = 2.2 \cdot 10^{10} \left[\frac{A}{m^2} \right]$.

Finally, also the value of the cathode sheath voltage drop was shown to have only a minor influence on the ratio of current densities, comprising the first criterion for self-sustaining operation.

2.2.2.2 Models by Benilov (2015) and Almeida (2013) for vacuum arcs on evaporating Cr or CrCu cathodes.

Another line of work that is concerned with the cathode layer on non-refractory cathodes are the works [ALM13] and [BEN15], which are concerned with vacuum arcs on chromium or chromium alloy cathodes. It is stated in [BEN15], that in the case of a chromium cathode, diffuse attachment can be realized, when the cathode is molten. Also it is stated that in these cases, the current should be dominated by ions diffusing to the cathode from the plasma bulk, as the cathode is too cold for the current by field-

enhanced thermionic emission, to be high enough. A sufficiently high level of electron temperature in the ionization layer is ensured by electron heat conduction from the bulk plasma. The analysis in [BEN15] for chromium cathodes is performed based on the model presented in [ALM13], but it is being generalized to “diffuse attachment”, by adopting the approach of ions diffusing to the cathode from the plasma, which leads to a higher ion current density, which reaches appropriate values for $T_w \approx 2000[K]$, while still monotonically rising with T_w , see Figure 13. The electron temperature was set as $T_e = 8000[K]$ and the pressure in the bulk plasma was set at $p = 1[mbar]$, creating conditions where the Cr vapor approaches full ionization. In contrast to that, also Gadolinium cathodes under the same condition are discussed, but there the current seems to be dominated by field-enhanced thermionic emission, because of the unusually low work function of Gadolinium.

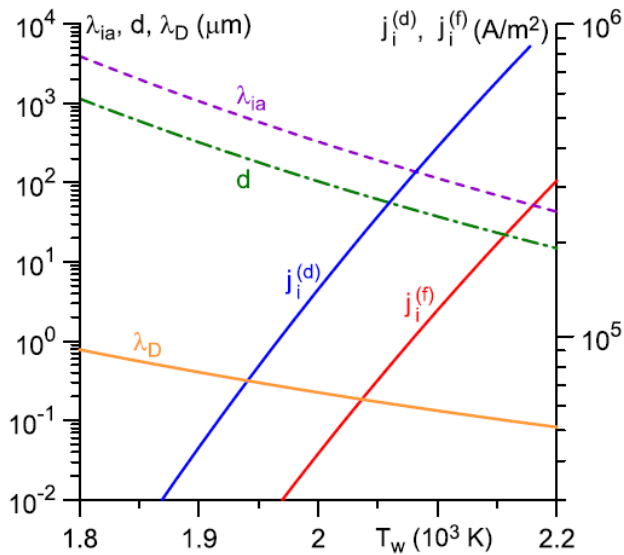


Figure 13: Ion saturation current for Cr-vapor plasma, $T_e = 8000[K]$, $j_i^{(d)}$: diffusion approach, $j_i^{(f)}$: multi-fluid approach; d : ionization length; λ_D : Debye-length; λ_{ia} : mean free path for collisions between ions and neutrals, from [BEN15]

Abbildung 13: Ionensättigungsstrom für Cr-Dampf-Plasma, $T_e = 8000[K]$, $j_i^{(d)}$: mit Diffusionsansatz, $j_i^{(f)}$: mit Multi-Fluid-Ansatz; d : Ionisationslänge; λ_D : Debye-Länge;

λ_{ia} : mittlere freie Weglänge für Kollisionen zwischen Ionen und Neutralen, aus [BEN15]

In contrast to [BEN15], the model of [ALM13] is concerned with “spot attachment”. It is stated there, that the potential in the sheath is modified due to atoms emitted from the cathode surface by evaporation, and therefore some of the ions generated in the ionization layer will scatter back to the plasma bulk, see Figure 14.

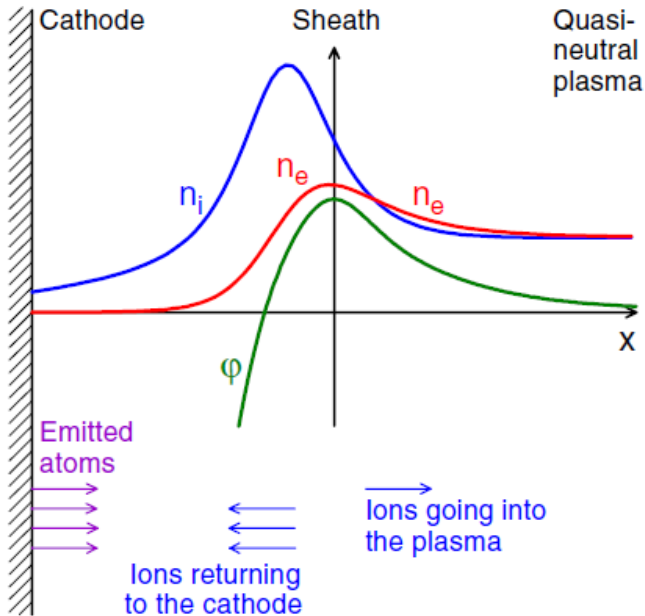


Figure 14: Schematic of the double sheath approach with ionisation of emitted atoms, from [BEN10]

Abbildung 14: Schematische Darstellung des Doppelschicht Ansatzes mit Ionisierung der emittierten Atome, aus [BEN10]

Here, it is considered that the flux of atoms, evaporated from the cathode surface is fully ionized. However, due to considerations in the microscale, about where in respect to the potential maximum the ionization occurs, a large part of the ions will be scattered back to the plasma bulk, thereby limiting the ion flux to the cathode, as indicated by the ion backflow coefficient in appendix B of [BEN10]. The energy balance of the electrons is satisfied, also taking into account energy transported back from the bulk

plasma to the sheath, by thermalized electrons from ionizations occurring after the maximum of the potential φ . As a result, one can determine the current density, see Figure 15 and the heat flux from the plasma to the cathode, see Figure 16. It should be noted, that the current density j is strongly monotonically rising with cathode surface temperature T_w and the heat flux q is positive for cathode surface temperature up to $T_w \approx 4400[K]$, where the current density $j \approx 10^{10} \left[\frac{A}{m^2} \right]$.

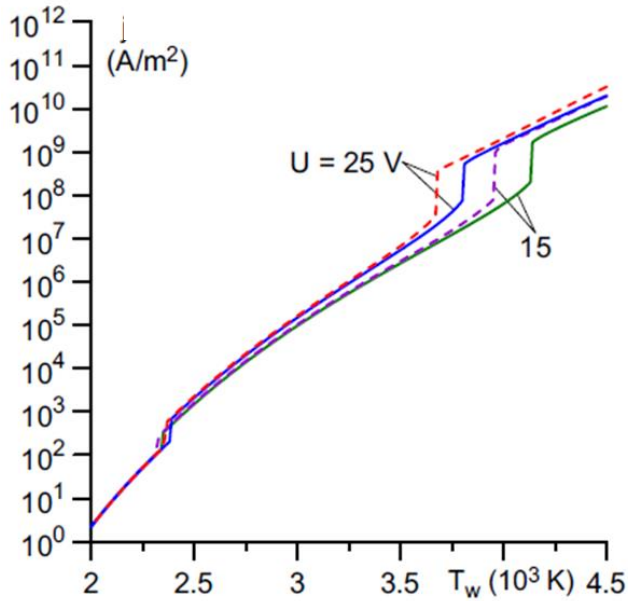


Figure 15: Electric current density j for Cu (solid) and Cr (dashed), for different cathode layer voltages, from [ALM13]

Abbildung 15: Elektrische Stromdichte j für Cu (durchgezogen) und Cr (gestrichelt), für verschiedene Kathodenschichtspannungen, aus [ALM13]

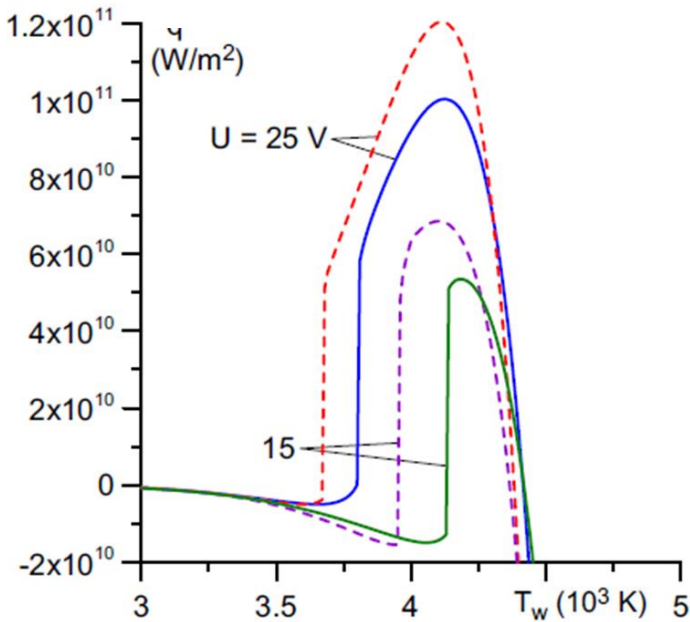


Figure 16: Heat flux from the plasma to the cathode q for Cu (solid) and Cr (dashed) cathode with different cathode layer voltages from [ALM13]

Abbildung 16: Wärmestromdichte q vom Plasma zur Kathode für Cu (durchgezogen) und Cr (gestrichelt) Kathoden mit unterschiedlichen Kathodenschichtspannungen aus [ALM13]

2.2.2.3 Model of Benilov (1993) for “spot attachment” in vacuum arc for copper cathodes

Finally, the work presented in [BEN93] should be discussed briefly, as the code which was used to calculate the heat flux to a copper cathode, presented in this paper, was provided by Prof. Benilov to the author during a research stay and was subsequently used as the starting point for the model developed in this thesis. The work [BEN93] contains intricate mathematical derivations about the existence and stability of axisymmetric stationary solutions for vacuum arc cathode spots, but their discussion exceeds the scope of this thesis and is therefore omitted. It is the first work of its kind,

to give the radius of the cathode spot in a vacuum arc on a copper cathode, in a self-consistent way.

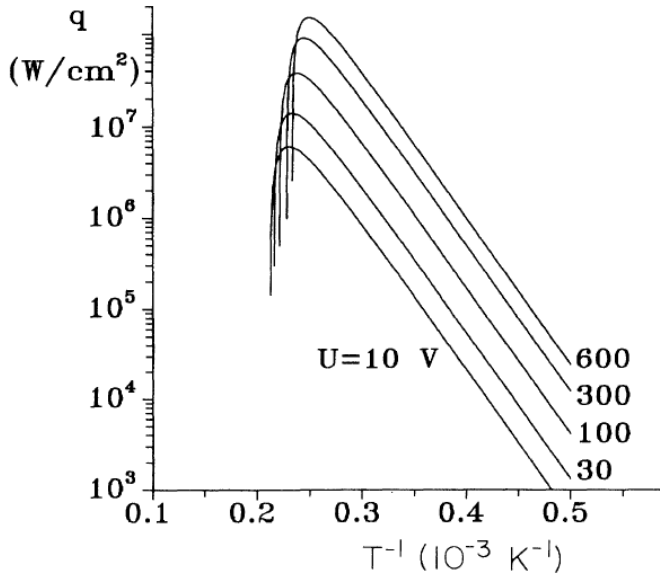


Figure 17: Heat flux as resulting for a copper cathode in a vacuum arc, in dependence of cathode layer voltage drop and inverse cathode surface temperature T_w^{-1} , from [BEN93]

Abbildung 17: Wärmestromdichte, wie er sich für eine Kupferkathode in einem Vakuumlichtbogen ergibt, in Abhängigkeit vom Kathodenschichtspannungsabfall und der inversen Kathodenoberflächentemperatur T_w^{-1} , aus [BEN93]

The heat flux to the cathode q for this model is expressed as

$$q = j_i \cdot (U + E_{ion} - A) - j_{em} \cdot A + \frac{H}{e \cdot N_A} \cdot (j_i - e \cdot J_{vap}) \quad (2)$$

Where j_i is the ion current density, j_e is the current density of the emitted electron (field-enhanced thermionic emission), U is the voltage drop over the cathode layer, E_{ion} is the first ionization energy of the cathode metal, A is the work function, H is the heat of vaporization, e is the elementary charge, N_A is the Avogadro constant and J_{vap} is the flux of evaporated atoms. It should be noted, that in this case the work function A is

used, instead of the effective work function A_{eff} , as was mistakenly used in Eq.(1), from [BEN95]. As becomes apparent only from the code, this approach is very simplified as it assumes complete ionization of all evaporated atoms and their full return to the cathode. Therefore, the ion current density is defined as

$$j_i = e \cdot n_{ion} \cdot v_{Bohm} \quad (3)$$

With $n_{ion} = \frac{N_L p_{vap} \cdot 273[K]}{T_{ion}}$, with N_L the Loschmidt number, p_{vap} the saturated vapor pressure on the cathode surface and the ion temperature equaling the temperature of the cathode surface $T_{ion} \approx T_w$.

The results for copper are displayed in Figure 17. It should be noted, that here the heat flux remains positive until a surface temperature of about $T_w \approx 4500[K] \triangleq T_w^{-1} \approx 0.22 \cdot 10^{-3} \left[\frac{1}{K} \right]$.

2.3 Discussion

The state of the art as presented here gives an overview over the models for the arc-cathode coupling currently used in GMAW welding simulation. Then, some of the most relevant works concerning the modelling of arc-cathode coupling in atmospheric arcs with a tungsten cathode are presented. Finally, the most relevant works for non-refractory cathodes, either for vacuum or atmospheric pressure arcs are summarized.

The analysis of the current state of GMAW welding simulation show, that currently no physically in-depth models for the arc-cathode coupling are realized and their level is much lower than the level of the models realized for the arc-cathode coupling in TIG welding. The heat flux is either given in a predefined Gaussian distribution or given in dependence of the plasma temperature, assuming simple heat conduction, or in dependence of the current density, which results from the current going through the electrode wire and the electrical conductivity in the plasma column. In none of these cases, the physics of the cathode layer region, as considered in the works for arc-cathode coupling with a tungsten cathode, is taken into account. Often it is stated that these simplifications were applied due to the relevant processes being poorly understood (e.g. [MUR11] or [XU09]).

The relevant works for the case of a tungsten cathode, as is the case in TIG welding, are mostly based on the ground-breaking work by Benilov and Marotta [BEN95], and

this is the reason why this work was examined in detail here, as well. The only work that stood out in this respect was the thesis by Kaddani, who used a model by Hsu [HSU83] and Delalondre [DEL90]. The thesis by Kaddani presented the only model that considered metal vapors. It is surprising for the model to consider tungsten vapor, in that respect, as the boiling temperature of tungsten is very high and evaporation is usually seen as a negligible effect in tungsten cathode arcs. However, all other models differ mainly from the models for “cold” cathodes, by not considering metal vapors, but instead they manage to describe the cathode boundary layer in a self-consistent way, while taking into account the deviation from LTE on the cathode boundary region. This was also necessary to ensure, that the electrical conductivity in the near-cathode regions of the numerical models would not drop to zero, as the temperature jump from the cathode to the plasma could not be resolved numerically due to limitations in the mesh resolution. In all approaches, the energy balance in the space charge sheath together with the ionization layer was seen as critical as well as current continuity, since it was necessary to enable the self-consistency. The self-consistency was even possible for a calculation without consideration of the plasma column, if the heat fluxes from the plasma column to the cathode layer were negligible [BEN95]. All approaches, except of the approach formulated by Kaddani used the Richardson-Dushman formula for thermionic emission or the Richardson-Schottky formula for field-enhanced thermionic emission, or even the Murphy-Good formalism for thermo-field emission. It was shown in [CAY08] and [BEN95], that the cathode sheath voltage drop was very sensitive to the boundary conditions at low plasma electron temperatures, ranging from $U_D \ll 1[V]$ for $T_w = 5000[K]$ to $U_D = 30[V]$ for $T_w = 3000[K]$. Also it was stated in [BEN95] that the ionization degree at the edge of the ionization layer needs to be larger than 0.6 in order to allow for a stable sheath. However, it should be definitely noted, that the cathode temperatures reached in these models are large, i.e. $T_w \gg 4000[K]$, see Figure 6, which is still possible for tungsten, but hardly achievable for non-refractory cathodes. However, in these models, such high temperatures are necessary, to allow for the thermionic or field-enhanced thermionic emission, to achieve the current densities that are observed in the experiment. Also, they do not consider evaporation to have any kind of influence on the processes. This leads to the characteristic feature of these types of models that the limitation of heat flux in dependence of the boiling temperature is always due heat losses by electron emission from the cathode, which requires high levels of electron emission. For non-refractory

cathodes, the heat losses by evaporation will be very strong for $T_w \gg T_{boiling}$, potentially becoming the limiting factor for the net heat flux to the cathode.

For the models for non-refractory cathodes, it is agreed that the mechanism of current transfer must be completely different from the one in the case of refractory cathodes. Here, two approaches are presented: one stating thermo-field emission in highly localized cathode spots, with high local pressures due to vaporization, as presented by Coulombe [COU97] or in [MOK20a]; and the second one considering the ionization of the metal vapor of a vacuum arc, either in spots [ALM13], or in a diffuse mode [BEN15], where the current is mostly carried by the ions. While the models of the spots require still a very high surface temperature, the model presented in [BEN15], which gives appropriate current densities for $T_w \approx 2000[K]$, does not give an explanation on how the flux of ions to the cathode would be limited for $T_w < T_{boiling}$. The model in [COU97], defines a criterion, that the flux of emitted electrons has to be larger than the flux of emitted ions. However, this criterion is only satisfied for vapor pressures at $T_w \gg T_{boiling}$, see Figure 9. Therefore, in case of a diffuse attachment of the arc to a “cold” cathode at atmospheric pressure, the criterion could never be valid for $T_w \leq T_{boiling}$. Also, this criterion does not hold for the conditions presented in [BEN15] of a non-emitting cathode, where the dominating carrier of current is the ion flux. Additionally, for all of the approaches, the range where the heat flux to the cathode is net positive $q \geq 0 \left[\frac{W}{m^2} \right]$, always extends far beyond boiling temperature, see Figure 11, Figure 16, Figure 17. This means in practice, that the cathode will be heated until the maximum temperature will be reached, which would mean the cathode surface would always be well beyond boiling temperature and heat losses by evaporation would always be significant. Another feature that all approaches share, is that the current density is always increasing monotonically with surface temperature T_w , see Figure 12, Figure 13, Figure 15. Finally, the last model discussed from [BEN93] considers the simplification of all evaporated particles to be ionized and all of them returning to the cathode. It should be noted that it is a strong simplification, which is revised in the authors newer works, i.e. [ALM13] and [BEN15]. However, in these works a certain fraction of these ions is assumed to be scattered towards the plasma bulk, due to a modification of the potential by the influence of the vaporized atoms. At this moment also the works of Lowke and Quartel [LOW97a] and Lowke, Morrow and Haidar [LOW97b] should be mentioned. There it was stated that thermal ionization or

photoionization will be most likely to generate the current in the cathode layer in non-refractory cathodes. Also, in the model in [BEN15] the assumption of electron generation due to thermal ionization in the bulk plasma was able to result in reasonable current densities, for diffuse attachment, when using sheath voltages of $U_D = 20[V]$.

3 Statement of the problem and goals

In order to reveal the link between the state of the theory and the conditions of the real welding experiments, this chapter includes two sections, one with experiments 3.1 and one with a dialectic argument concerning the responsible mechanism 3.2. From these considerations, the statement of the problem becomes apparent and it is offered in the conclusion 3.3. Finally this chapter is concluded with a statement on the intended goal of the work and the problem solving approach.

3.1 Preliminary welding experiments (high speed video recordings)

Before the model was developed, high-speed video recordings were obtained of the process, in order to capture the location of cathode spots, with similar camera setting as was the case in [LE 19]. The results were already published in [MOK20b]. The welding experiments were performed on a 6[mm] thick mild steel plate S235 with a roughly cleaned surface by wiping with ethanol. The power source was a EWM Alpha Q 551, and a synergy line was set, to match the conditions for spray transfer. The wire was a ESAB AristoRod 12.50, which is a G3Si1 wire, of 1.0[mm] diameter, the wire feed speed was $v_{wire} = 8[m/min]$. The contact tube to work piece distance was 11[mm], and the inclination of the torch was 0° . The shielding gas was 100% helium for one and Ferroline C8, which consists of 92% argon/8% carbondioxide, for the other line of trials. The gas flow rate was set to be sufficient, but not recorded. The camera was a Photron Fastcam SA4 (monochrome) and the recording speed ranged from 30.000fps at 320x320 pixels to 225.000fps at 128x64 pixels. The camera was equipped with several spectral filters as well as UV- and ND-filters (intensity filters). The aperture of the camera was 22 or 3.5 and the shutter time was between $1/30000[s]$ to $1/1000000[s]$. The camera was mounted to focus on a fixed spot below the fixed torch and the work piece was moved below the torch at constant welding speed $v_{weld} = \{40 \left[\frac{cm}{min} \right]; 60 \left[\frac{cm}{min} \right]; 90 \left[\frac{cm}{min} \right]\}$. No additional light source was used.

Current and voltage were recorded during the process. An examination of the weld seam was not performed, neither a recording of the width nor of the height, as the focus of interest was in the investigation of the mode and distribution of attachment of the arc to the weld pool.

3.1.1 Welding experiments with helium

Although the power source synergy lines did not provide a setting for helium shielding gas, trials were performed with a synergy line for argon shielding gas, in order to capture a visual recording of the cathode spot location. A typical recorded voltage and current is displayed in Figure 18, where many short circuit events can be seen.

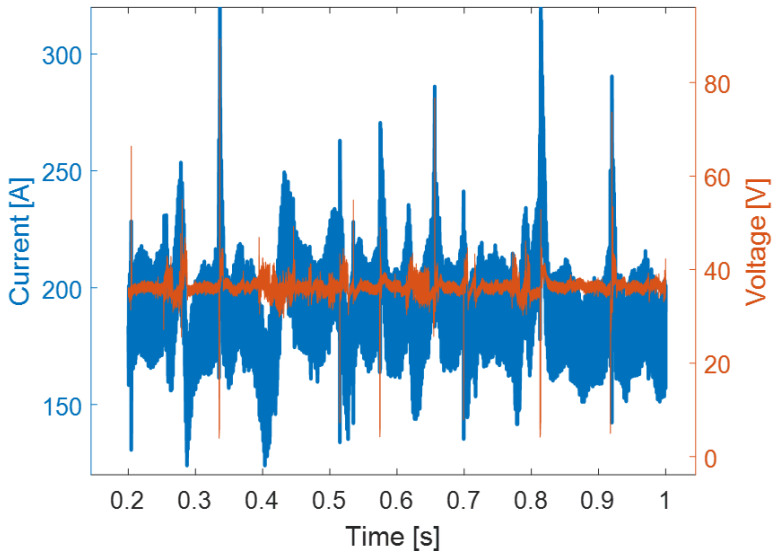


Figure 18: Transient Current-Voltage recordings for helium shielding gas, with $v_{weld} = 60 \left[\frac{cm}{min} \right]$. $U_{total,average} = 36[V]$, $I = 193[A]$

Abbildung 18: Strom-Spannungs-Verlauf für Helium-Schutzgas, bei $v_{weld} = 60 \left[\frac{cm}{min} \right]$. $U_{total,average} = 36[V]$, $I = 193[A]$

In the high speed video recordings two alternating regimes could be observed. One very stable mode of operation where cathode spots can be clearly identified on the melting front, see Figure 19. And an alternative mode of operation with a violent impact,

possibly boiling, on the melt pool surface, where no spots can be observed. A comparison between these two modes of attachment, recorded with a spectral filter to reduce the arc brightness, can be seen in Figure 20.

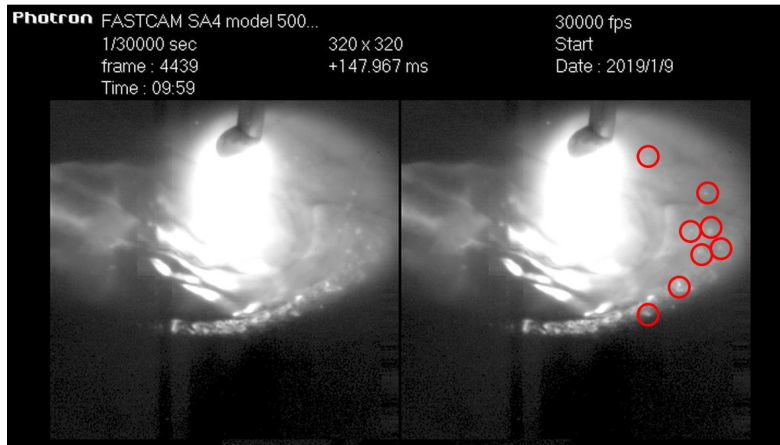


Figure 19: Identifiable cathode spots (marked with red circles on the right side) in helium, with $v_{weld} = 60 \left[\frac{cm}{min} \right]$. Aperture 22; UV+ND4 Filter. No spectral filter. 30000fps. 1/30000[s] shutter time. [MOK20b]

Abbildung 19: Identifizierbare Kathodenflecken (mit roten Kreisen auf der rechten Seite markiert) in Helium, mit $v_{weld} = 60 \left[\frac{cm}{min} \right]$. Blende 22; UV+ND4 Filter. Kein Spektralfilter. 30000fps. 1/30000[s] Verschlusszeit. [MOK20b]

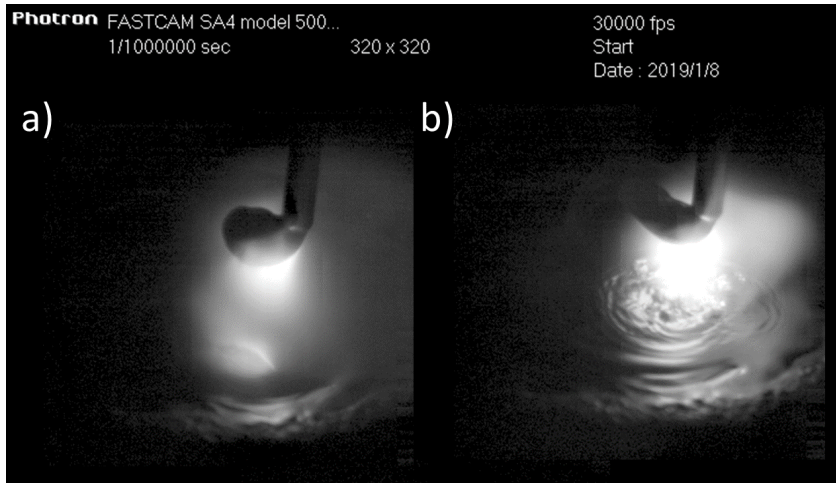


Figure 20: a) calm and smooth weld pool surface in the case with spot attachment, see Figure 19. b) rough weld pool surface at weld pool attachment. Shielding gas: helium, with $v_{weld} = 60 \left[\frac{cm}{min} \right]$. The arc is burning directly on the melt pool. Aperture 22; UV+ND4 Filter. 436nm spectral filter. 30000fps. $1/1000000[s]$ shutter time. [MOK20b]

Bild 20: a) ruhige und glatte Schmelzbadoberfläche im Fall mit Anbindung in kleinen Kathodenflecken (siehe Abbildung 19). b) raue Schmelzbadoberfläche bei einer Anbindung direkt auf dem Schmelzbad. Schutzgas: Helium, mit $v_{weld} = 60 \left[\frac{cm}{min} \right]$. Der Lichtbogen brennt direkt auf dem Schmelzbad. Blende 22; UV+ND4-Filter. 436nm-Spektralfilter. 30000fps. $1/1000000[s]$ Verschlusszeit. [MOK20b]

Another interesting observation could be made when the welding velocity was increased in this mode. At $v_{weld} = 90 \left[\frac{cm}{min} \right]$ the weld pool became very shallow, which allowed the shielding gas flow, to push back the liquid melt, until the still solid bottom of the melt pool was exposed, and to create “dry islands” in the middle of the melt pool, see Figure 21. These “dry islands” would exist as long as the arc was in “spot attachment” mode, but once the arc would start burning back on the weld pool, the roughed up molten metal would cover the dry island, until the mode of attachment would switch back and then the island could dry up again.

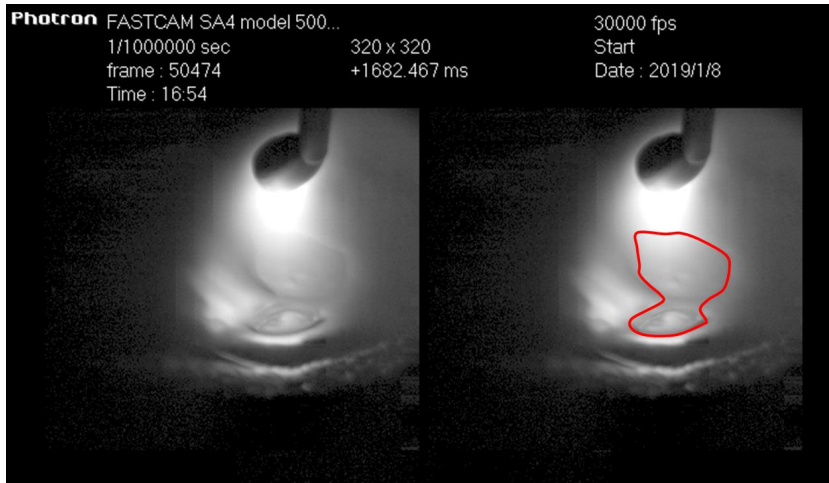


Figure 21: Appearance of dry islands (marked in red on the right side) in helium with $v_{\text{weld}} = 90 \left[\frac{\text{cm}}{\text{min}} \right]$, in the phase with “spot attachment”. Aperture 22, UV+ND4 Filter. 436nm spectral filter. 30000fps. $1/1000000[\text{s}]$ shutter time.

Abbildung 21: Auftreten trockener Inseln (auf der rechten Seite rot markiert) in Helium bei $v_{\text{weld}} = 90 \left[\frac{\text{cm}}{\text{min}} \right]$, in der Phase mit Anbindung in kleinen Kathodenflecken. Blende 22, UV+ND4 Filter. 436nm-Spektralfilter. 30000fps. $1/1000000[\text{s}]$ Verschlusszeit.

3.1.2 Welding experiments with Ar+8%CO₂

Several experiments with Ar+8%CO₂ shielding gas were performed. The process was quite stable, as the power source synergy line was set to match the conditions. The voltage and current recordings can be seen in Figure 22, where the process is running unsteady and the effect of the control by the power source can be seen in the strong periodic variation of the current.

However, in the experiments, no spots could be clearly identified. This was also the case with very short shutter times, any of the available filters (436nm, 650nm, 808nm, >900nm) or the highest recording rate of 225000fps. An exemplary recording is shown in Figure 23 and another one, recorded at a higher frame rate of 225000fps in Figure 24. There is a clearly observable “white zone” in Figure 23, which might indicate the activity of some spots, like oxide cleaning. However, the heating power of these low-

luminosity spots must be very low, as no significant melting can be observed. After discussing the recordings with the group of Prof. Benilov, it was agreed, that the attachment under these conditions was most likely “diffuse attachment”, and any occurrence of the spots would be most likely a fringe phenomenon, and only play a minor role in the transfer of current and heat.

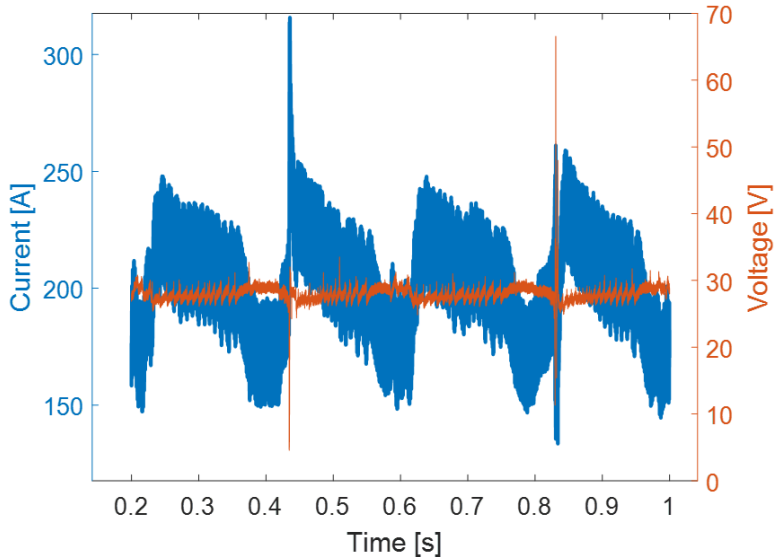


Figure 22: Transient Current-Voltage recordings for argon+8%CO₂ shielding gas, with $v_{weld} = 60 \frac{cm}{min}$. $U_{total,average} = 28[V]$, $I_{total,average} = 197[A]$

Abbildung 22: Strom-Spannungs-Verläufe für argon+8%CO₂-Schutzgas, bei $v_{weld} = 60 \frac{cm}{min}$. $U_{total,average} = 28[V]$, $I_{total,average} = 197[A]$

Another important observation of the weld pool is, that no boiling can be observed, as the weld pool in Figure 23 looks very smooth. The suppression of boiling could possibly be due to increased boiling temperature at the effect of the pressure of the arc (ions impinging onto the weld pool surface), but an estimation of the magnitude of this effect showed that the effect was negligible. So, even though no temperature measurements were performed in these trials, it can be concluded, that the weld pool surface temperature cannot be much higher than $T_{boiling}$.

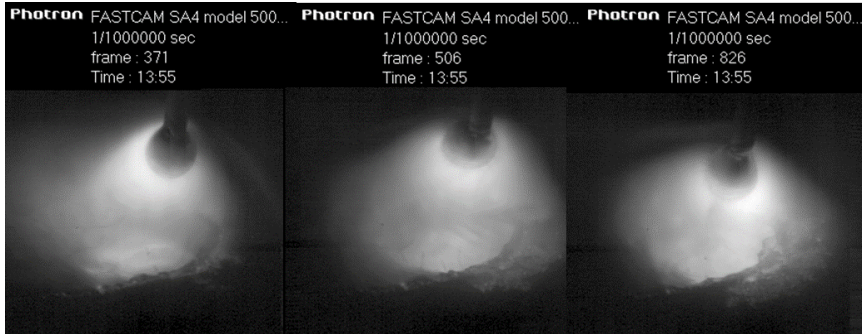


Figure 23: Three consecutive moments of the weld pool in Ar+8%CO₂ at $v_{weld} = 60 \left[\frac{cm}{min} \right]$. No spots are identifiable, but only an extending "white zone" ahead of the melting front. Aperture 22, UV+ND2 Filter. No spectral filter. 30000fps. 1/1000000[s] shutter time. [MOK20b]

Abbildung 23: Drei aufeinander folgende Momente des Schweißbades in Ar+8%CO₂ bei $v_{weld} = 60 \left[\frac{cm}{min} \right]$. Es sind keine einzelnen Kathodenflecken erkennbar, sondern nur eine sich ausdehnende "weiße Zone" vor der Schmelzfront. Blende 22, UV+ND2 Filter. Kein Spektralfilter. 30000fps. 1/1000000[s] Verschlusszeit. [MOK20b]

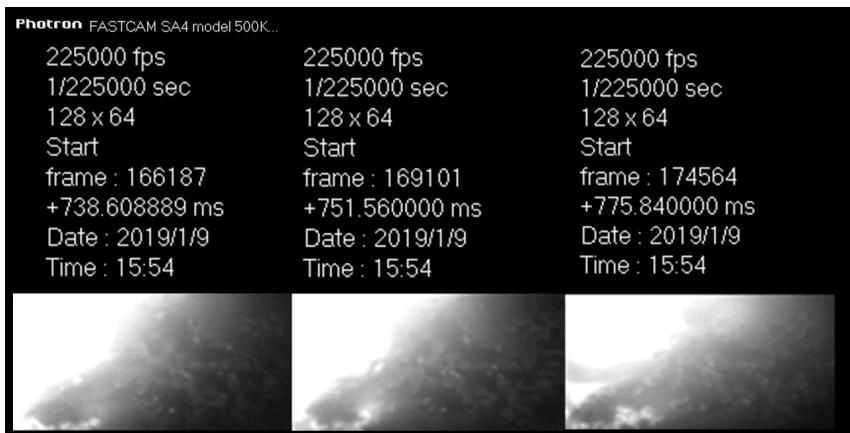


Figure 24: Three consecutive close-ups of the "white zone" in Ar+8%CO₂ at $v_{weld} = 60 \left[\frac{cm}{min} \right]$. Spots are not identifiable. Aperture 22, UV+ND2 Filter. No spectral filter. 225000fps. 1/225000[s] shutter time. [MOK20b]

Abbildung 24: Drei aufeinanderfolgende Nahaufnahmen der "weißen Zone" in Ar+8%CO₂ bei $v_{weld} = 60 \left[\frac{cm}{min} \right]$. Flecken sind nicht erkennbar. Blende 22, UV+ND2 Filter. Kein Spektralfilter. 225000fps. 1/225000[s] Verschlusszeit. [MOK20b]

3.2 Dialectic argument

Now, it can be concluded from the experiments, that under the investigated conditions, that means GMAW welding of steel with Ar+8%CO₂ shielding gas, the arc attachment is "diffuse" and that no boiling occurs. This means, that none of the available models for arc-cathode attachment, that were examined in 2.2. are applicable. As the attachment was diffuse, this allows a rough estimation of the occurring current densities and heat fluxes

$$j_{diffuse} = \frac{200[A]}{\pi \cdot (5[mm])^2} \approx 2.5 \cdot 10^6 \left[\frac{A}{m^2} \right] \quad (4)$$

$$q_{diffuse} = \frac{200[A] \cdot 20[V]}{\pi \cdot (5[mm])^2} \approx 5 \cdot 10^7 \left[\frac{W}{m^2} \right]$$

If we assume an almost even distribution of the current, half due to ions, we can estimate of the other half of the current could be accounted for by field-enhanced thermionic emission (Richardson-Schottky).

If $j_{ion} = 1.25 \cdot 10^6 \left[\frac{A}{m^2} \right]$, the electric field can be determined by the Mackeown formula (see Eq.(19)) and the resulting field-enhanced thermionic emission at $T_s = T_{boiling}$ can be evaluated, see Figure 25. It results in $j_{em} = 1.65 \cdot 10^6 \left[\frac{A}{m^2} \right]$, which is close to the estimated diffuse current density, which means that field enhanced thermionic emission and an equally scaled ion flux could be sufficient to account for the current density. However, the ratio $\frac{j_{ion}}{j_{em}}$ determines how much of the total current is turned over into heat.

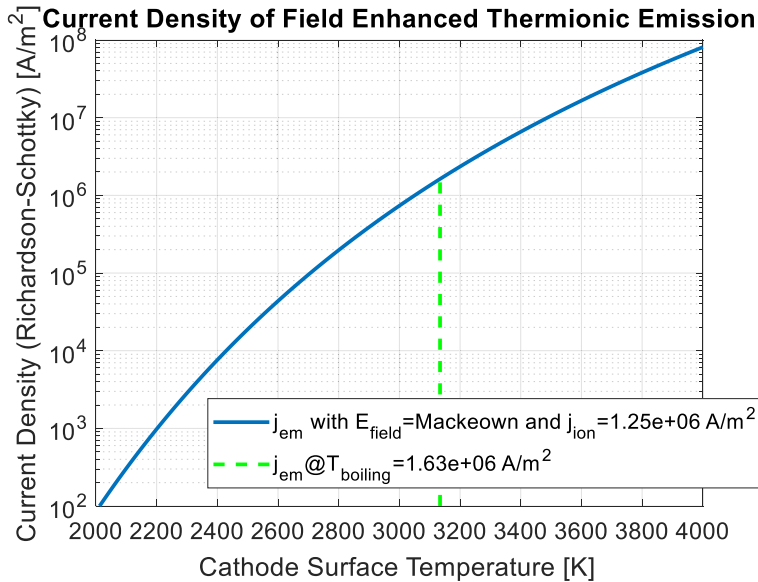


Figure 25: Current density due to field enhanced thermionic emission, with fixed ion current density j_{ion} for the Mackeown formula

Abbildung 25: Elektrische Stromdichte aufgrund feldverstärkter thermionischer Emission, mit fester Ionenstromdichte j_{ion} für die Mackeown-Formel, siehe Gleichung

In order to investigate the possible mechanisms of the generation of j_{ion} , in the following two hypotheses will be stated and consequently refuted in the style of a dialectic argument. The resulting synthesis will serve as a justification for the approach for the model of the arc-cathode coupling in GMAW, which is proposed in this thesis. The plots and graphics used to illustrate the argument were generated based on modifications of the model presented in 4.1.

3.2.1 Hypothesis 1: Ion flux due to evaporated atoms, ionized in the near-cathode plasma at constant temperature

3.2.1.1 Analysis

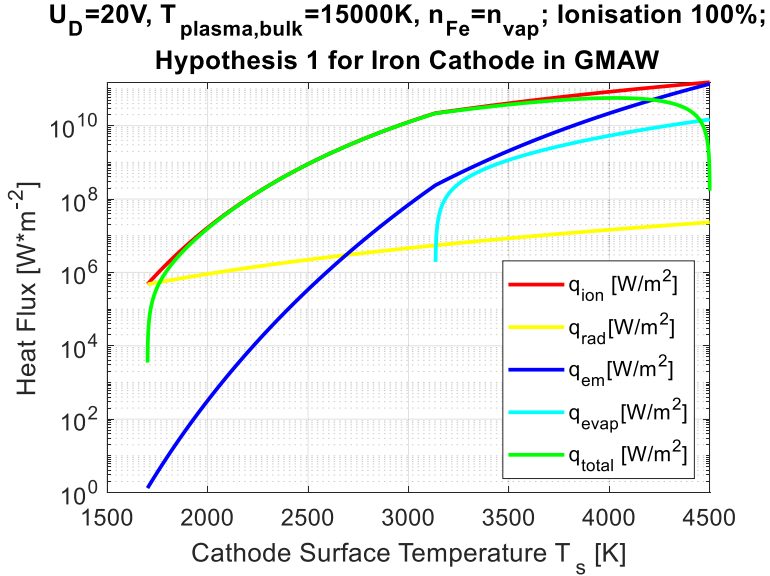


Figure 26: Heat fluxes according to the assumption of full ionization of the evaporated atoms and their return to the cathode

Abbildung 26: Wärmestromdichten unter der Annahme einer vollständigen Ionisierung der verdampften Atome und ihrer Rückkehr zur Kathode

Following the model used in [BEN93], it is assumed that the evaporated atoms from the cathode surface constitute the source of the ion flux. In a first approach it could be assumed that all evaporated atoms will be ionized (as would be the case for iron atoms at a plasma temperature $T_{\text{plasma}} = 15000[K]$) and that all ions would return to the surface. This corresponds to the equations (5)-(19) in 4.1.1, except for Eq.(14) where the local plasma temperature is set constant at $T_{\text{plasma,local}} = T_{\text{plasma}} = 15000[K]$, a temperature where almost all iron atoms are always ionized. The resulting heat fluxes are shown in Figure 26 and the resulting current densities in Figure 27.

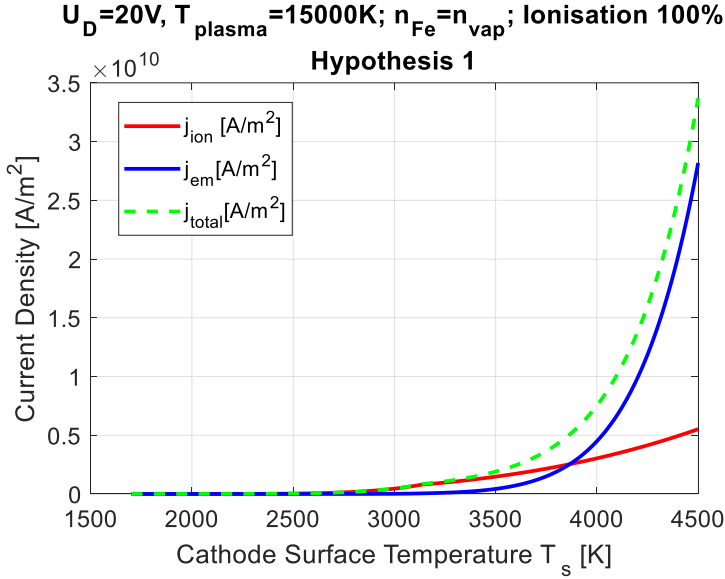


Figure 27: Current density according to the assumption of full ionization of the evaporated atoms and their return to the cathode

Abbildung 26: Elektrische Stromdichten unter der Annahme einer vollständigen Ionisierung der verdampften Atome und ihrer Rückkehr zur Kathode

This result shows, that the heat fluxes in this approach are very high and the maximal surface temperature, that still returns a positive heat flux is $T_{s,max}(q > 0) = 4500$ [K], which is the temperature to which the weld pool surface would heat up, theoretically. This is much larger than boiling temperature ($T_{\text{boiling}} = 3134$ [K]). The maximum heat flux is generated at $T_s(q_{max}) = 4026$ [K]. It can be also seen, that in this approach the heat flux is limited for higher surface temperatures mainly by the losses due to field-enhanced thermionic emission, as is the case for the models considering a tungsten cathode. Heat losses by evaporation play a minor role. Taking the current density at this temperature $T_{s,max}(q > 0) = 4500$ [K], and calculating from this the expected radius of arc attachment at a total current of $I = 200$ [A] results in $r_{HS} = 0.0435$ [mm]. It was attempted to calculate the distribution on the weld pool for these relationships, but the problem appeared numerically unstable and the attempt was given up.

However, as could be seen in 1.2.1, more recent studies of the GMAW arc indicate, that the plasma temperature in the arc column is colder, so that the attempt was made, to take into account the ionization degree, at a constant temperature plasma temperature of $T_{plasma} = 7000[K]$. The ionization degree was calculated due to the Saha equation, assuming LTE and it decreased at constant T_{plasma} , due to the strong increase of the density of evaporated iron atoms n_{vap} , see Figure 28. The noise at around $T_s \approx 500[K]$ is a numerical instability, due to the very low density of evaporated iron atoms.

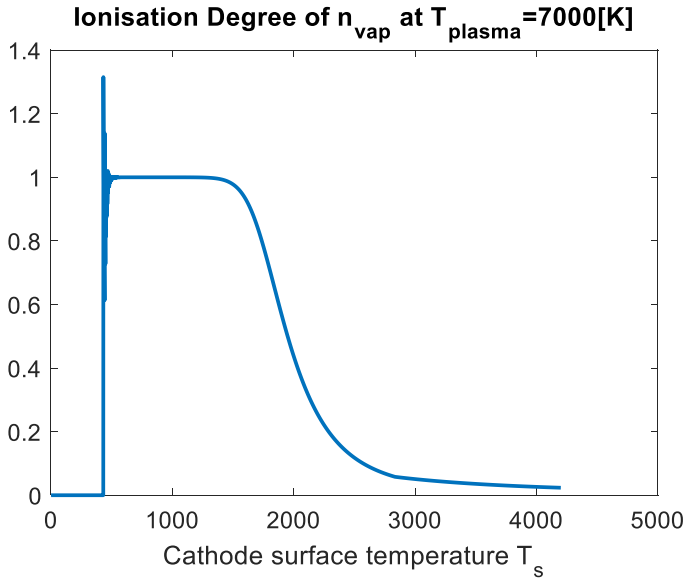


Figure 28: Ionization degree for the assumption that evaporated iron atoms are ionized at $T_{plasma} = 7000[K]$

Abbildung 28: Ionisationsgrad entsprechend der Annahme, dass bei dem verdampfte Eisenatome bei $T_{plasma} = 7000[K]$ ionisiert werden

When considering a lower plasma temperature, i.e. equations (5)-(19) in 4.1.1, except for Eq.(14) where the local plasma temperature is set constant at $T_{plasma,local} = T_{plasma} = 7000[K]$, the ionization degree of the iron atoms changes according to the iron atom density resulting from the saturated vapor density, as can be seen in Figure 28. The resulting heat fluxes can be seen in Figure 29, where the maximum surface

temperature decreased strongly to $T_{s,max}(q > 0) = 3460 \text{ [K]}$, and the heat losses by evaporation become the limiting mechanism for the heat flux at higher surface temperatures. It is for this reason, that the boiling temperature indicates the temperature of maximal heat flux $T_s(q_{max}) = T_{boiling}$.

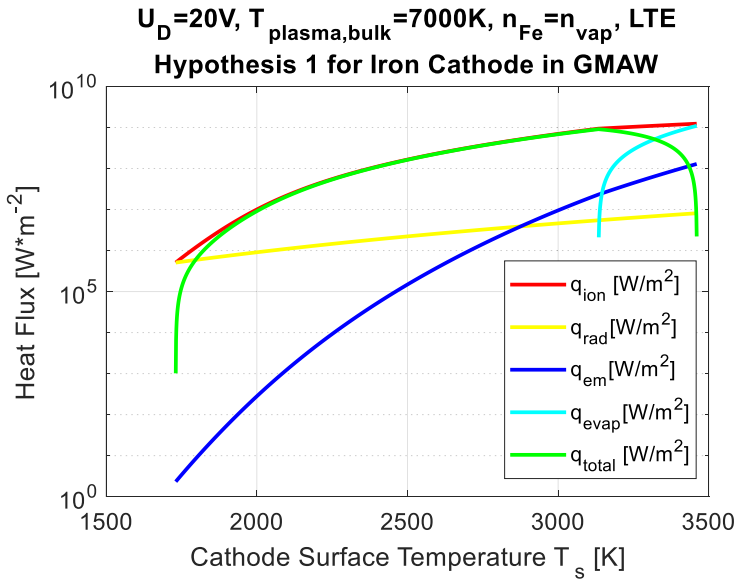


Figure 29: Heat flux to the cathode, assuming ionization of evaporated iron atoms in LTE at $T_{\text{plasma}} = 7000[K]$

Abbildung 29: Wärmestromdichte zur Kathode, unter der Annahme der Ionisierung von verdampften Eisenatomen im LTE bei $T_{\text{plasma}} = 7000[K]$

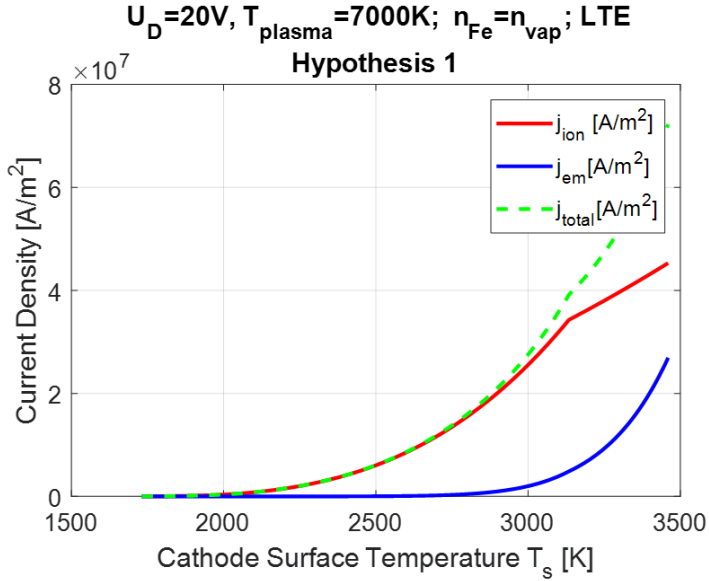


Figure 30: Current density to the cathode, assuming ionization of evaporated iron atoms in LTE at $T_{\text{plasma}} = 7000[K]$

Abbildung 30: Elektrische Stromdichte zur Kathode, unter der Annahme der Ionisierung von verdampften Eisenatomen im LTE bei $T_{\text{plasma}} = 7000[K]$

In Figure 31 an example surface temperature field for the same approach is shown, however in this case assuming $T_{\text{plasma,local}} = T_{\text{plasma}} = 6500[K]$ instead of Eq.(14), since for higher plasma temperatures the numerical simulation would become instable and break down. Here, a weld pool simulation as set in 5.1 was performed, where profile for the plasma temperature was applied, that was constant at T_{plasma} within the radius r_{HS} , and at $300[K]$ outside of the radius. It can be seen that the surface temperature is much higher than boiling temperature over a large area, leading to massive heat losses by evaporation. Another peculiarity is that, while the total heat supplied to the cathode is at a reasonable magnitude for this chosen radius $r_{HS} = 3[mm]$, the total current is much higher, than could be expected for the conditions of GMAW. This effect can be explained by the fact that, while for a large area (almost all within r_{HS}) T_s is very close to $T_{s,max}(q > 0)$, this area produces almost no net heat, because all of it is balanced by the losses due to evaporation. However, since the

current density is monotonically rising with T_s , see Figure 30, this means that a large amount of current is transferred, while no heat is provided to the cathode. This behavior for the current density is even stronger for the approach considering full ionization, see Figure 27.

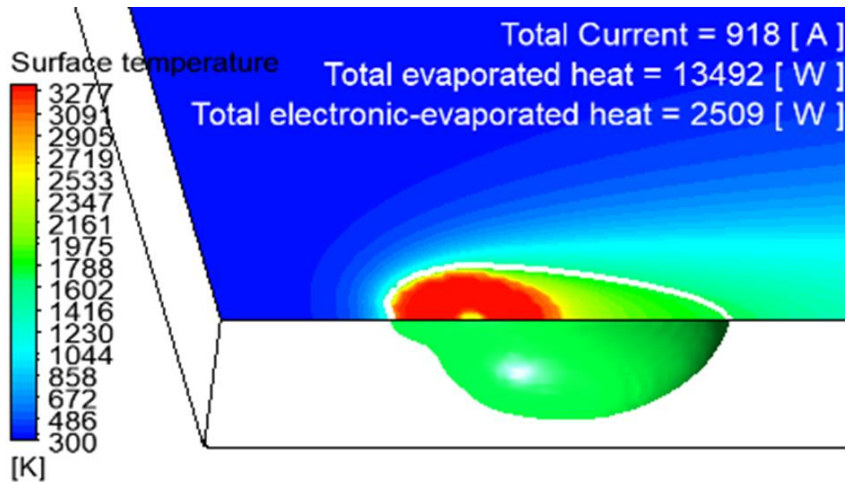


Figure 31: Hypothetical surface temperature of a weld pool calculation assuming ionization of evaporated atoms at $T_{plasma} = 6500[K]$. The current as well as the evaporation losses are unrealistically high.

Abbildung 31: Hypothetische Oberflächentemperatur einer Schmelzbadberechnung unter der Annahme der Ionisierung der verdampften Atome bei $T_{plasma} = 6500[K]$. Sowohl der elektrische Strom als auch die Verdampfungsverluste sind unrealistisch hoch.

3.2.1.2 Conclusions

The analysis of the approach, that the ion flux is due to ionization of the metal vapor at constant temperature shows that this approach needs to be refuted. Besides generating considerable heat fluxes at surface temperatures far above $T_{boiling}$, thereby causing extreme heat losses due to evaporation, the monotonically increasing current densities are of primary concern.

As can be easily followed from Figure 29, Figure 30 and Figure 31, any mechanism, which would allow for the current density to increase monotonically, will generate a

discrepancy between the total current transmitted and the heat supplied to the cathode. This discrepancy might be small, when the area at temperatures close to $T_{s,max}(q > 0)$ is small compared to the area with temperature close to $T_s(q_{max})$, but for larger diameters of the heat source (as is the case in “diffuse” attachment in GMAW), this discrepancy will become absolutely prohibitive. This monotonic increase of the current density is a feature which is common to every cathode layer model analyzed in 2.2., and in fact it will be a feature in every model that does not have a distinct maximum of the ion flux at $T_s < T_{boiling}$, since there is no mechanism to decrease the current transported by emitted electrons.

⇒ Therefore, it has to be concluded, that a working model for arc-cathode coupling in diffusely attached GMAW will need a distinct maximum of the ion flux at $T_s < T_{boiling}$.

3.2.2 Hypothesis 2: Ion flux due to constant metal vapor density in the plasma

3.2.2.1 Analysis

In the next hypothesis, it is assumed that the ions originate from a constant density of Fe atoms, which is present in the plasma, i.e. Eq. (5)–(19) with setting $n_{vap} = 0[m^{-3}]$ in Eq.(15) and therefore $n_{Fe} = n_0 = const$. The magnitude of such density can be taken from measurements, e.g. [KOZ13], where the Fe concentration has been measured in the metal vapor core $n_{Fe} \approx 2.5 \cdot 10^{22}[m^{-3}]$, $1[mm]$ above the cathode. Considering a constant plasma temperature of $T_{plasma} = 7000[K]$ and density, the ionization degree in LTE will be constant as well at ~ 0.43 .

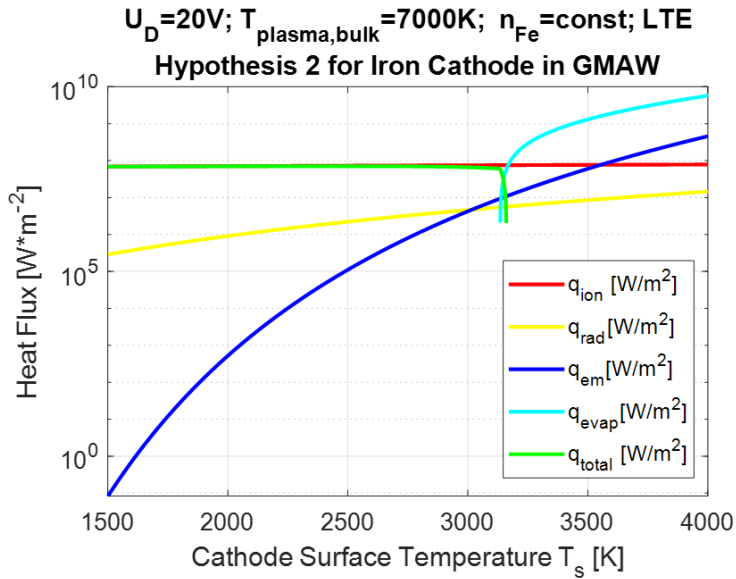


Figure 32: Heat flux to the cathode, assuming ionization of a constant density of iron atoms in LTE at $T_{\text{plasma}} = 7000[K]$

Abbildung 32: Wärmestromdichte zur Kathode unter der Annahme der Ionisation einer konstanten Dichte von Eisenatomen im LTE bei $T_{\text{plasma}} = 7000[K]$

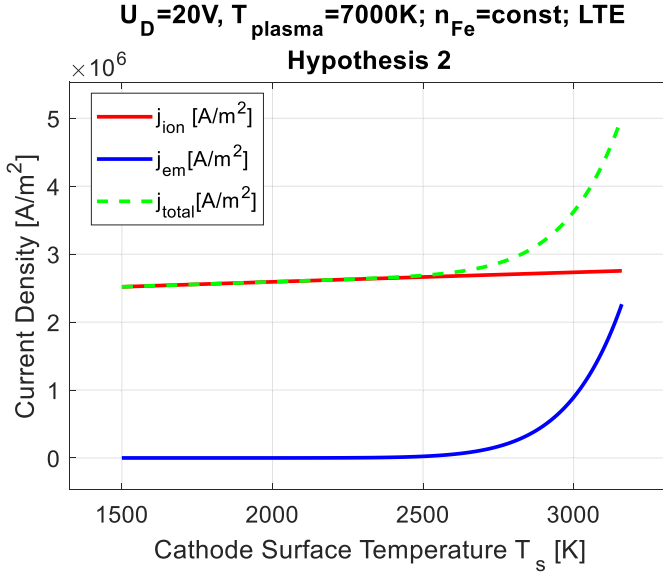


Figure 33: Current density to the cathode, assuming ionization of a constant density of iron atoms in LTE at $T_{\text{plasma}} = 7000[K]$

Abbildung 33: Stromdichte zur Kathode, unter der Annahme der Ionisation einer konstanten Dichte von Eisenatomen im LTE bei $T_{\text{plasma}} = 7000[K]$

It can be seen in Figure 32 that the heat losses by evaporation are the limiting mechanism for the heat flux at higher surface temperatures and the maximum surface temperature is limited to $T_{s,\text{max}}(q > 0) = 3160 [K]$. The temperature of the maximal heat flux is well below boiling temperature $T_s(q_{\text{max}}) = 2435[K] \ll T_{\text{boiling}}$. The current densities are again monotonically rising, see Figure 33, however at a much more moderate rate, in particular also when approaching $T_{s,\text{max}}(q > 0)$. In Figure 34 again a weld pool simulation as set in 5.1 was performed, where profile for the plasma temperature was applied, that was constant at T_{plasma} within the radius r_{HS} , and at $300[K]$ outside of the radius. It can be seen that the surface temperature seems not too unreasonable, as well as the total current in relation to the generated heat. Only the heat losses by evaporation seem a bit excessive, but not prohibitive.

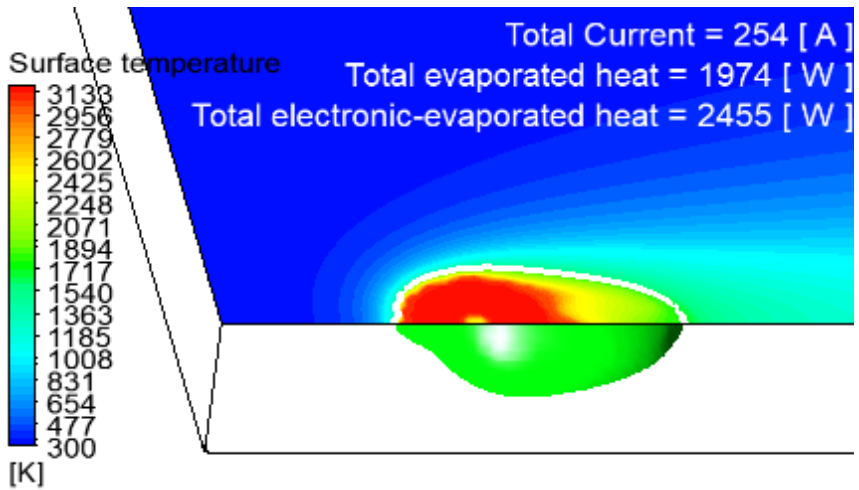


Figure 34: Hypothetical surface temperature of a weld pool calculation assuming ionization of a constant density of iron atoms in LTE at $T_{plasma} = 7000[K]$. Losses due to evaporation are significant.

Abbildung 34: Hypothetische Oberflächentemperatur einer Schmelzbadberechnung unter Annahme der Ionisation einer konstanten Dichte von Eisenatome im LTE bei $T_{plasma} = 7000[K]$. Die Verluste durch Verdampfung sind signifikant.

However, when looking at the saturated vapor densities in Figure 35, it becomes apparent, that for cathode surface temperatures $T_s > 2303[K]$, the atoms that vaporized from the cathode will become dominant and, within a certain proximity to the cathode, increase the iron atom density. Please note that in Figure 35 a semi-logarithmic scale is applied and that in fact, the influence of the iron vapor is much more dramatic than it appears in this depiction. This means, the iron vapor will have a strong influence on the iron atom concentration and that it cannot be simply neglected. The issue is the same for the ions, when assuming a constant temperature, see Figure 36, where it can be seen that the density of ions and therefore also the flux of ions increases almost exponentially, which is in contradiction with the conclusion of 3.2.1.2.

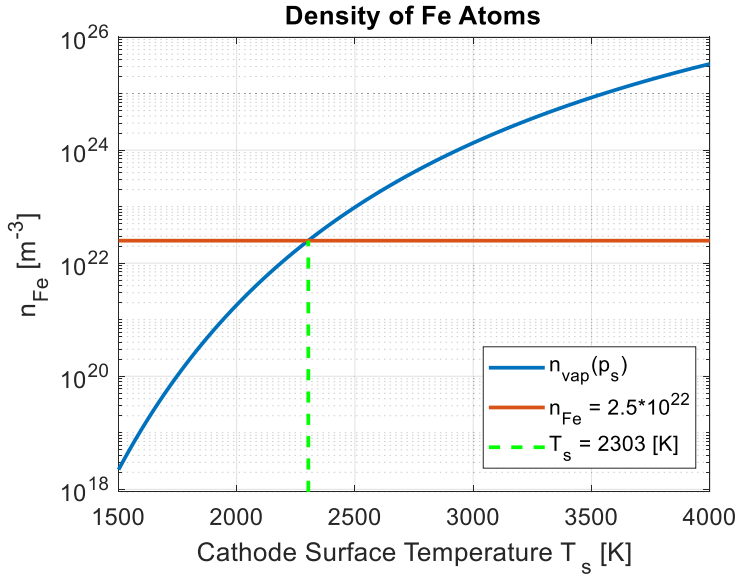


Figure 35: Saturated vapor density $n_{\text{vap}}(p_s)$ compared with the constant iron atom density $n_{\text{Fe}} = \text{const.}$

Abbildung 35: Sättigungsdampfdichte $n_{\text{vap}}(p_s)$ verglichen mit der konstanten Eisenatomdichte $n_{\text{Fe}} = \text{const.}$

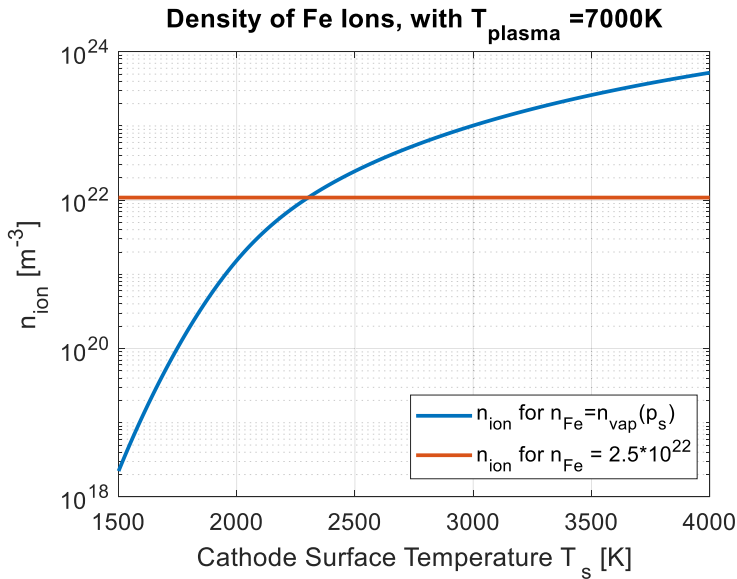


Figure 36: Comparison of ionized atoms at LTE with constant $T_{\text{plasma}} = 7000[\text{K}]$, once due to constant density and once due to saturated vapor pressure.

Abbildung 36: Vergleich der ionisierten Atome bei LTE konstantem $T_{\text{plasma}} = 7000[\text{K}]$, einmal aufgrund der konstanten Dichte und einmal aufgrund des Sättigungsdampfdrucks.

3.2.2.2 Conclusions

The analysis shows, that for an evaporating cathode, the iron atom density due to the saturated vapor pressure becomes dominant over the iron atom density of the plasma. At a constant plasma temperature, the same effect can be observed for the ion atoms. It is fair to assume, that the atom density due to the saturated vapor pressure will prevail over a distance of at least a few mean free paths for atom-atom collisions. Unfortunately, it could not be finally assessed with certainty that this region will include the complete cathode layer, but following the estimation in [BEN95], the length under similar conditions could be a few $100[\mu\text{m}]$, thereby including the complete cathode region (when the length scale of electron energy relaxation is estimated to be $\lambda_u \approx 100[\mu\text{m}]$).

- ⇒ Therefore it can be concluded, that the cathode layer will be most likely dominated by evaporated atoms for cathode surface temperatures $T_s > 2300[K]$

3.2.3 Synthesis: proposal of core hypothesis

The two conclusions, that were derived from the dialectic argument that was developed in the last two subchapters show, that for the explanation of the processes in the cathode layer, two opposing trends need to be reconciled. One requires a mechanism to strongly decrease the ion flux to the surface, while the other predicts a strong increase in the source material of the ions, namely the iron vapor atoms. Since the velocity of the ions to the cathode has a lower limit by the Bohm-velocity, the only possibility how this can be explained is by a decrease of the ionization degree, in close proximity to the cathode. As the ionization degree can be calculated with the assumption of LTE, depending on the plasma temperature, this thesis proposes the hypothesis, that

- the lowering of the plasma temperature in the close proximity of the cathode by cold metal vapor suppresses the flux of ions to the cathode in the conditions of diffuse attachment in GMAW.

3.3 Conclusion

The experiments, carried out as preliminary work for this thesis, indicated that the mode of attachment of the arc to the cathode in GMAW with the widely use shielding gas composition Ar+8%CO₂ is of a diffuse type, without boiling of the cathode surface. None of the currently existing theories of arc-cathode coupling are suitable to describe the prevailing physical conditions, in a satisfying and practically operational way. Therefore, there exists a demand for a model, that captures the relevant physical processes and relationships of the coupling between the arc with the cathode and the weld pool, in order to further our understanding of the economically highly important GMAW process. Following the theoretical consideration of a dialectic argument, two conflicting aspects of the description of the model were identified and a possible solution of the reconciliation of the conflict was proposed, that serves as the core hypothesis, presented in this thesis.

3.4 Goal of the work

The goal of this thesis is to further improve the understanding of the GMAW process by proposing a new model for the coupling between the arc and the cathode, under the conditions of diffuse attachment, as it was observed in experiments. The proposed model will build on previously published theoretical models and take into account recent findings about the structure of the plasma column in GMAW. Although it does not go into the same physical depth as previously published models from the domain of theoretical plasma physics, it presents a significant progress in terms of physical depth over the models currently used in welding process simulation. Therefore, the goal of this thesis is to contribute to the interdisciplinary mutual understanding between plasma physics and the field of welding research, which is dominated by the engineering sciences.

3.4.1 Problem solving approach

In order to realize the goals of the thesis, the GMAW process was studied experimentally, as well as on a theoretical basis. The conditions applying to the process were identified and the theoretical approaches for the treatment of similar conditions were analyzed. This analysis served as a foundation for the development of a new model, which was tailored to fit to the conditions observed in the experiments. Although, the small physical thickness of the cathode layer does not allow for a direct experimental validation of the proposed model, the author is of the firm conviction, that the presented theoretical argument, and the indirect support by the experiment, which shows no boiling of the weld pool surface, contains sufficient cogency for the consideration of the approach.

Over the course of this work, the findings and considerations were developed, presented and published within conferences covering the field of welding simulation as well as the field of plasma physics. The discussions with the experienced experts of each of their field contributed to further the understanding of the conditions and relevant mechanisms.

The following will present a detailed description of the model, an analysis of its properties, as well as an analysis of the effects of different welding parameters on the model's influence on weld pool formation.

4 Model description

4.1 Model for diffuse arc-cathode attachment

4.1.1 Theory of the model of the evaporation-determined arc cathode coupling (EDACC)

The proposed model of Evaporation-Determined Arc-Cathode Coupling (EDACC) is roughly based on the model for the cathode layer of atmospheric pressure arcs [BEN95], but in a simplified way, as it does not attempt to achieve self-consistency by solving the energy balance in the cathode layer. It assumes a significant energy contribution from the plasma bulk in the plasma column to the cathode layer, but the plasma column was not included in the modelling up until now, so the system is not considered to be energetically closed. Therefore, the structure of distinct layered zones of space charge sheath, ionization layer and LTE-bulk, is omitted and instead bulk properties over the whole layer are considered. In contrast to [BEN95], the model takes into account condensation and ionization of the evaporated metal following [BEN93], as well as radiation [BEN08]. The ionization of the evaporated metal allows for a stronger mechanism of electron emission, at temperatures, where the thermo-field emission can be largely neglected. However, the EDACC model, as already published in [MOK19] considers an additional mechanism to limit the process to cathode surface temperatures below boiling, by assuming a lowering of the ionization degree by a cooling of the local plasma temperature due to cold metal evaporation.

4.1.1.1 Heat fluxes

For the net heat flux q_{total} , ion heating q_{ion} , with losses due to field-enhanced thermionic emission q_{em} , evaporation q_{evap} and radiation q_{rad} are being considered.

$$q_{total} = q_{ion} - q_{em} - q_{vap} - q_{rad} \quad (5)$$

The heat flux due to the ion current density j_{ion} is composed of a contribution due to thermal energy $\frac{k_B T_e}{2}$ with k_B the Boltzmann constant and T_e the electron temperature, the energy gain by traveling through electric field characterized by the cathode voltage drop U_D with the elementary charge e , the ionization energy E_{ion} , as well as the condensation enthalpy H_{vap} per particle, which will be deposited on the surface subtracted by the work function of iron A , combining the approaches from [BEN95], [BEN93] and [BEN08].

$$q_{ion} = \frac{j_{ion}}{e} \cdot \left(\frac{k_B \cdot T_e}{2} + e \cdot U_D + E_{ion} + \frac{H_{vap}}{N_{Avogadro}} - A \right) \quad (6)$$

Here it is assumed that the ion temperature T_i roughly equals the cathode surface temperature T_s , $T_i \approx T_s$, so the contributions by the thermal ion energy deposited (found in [BEN95]) cancels with the energy required to heat the particle to the temperature of the surface. While the ion temperature will be somewhat higher than the surface temperature, this assumption will have a minor influence on the result.

The heat losses due to field-enhanced thermionic electron emission current density j_{em} are composed of a thermal contribution $2 \cdot k_B \cdot T_s$ as well as the required work function A to release the electron from the electrode surface. [BEN95]

$$q_{em} = \frac{j_{em}}{e} \cdot (2 \cdot k_B \cdot T_s + A) \quad (7)$$

It is noteworthy that in Eq. (6) and (7) the actual work function is used instead of the effective work function which is used in [BEN95], as the effective work function should be only used for the calculation of the field-enhanced thermionic electron emission in the Richardson-Schottky formula, see Eq. (18) .

The heat losses by evaporation are taken as

$$q_{vap} = \frac{J_{vap} \cdot H_{vap}}{M_{Fe}} \quad (8)$$

following [MUR10], where J_{vap} is the evaporated net mass flux, H_{vap} is the molar heat of vaporization, which equals the enthalpy of condensation from Eq. (6) and M_{Fe} is the molar mass of iron. However, for $T_s < T_{boiling}$ the net flux $J_{vap} = 0$, because saturated evaporation conditions are assumed (i.e. as many particles are leaving the surface as are being scattered back to the surface from the vapor phase). For surface temperatures exceeding boiling temperature it is given as

$$J_{vap} = \rho_k \cdot u_k \quad (9)$$

with ρ_k the mass density at the edge of the Knudsen layer and u_k the bulk velocity of the vapor jet at the edge of the Knudsen layer, according to the model of [KNI79], see Appendix A. Please note, that this does not mean, that no evaporation occurs, only that the heat losses due to evaporation are negligible and become only significant when convective evaporation, i.e. boiling occurs. Of course, in reality the conditions are not fully saturated, even below boiling temperature. Instead it is expected that a

metal vapor “cushion” will build up in close proximity to the cathode, whose thickness and saturation will depend on the diffusion and convection in the close proximity of the surface. However, since these conditions are difficult to determine and since the heat losses due to evaporation are expected to be minor in relation to the heat balance below boiling temperature, this simplification seems to be justified.

Losses by radiation are described as

$$q_{rad} = \varepsilon \sigma \cdot T_s^4 \quad (10)$$

which is the Stefan-Boltzmann law, following [BEN08], with $\varepsilon \sigma$ being the Stefan-Boltzmann constant. Heating by radiation from the arc was neglected, following a reasoning from [ZHU92].

For the evaluation of these heat fluxes, the ion current density j_{ion} , the field-enhanced thermionic electron emission current density j_{em} are required.

4.1.1.2 Electrical current densities

The total current density is calculated as

$$j_{total} = j_{ion} + j_{em} \quad (11)$$

With j_{em} being the field-enhanced thermionic electron emission and j_{ion} being the current density due to ionized vapor atoms, where it is assumed that each evaporated atom that will be ionized moves back to the cathode surface (j_{ion}) and also releases an electron, which constitutes the main current generation mechanism in this model.

The ion current density j_{ion} is stated as

$$j_{ion} = e \cdot c_{ion} \cdot n_{ion} \quad (12)$$

where it is assumed that all ionized atoms return to the surface, with the ion speed of sound c_{ion} and the ion density n_{ion}

$$c_{ion} = \sqrt{\gamma \frac{k_B \cdot (T_{plasma,local} + T_i)}{m_{Fe}}} \text{ for } T_s \leq T_{boiling} \quad (13)$$

$$c_{ion} = \frac{u_k}{2} \left(\sqrt{1 + 4\gamma \frac{k_B \cdot (T_{plasma,local} + T_k)}{u_k^2 \cdot m_{Fe}}} - 1 \right) \text{ for } T_s > T_{boiling}$$

Where the ion speed of sound for $T_s \leq T_{boiling}$ is taken as the well known Bohm velocity, and for the condition of $T_s > T_{boiling}$ the ion speed of sound is taken from

[KRI10a], taking into account only one ion species. Here u_k and T_k are the velocity and temperature at the edge of the Knudsen-layer, derived from [KNI79], see Appendix A. Again it is assumed that $T_i = T_s$, $\gamma = 5/3$ is the ratio of the specific heats for monatomic gas and m_{Fe} is the atomic mass of iron. Here, the situation is simplified in such way, that it is assumed that the temperature of the atoms and the ions will be also taken on by the electrons, i.e. $T_{plasma,local} \approx T_e$, which corresponds to the assumption of LTE. This assumption is necessary, as the Saha equation, even the 2T-Saha equation see [VAN89], is mainly dependent on the electron temperature T_e . The temperature $T_{plasma,local}$ in the close vicinity of the cathode is approximated as a weighted arithmetic mean of the temperature of the plasma bulk $T_{plasma,bulk}$, i.e. the conditions in the arc column and the temperature of the metal vapor at the edge of the Knudsen layer T_{vap} (see Eq.(15) and Appendix A). They are weighted by their respective particle densities, i.e. the particle density of the plasma bulk $n_{plasma,bulk}$ which is assumed to be constant, see Eq. (16) and the density of the saturated metal vapor at the Knudsen edge n_{vap} which is exponentially increasing with increasing surface temperature T_s , see Eq. (15).

$$T_{plasma,local} = \frac{n_{vap} \cdot T_{vap} + n_{plasma,bulk} \cdot T_{plasma,bulk}}{n_{vap} + n_{plasma,bulk}} \quad (14)$$

Here n_{vap} is the saturated vapor atom density, determined by the Clausius-Clayperon equation

$$n_{vap} = \frac{p_{atm}}{k_B \cdot T_s} \cdot \exp\left(\frac{H_{vap}}{R} \cdot \left(\frac{1}{T_{boiling}} - \frac{1}{T_s}\right)\right); T_{vap} = T_s \text{ for } T_s \leq T_{boiling} \quad (15)$$

$$n_{vap} = n_k; T_{vap} = T_k \text{ for } T_s > T_{boiling}$$

With n_k the vapor density at the edge of the Knudsen-layer, from [KNI79], see Appendix A Eq.(31), p_{atm} atmospheric pressure, R ideal gas constant and $T_{boiling} = 3134$ [K] the boiling temperature at normal pressure of iron and

$$n_{plasma,bulk} = \frac{p_{atm}}{k_B \cdot T_{plasma,bulk}} \quad (16)$$

the bulk plasma atom density, following from the ideal gas law.

n_{ion} is the density of the ions in the vicinity of the cathode, as determined with $n_{ion} = n_e$ by the Saha equation reduced to the contribution of singly ionized metal vapor, while local thermodynamic equilibrium (LTE) is assumed.

$$\frac{n_e^2}{n_{Fe}} = \frac{2 \cdot Z_{Fe+}}{Z_{Fe}} \cdot \frac{(2\pi \cdot m_e \cdot k_B \cdot T_{plasma,local})^{\frac{3}{2}}}{h^3} \cdot \exp\left(-\frac{E_{ion}}{k_B \cdot T_{plasma,local}}\right) \quad (17)$$

with $E_{ion} = 7.9$ [eV] being the first ionization energy of iron, m_e being the electron mass and h being the Planck constant, while $n_{Fe} = n_{vap} + n_0$, considering the density of the iron atoms that will be ionized as constituted by the metal atom density arising from the bulk plasma (i.e. plasma column), here set to $n_0 = 2.5 \cdot 10^{22}$ [m⁻³], and at higher surface temperatures increasing by the evaporated iron atoms n_{vap} . This influence on the ion density is shown in Figure 37. Z_{Fe+} and Z_{Fe} are the partition functions for singly ionized and neutral iron atoms for the electron temperature $T_e \approx T_{plasma,local}$. The partition functions were taken from [KRA], by evaluating at discrete steps of T_e for a range of 4000[K] – 20000[K] and then interpolating the resulting values.

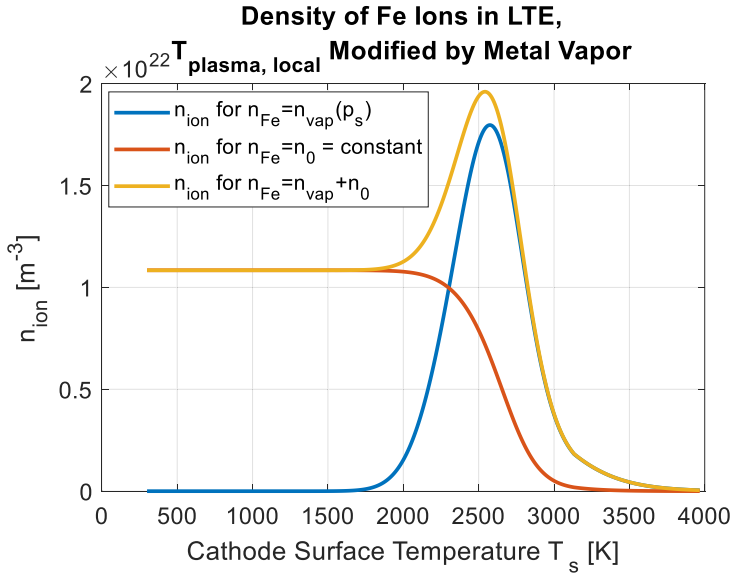


Figure 37: The ion density in LTE for $T_{plasma,local}$ modified by metal vapor according to Eq.(14), assuming $T_{plasma,bulk} = 7000$ [K], showing the behavior when considering only ionization of atoms from vapor or from the plasma bulk, and their combined influence.

Abbildung 37: Die Ionendichte in LTE für $T_{\text{plasma,local}}$ modifiziert durch Metaldampf gemäß Gl.(14), unter der Annahme, dass $T_{\text{plasma,bulk}} = 7000[\text{K}]$, zeigt das Verhalten, wenn man nur die Ionisation von Atomen aus der Verdampfung oder nur aus dem Plasmahintergrund oder ihren kombinierten Einfluss betrachtet.

The field-enhanced thermionic electron emission current density is calculated as

$$j_{em} = \frac{e \cdot 4 \cdot \pi \cdot k_B \cdot m_e}{h^3} \cdot T_s^2 \cdot \exp\left(-\frac{A_{eff}}{k_B \cdot T_s}\right) \quad (18)$$

which is the well-known Richardson-Schottky formula, $A_{eff} = A - \Delta A$ is the effective work function, with $A = 4.5 [\text{eV}]$ and $\Delta A = e \sqrt{\frac{e \cdot E_f}{4 \cdot \pi \cdot \epsilon_0}}$ the lowering of the work function from [PEK17] and

$$E_f = \left(\frac{8 \cdot m_{Fe} \cdot j_{ion}^2 \cdot U_D}{e \cdot \epsilon_0} \right)^{\frac{1}{4}} \quad (19)$$

the Mackeown formula for the electric field according to [BEN95] and ϵ_0 the vacuum permittivity.

4.1.2 Results of the model for the evaporation-determined arc-cathode coupling

The model presented in 4.1.1 is able to predict the heat flux $q_{total}(U_D, T_s, T_{\text{plasma,bulk}}, n_{\text{plasma,bulk}})$ and the electrical current density $j_{total}(U_D, T_s, T_{\text{plasma,bulk}}, n_{\text{plasma,bulk}})$ in terms of the cathode voltage drop U_D , the cathode surface temperature T_s , the plasma temperature of the plasma bulk $T_{\text{plasma,bulk}}$ and the metal atom density in vicinity of the cathode coming from the plasma column and n_0 . In the following the resulting properties of the established relations are thoroughly examined, assuming $n_0 = 2.5 \cdot 10^{22} [\text{m}^{-3}]$ taken from [KOZ13]. For simplification the value of n_0 is assumed as constant, while in reality the value will be dependent on the conditions of the arc (like temperature or gas flow conditions) and the evaporation at the anode.

4.1.2.1 Composition of the heat flux and dominating mechanisms

Figure 38 shows the resulting heat flux in dependence of the cathode surface temperature T_s , assuming a bulk plasma temperature of $T_{plasma,bulk} = 7000[K]$, which would be typical for the metal vapor core in the arc column in GMAW, see e.g. [NOM17] and a cathode voltage drop of $U_D = 17[V]$. Here, the surface temperature of the maximum heat flux $T_s(q_{max}) = 2533[K]$ and the maximum temperature of a positive net heat flux $T_{s,max}(q > 0) = 3111[K]$. The maximum heat flux in these condition is $q_{max} = 1.12 \cdot 10^8 \left[\frac{W}{m^2} \right]$. Under these conditions, no boiling occurs ($q_{vap} = 0 \forall T_s(q > 0)$), so q_{vap} is not shown in Figure 38) and the total heat flux q_{total} is mainly limited by the heat losses due to field-enhanced thermionic emission q_{em} . However, it is apparent that the main limitation on the total heat flux is the reduction of the ion heat flux q_{ion} following the decrease in the ionization degree of the local plasma due to the local cooling by the metal vapor.

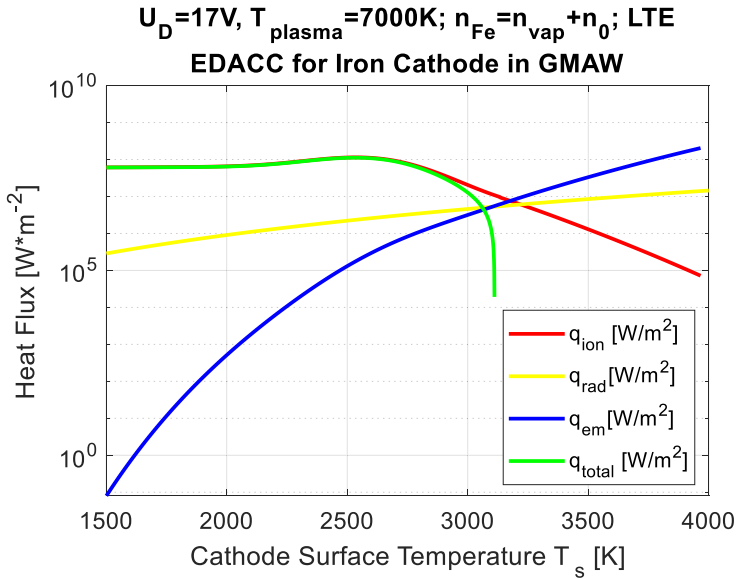


Figure 38: Heat flux according to the model presented in 4.1.1, with $U_D = 17[V]$ and $T_{plasma,bulk} = 7000[K]$

Abbildung 38: Wärmestromdichte nach dem in 4.1.1 vorgestellten Modell, mit $U_D = 17[V]$ und $T_{plasma,bulk} = 7000[K]$

Figure 39 shows the resulting heat flux in dependence of the cathode surface temperature T_s , assuming a bulk plasma temperature of $T_{plasma,bulk} = 12000[K]$, which would be typical for the arc column in GMAW close to the cathode outside the metal vapor core, see e.g. [KOZ13] for the measurement 1[mm] above the cathode, and a cathode voltage drop of $U_D = 17[V]$. Here, the surface temperature of the maximum heat flux $T_s(q_{max}) = 2657[K]$ and the maximum temperature of a positive net heat flux $T_{s,max}(q > 0) = 3144[K]$. The maximum heat flux in these condition is $q_{max} = 1.13 \cdot 10^9 \left[\frac{W}{m^2} \right]$. Under these conditions, boiling does occur and the total heat flux q_{total} is limited by the heat losses due to evaporation q_{vap} . However, it is apparent that the main limitation on the total heat flux is again the reduction of the ion heat flux q_{ion} following the decrease in the ionization degree of the local plasma due to the local cooling by the metal vapor.

It should be noted from Figure 38 and Figure 39, that the model in the current state, does not give a lower boundary for the $T_s(q > 0)$, that means, due to the constant supply of ions from the plasma, heating is ensured, even for cathodes at room temperature.

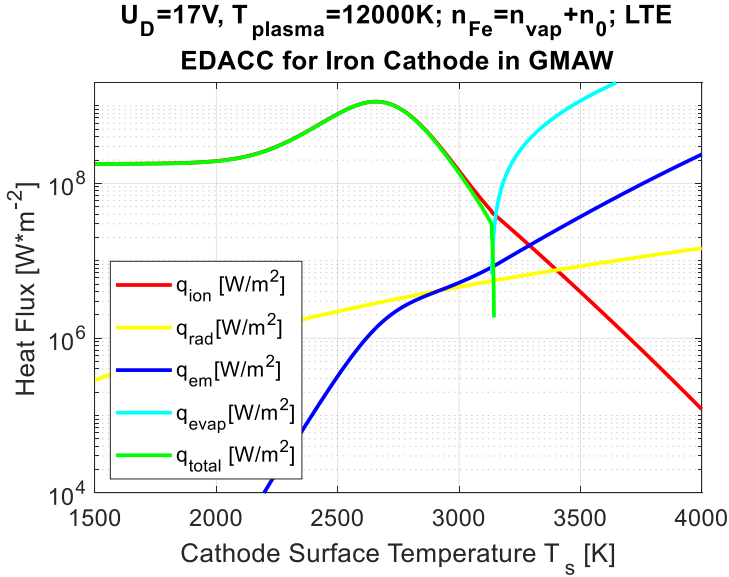


Figure 39: Heat flux according to the model presented in 4.1.1, with $U_D = 17[V]$ and $T_{\text{plasma,bulk}} = 12000[K]$

Abbildung 39: Wärmestromdichte nach dem in 4.1.1 vorgestellten Modell, mit $U_D = 17[V]$ und $T_{\text{plasma,bulk}} = 12000[K]$

In Figure 40 a comparison of the current density due to ions and the current density due to field-enhanced thermionic emission, for $T_{\text{plasma,bulk}} = 7000[K]$ and $U_D = 17[V]$, is shown. It can be seen that the current transfer due to field-enhanced thermionic emission becomes dominant for $T_s > 3022[K]$.

In Figure 41 the ionization degree is shown when assuming a temperature of the plasma bulk of $T_{\text{plasma,bulk}} = 7000[K]$. It should be noted, that the local ionization degree decreases strongly for $T_s > 2500[K]$, due to the strong cooling of the local plasma by cold metal vapor, which is displayed in Figure 42.

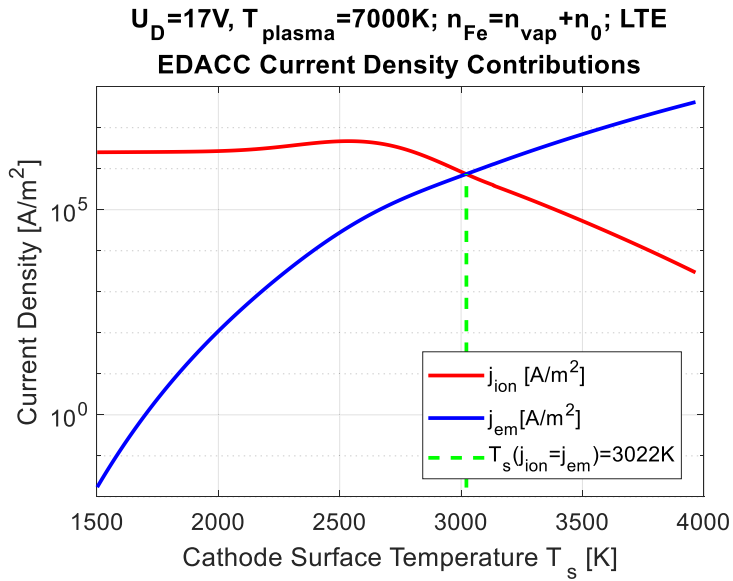


Figure 40: Comparison of current density due to ions and due to field-enhanced thermionic emission

Abbildung 40: Vergleich der elektrischen Stromdichte aufgrund von Ionen und aufgrund von feldverstärkter thermionischer Emission

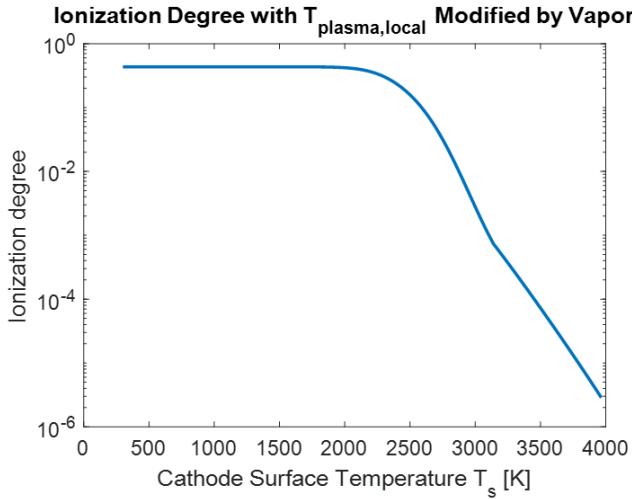


Figure 41: ionization degree according to the model presented in 4.1.1, with $T_{\text{plasma,bulk}} = 7000[\text{K}]$

Abbildung 41: Ionisationsgrad nach dem in 4.1.1 vorgestellten Modell, mit $T_{\text{plasma,bulk}} = 7000[\text{K}]$

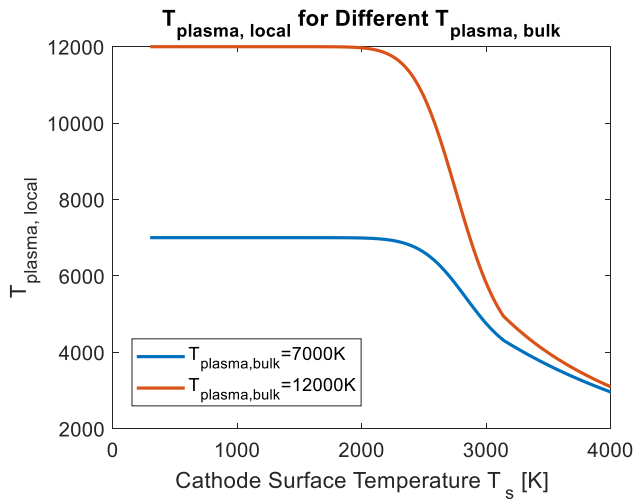


Figure 42: $T_{\text{plasma,local}}$ for different $T_{\text{plasma,bulk}}$

Abbildung 42: $T_{\text{plasma,local}}$ für verschiedene $T_{\text{plasma,bulk}}$

4.1.2.2 Dependence of the heat flux and current density on $T_{\text{plasma,bulk}}$

The dependence of the heat flux and current density on the $T_{\text{plasma,bulk}}$ is examined in Figure 43 and Figure 44. It can be seen that the maximum of heat flux and current density to the cathode is very sensitive to the temperature of the plasma bulk. However, the surface temperature where the maximum heat flux occurs $T_s(q_{\text{max}})$ varies only a little. It can be also seen from Figure 43, that for $T_{\text{plasma,bulk}} = 9500[\text{K}]$ and $T_{\text{plasma,bulk}} = 12000[\text{K}]$, the limitation of the heat flux occurs due to evaporation, since the heat flux decreases sharply for cathode surface temperatures $T_s > T_{\text{boiling}} = 3134[\text{K}]$. For the current density it can be seen from Figure 44, that the current density does not decrease to zero for $T_{s,\text{max}}(q > 0)$. It should be noted that there exists a distinct maximum of j_{total} for $T_s < T_{\text{boiling}}$.

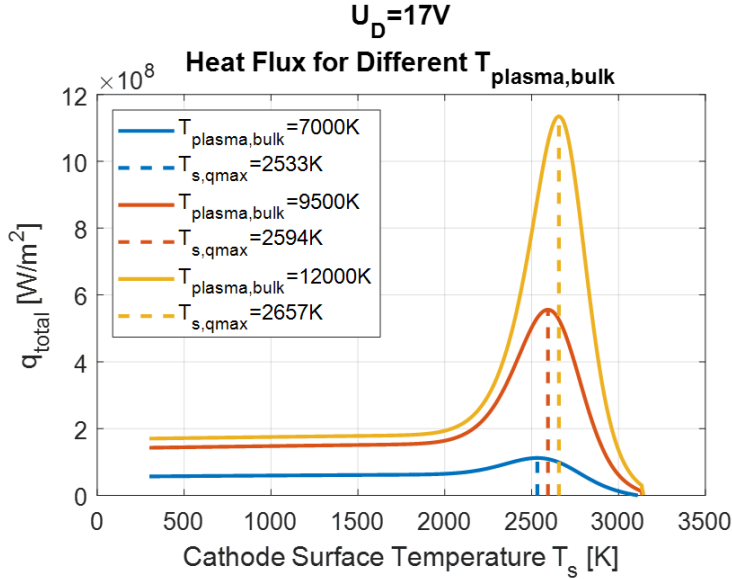


Figure 43: Heat flux dependency on $T_{\text{plasma,bulk}}$, with indication of the cathode surface temperature with maximum heat flux

Abbildung 43: Abhängigkeit der Wärmestromdichte von $T_{\text{plasma,bulk}}$, mit Angabe der Kathodenoberflächentemperatur bei maximaler Wärmestromdichte

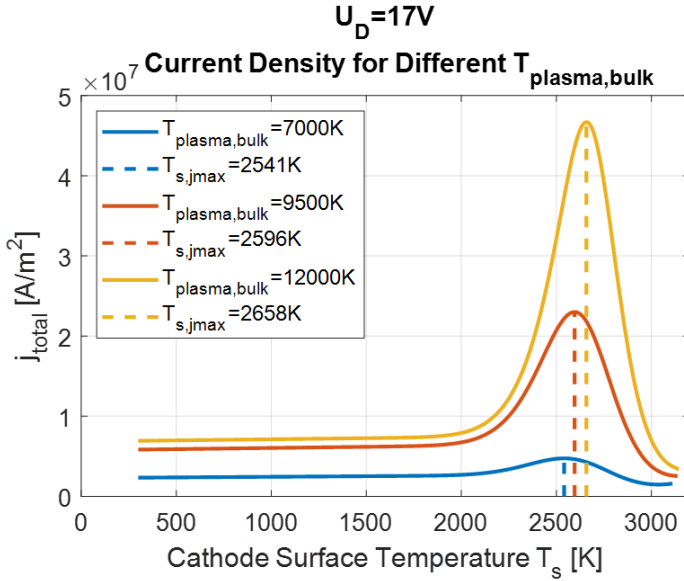


Figure 44: Current density dependency on $T_{\text{plasma,bulk}}$, with indication of the cathode surface temperature with maximum current density

Abbildung 44: Abhängigkeit der elektrischen Stromdichte von $T_{\text{plasma,bulk}}$, mit Angabe der Kathodenoberflächentemperatur bei maximaler Stromdichte

4.1.2.3 Dependence of the heat flux and current density on U_D

The dependence on the U_D is examined in Figure 45 and Figure 46. It can be seen from Figure 45, that while the maximum value of the heat flux q_{max} depends almost linearly on the cathode voltage drop U_D , the position of the maximum is not affected by U_D at all. This is due to the fact that the voltage drop only enters the relation to the heat flux linearly in the heat flux due to ions q_{ion} , see Eq. (6) and the heat flux due to thermionically emitted electrons q_{em} , see Eq. (7). It can be seen from Figure 46, that the dependency of the current density on the cathode voltage drop is barely recognizable. This is because of the relatively low contribution of the current density due to field-enhanced thermionic emission with the dependency of $E_f \sim \sqrt[4]{U_D}$ in Eq.(19), and also because the current density due to ion flux j_{ion} in Eq. (6) is not dependent on the voltage drop, which is a simplification as the velocity of the ions is assumed to be the ion speed of sound, see Eq. (12). Originally the Bohm criterion, from which this

relation was derived, states an ion velocity greater or equal than the speed of sound, so here the lower bound was taken. However, in a further developed model, the ion velocity could depend on the voltage drop U_D , as well.

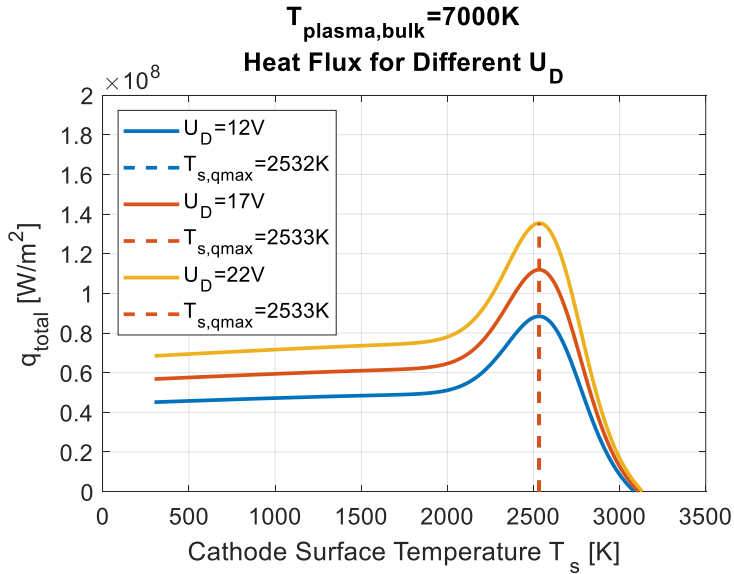


Figure 45: Heat flux dependency on U_D , with fixed temperature of the plasma bulk $T_{\text{plasma,bulk}} = 7000[\text{K}]$

Abbildung 45: Abhängigkeit der Wärmestromdichte von U_D , bei fester Temperatur des Plasmahintergrunds $T_{\text{plasma,bulk}} = 7000[\text{K}]$

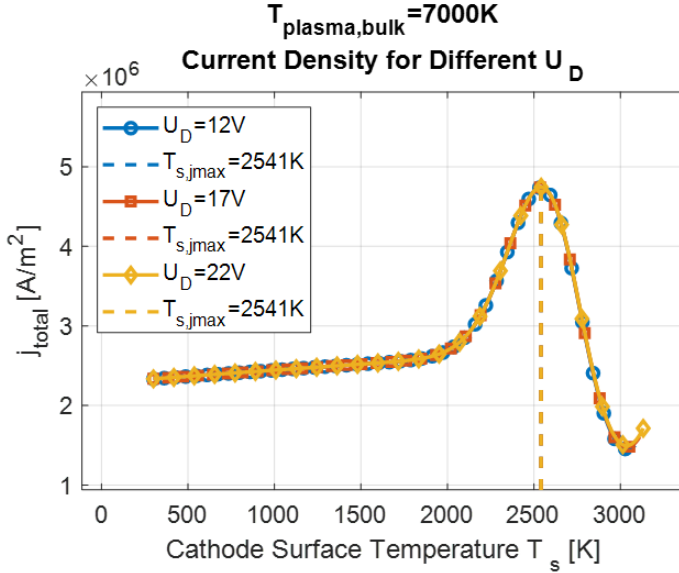


Figure 46: Current density dependency on U_D , with fixed temperature of the plasma bulk $T_{\text{plasma,bulk}} = 7000[\text{K}]$

Abbildung 46: Abhängigkeit der elektrischen Stromdichte von U_D , bei fester Temperatur des Plasmahintergrunds $T_{\text{plasma,bulk}} = 7000[\text{K}]$

4.2 Discussion

The newly proposed model for Evaporation-Determined Arc-Cathode Coupling (EDACC) for diffuse attachment in GMAW, was presented in detail. It is now time to discuss the reasonability of the model, in the context of the previous work.

The model proposed in this thesis does not consider a statement of the energy balance and is therefore not self-consistent. The cooling effect of the metal vapor on the local plasma is modelled by the simplified approach of temperature mixing as a weighted arithmetic mean between the plasma bulk temperature and the metal vapor temperature, see Eq. (14). It is reasonable to assume, that a more detailed treatment is possible, when considering a more microscopic scale. But it should be kept in mind that as the cathode layer is interacting with the arc, it is very likely that the system of the cathode layer is energetically open and therefore the whole system of arc and electrodes would need to be considered to close the energy balance.

It was not possible to determine the thickness of the metal vapor “cushion”, so it was not possible to determine if the influence of the vapor would reach over the length of electron energy relaxation, which can be calculated, as was done in [BEN95], to $\lambda_u \approx 100[\mu m]$. This length λ_u determines the length scale on which the assumption of LTE does not hold and $T_e \neq T_i$ and where the ionization degree can be expressed in terms of the electron temperature T_e following Van den Sanden’s 2-Temperature plasma approach [VAN89]. If the plasma temperature was influenced by the metal vapor on distances $\lambda_{vap} > \lambda_u$, the reasoning presented in this thesis will still hold as the metal vapors would also be able to affect the electron temperature T_e , to justify the assumption of the relation $T_{plasma,local} \approx T_e$. However, in order to do this, the arc column and the flows of the shielding gas need to be taken into account as well, and the cross-sections would need to be considered (for copper these are available in [ABD80]). In general it can be stated, that the argument, presented in 3.2 is still valid and there has to be a mechanism to decrease the ion flux, be it either by lowering the ionization degree by a lowered plasma temperature (Eq. (14)) or by some other means, as for example the non-monotonic potential as proposed in [ALM13] and shown in Figure 14. However, this potential should also depend on the particle flux of evaporated atoms and the plasma temperature in the near-cathode plasma, similar to Eq. (14), so that Eq. (14) might present a simple approximation to these even deeper physical processes. Also, the mechanism needs to scale exponentially, as the density of the metal evaporation from the cathode is growing at exponential rate, too.

The lowering of the heat flux alone, due to field-enhanced thermionic emission or evaporation heat losses will not be sufficient, as this would not cause a distinct maximum of the current density at $T_s < T_{boiling}$. If a model would be considered which does not provide this feature, it would lead to the following situation for an extended spot, as is present in “diffuse” attachment: the maximum heat flux would be generated at a lower temperature than the maximum current density, and in fact at the temperature of the maximum current density the net heat flux would be zero. This means, that the spot is heated until it reaches maximum temperature and in this situation, the heat flux is mainly generated on the circumference of the spot, where the temperature reaches $T_s(q_{max})$, while the current would be mainly generated over the area of the spot where the temperature is maximum $T_{s,max}(q > 0)$. This could cause the effect that with increasing radius of the spot, the total power scales with the radius $P \sim r_{HS}$, while the total current scales with the square $I \sim r_{HS}^2$. This means, that for larger

radii of the attachment, the power would not scale anymore linearly with the current $P \sim \sqrt{I}$ which is contrary to experience.

It should be added, that the influence of the Knight model for evaporation in Eq. (9), (13) and (15), originally came from the consideration that considerable heat fluxes could be present at $T_s > T_{boiling}$. It turned out that most of the heat flux is generated much below $T_{boiling}$ so that the implementation of the Knight model is not an integral part of the model presented and will therefore be presented in the Appendix A.

Finally, it should be mentioned that the accuracy of the exact value of n_0 , which in the best case should even be spatially resolved, can have an impact on the calculated distributions at lower surface temperatures, where $n_0 > n_{vap}$ so that the iron atom density is only determined by these plasma iron atoms $n_{Fe} \approx n_0$. For the conditions considered in this thesis (i.e. $n_0 = 2.5 \cdot 10^{22} [m^{-3}]$ according to [KOZ13]), this means surface temperatures below $T_s < 2303 [K]$, see Figure 35. Of course, depending on the exact value of n_0 this temperature threshold might vary as well. At surface temperatures below this threshold, the attachment will not be determined by the evaporation of the cathode anymore, but probably by the iron vapor present in the plasma bulk, either from the ignition process or from the evaporating anode.

5 Results: Coupling of the EDACC model to the weld pool

5.1 Set up for numerical CFD experiments

The numerical CFD experiments to study the interaction of the EDACC model with the weld pool were modelled in Ansys CFX, using the model from [MOK17, MOK20c]. For the calculation of the weld pool geometry an approach without the consideration of a free surface was chosen for reasons of calculation speed and the requirement of a defined surface for the application of the EDACC model. The solution was found for the steady state. The main system of equations that are being solved in the weld pool simulation are the Navier-Stokes equations, assuming laminar non-compressible flow with buoyancy Eq.(20), the mass conservation Eq. (21) and energy conservation Eq.(22) equations, as well as the Maxwell equations Eq.(23).

$$\rho \left(\frac{\partial \vec{u}}{\partial t} + (\vec{u} \cdot \nabla) \vec{u} \right) = -\nabla p + \nabla(\nu \nabla \vec{u}) + \rho \vec{g} \beta_A T + \vec{j} \times \vec{B} + \overrightarrow{S_{droplet,u}} \quad (20)$$

$$\nabla(\rho\vec{u}) = 0 \quad (21)$$

$$\frac{\partial h}{\partial t} + \nabla(\vec{u}h) = \nabla(\lambda\nabla T) + \frac{\vec{j}^2}{\sigma} + S_{droplet,h} \quad (22)$$

$$\vec{B} = \nabla \times \vec{A}; \nabla^2 \vec{A} = \mu_0 \vec{j} \quad (23)$$

Where ρ is the density, \vec{u} is the flow velocity vector, t is time, p is pressure, ν is the viscosity, \vec{g} is gravitation, β_A is thermal expansion coefficient, T is temperature, \vec{j} is current density vector, \vec{B} is the magnetic field vector, $\vec{S}_{droplet,u}$ is a momentum source due to droplets, h is the enthalpy, λ is the thermal conductivity, σ is the electrical conductivity, $S_{droplet,h}$ is an enthalpy source from the droplets, \vec{A} is the magnetic vector potential and μ_0 is the magnetic vacuum permeability, following the notation in [MOK17]. It is important to note that the purpose of the work presented in this chapter is not to demonstrate an accurate prediction of the weld pool geometry, but rather to analyze the influence of the EDACC approach on the arc-attachment and the weld pool flows under different circumstances, in order to gain a deeper understanding of the occurring interdependencies.

5.1.1 The domain

The mesh and the computational domain is depicted in Figure 47. Here, the center of the arc, the point (x_0, y_0) , is marked with a spherical marker, with $x_0 = 10[mm]$ and $y_0 = 0[mm]$. The frontal surface is modelled as an inlet, the backward surface as an outlet, the surface at $y = 0[mm]$ is modelled as a symmetry plane and the other surfaces are modelled as no slip walls, moving with the welding velocity v_{weld} . The whole domain has the thickness of $d = 6[mm]$ and it is considered to be filled with steel, moving from the inlet to the outlet with constant velocity v_{weld} .

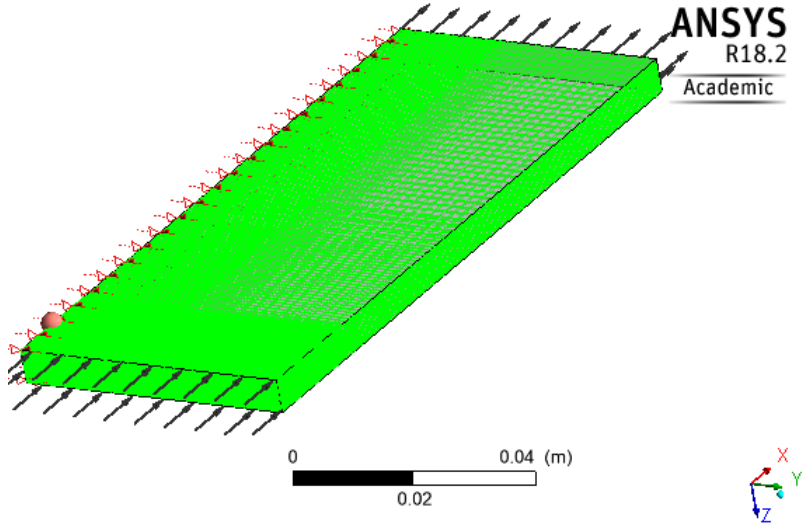


Figure 47: Computational domain for the weld pool calculation including mesh

Abbildung 47: Rechendomäne für die Schmelzbadberechnung einschließlich Berechnungsnetz

The heat transfer considers the thermal energy and the flows are considered laminar. Consideration of electromagnetics is switched on, using the electric potential for the electric field and the magnetic vector potential for the magnetic field. No external magnetic field is assumed. The flows are considered as buoyant, with gravity in z -direction and buoyancy reference density of $\rho_{iron} = 7854 \left[\frac{kg}{m^3} \right]$.

5.1.2 The material

The material is steel, modelled as a fluid. The viscosity of the steel is considered as

$$\begin{aligned} \nu &= 20 [Pa \cdot s] \text{ for } T < T_{melting} \\ \nu &= 10^{(-0.622 + \frac{2478[K]}{T})} \cdot 10^{-3} [Pa \cdot s] \text{ for } T > T_{melting} \end{aligned} \quad (24)$$

thereby approximating the solid steel as a highly viscous fluid. The density is set to

$$\rho_{Fe} = 7854 \left[\frac{kg}{m^3} \right] \text{ with molar mass } M_{Fe} = 55.85 \left[\frac{kg}{kmol} \right].$$

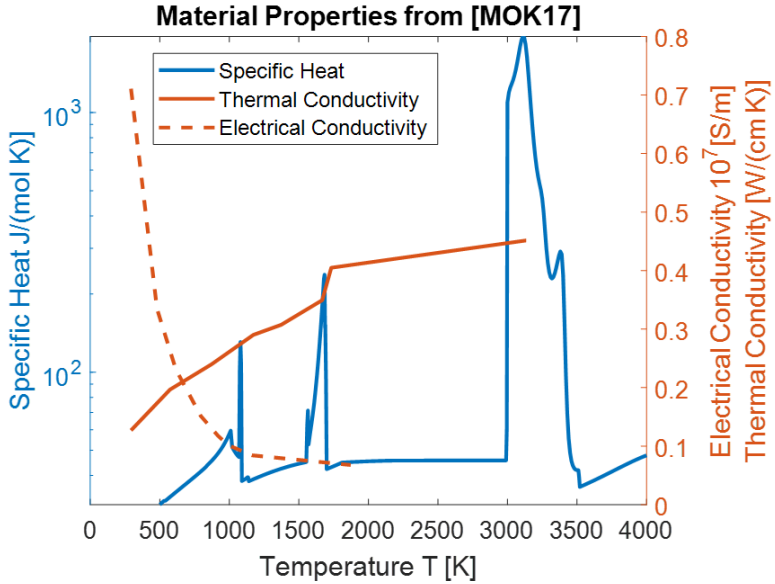


Figure 48: Specific Heat, thermal conductivity and electrical conductivity, as used, from [MOK17] (temperature ranges were extrapolated)

Abbildung 48: Die verwendete spezifische Wärme, Wärmeleitfähigkeit und elektrische Leitfähigkeit, aus [MOK17] (Temperaturbereiche wurden extrapoliert)

The specific heat capacity is evaluated at constant pressure, following the given temperature dependency shown in Figure 48. Please note, that this specific heat is an approximation, used for numerical reasons, as in reality the specific heat of iron is discontinuous at the temperatures of phase transition, e.g. melting, vaporization. The thermal conductivity and the electrical conductivity are given in Figure 48, as well. The magnetic permeability is taken as $\mu = \mu_0 = 1.25665 \cdot 10^{-6} \left[\frac{\text{kg} \cdot \text{m}}{\text{s}^2 \cdot \text{A}^2} \right]$ and the electric permittivity was not set. Please note, that the magnetic permeability is in reality temperature dependent.

A reference state was set at a specified point, with the reference temperature $T_{ref} = 1733[\text{K}]$ and the reference pressure $p_{ref} = 1[\text{atm}]$.

For all temperature dependent values, extrapolated tables are generated within Ansys CFX for the range of $T_{min} = 100\text{K}$ to $T_{max} = 4000\text{K}$.

5.1.3 The boundaries

5.1.3.1 Inlet

Over the entire Inlet a mass flux is imposed of solid steel, with the velocity of v_{weld} and temperature $T_0 = 300[K]$. The boundary condition for the electric field is zero flux and the magnetic field is acting parallel to the surface.

5.1.3.2 Outlet

Over the entire Outlet an outgoing mass flux is imposed, with the velocity of v_{weld} . The boundary condition for the electric field is zero flux and the magnetic field is acting parallel to the surface.

5.1.3.3 Top

The Top surface is modelled as a no slip wall, moving with the welding velocity v_{weld} in x-Direction. A heat transfer coefficient (HTC) is defined, in reference to the outside temperature of $T_0 = 300[K]$

$$HTC = \frac{1}{2} \cdot 5.67 \cdot 10^{-8} [W m^{-2} K^{-4}] \cdot (T + T_0) \cdot (T^2 + T_0^2) + 20 [W m^{-2} K^{-1}] \quad (25)$$

For the electric field, an incoming current flux is defined as specified in 5.1.3.7. The magnetic field is set to be normal to the surface. The sources defined on this surface include the heat and mass by the droplets (specified in 5.1.3.6), the electric current due to the arc-cathode coupling as well as heat flux due to the arc-cathode coupling (specified in 5.1.3.7) and evaporation losses (specified in 5.1.3.8). No external magnetic vector potential is defined.

5.1.3.4 Bottom

The Bottom surface is modelled as a no slip wall, moving with the welding velocity v_{weld} in x-Direction. The heat transfer coefficient (HTC) is defined by Eq.(25), in reference to the outside temperature of $T_0 = 300[K]$. For the electric field, the potential is set to ground potential and the magnetic field is set to be normal to the surface.

5.1.3.5 Wall

The outer Wall surface is modelled as a no slip wall, moving with the welding velocity v_{weld} in x-Direction. The heat transfer coefficient (HTC) is defined by Eq.(25), in

reference to the outside temperature of $T_0 = 300[K]$. For the electric field, the boundary condition is set to zero flux and the magnetic field is set to be parallel to the surface.

5.1.3.6 Droplets

The influence of the droplets is modelled as a steady fluid mass flux, of a mass rate \dot{m}

$$\dot{m} = \rho_{wire} \cdot \left(\frac{d_{wire}}{2}\right)^2 \cdot v_{wire} \quad (26)$$

evenly distributed over an area on the Top surface

$$(x - x_0)^2 + (y - y_0)^2 < r_{droplet}^2 \quad (27)$$

With $\rho_{wire} = 7854 \left[\frac{kg}{m^3}\right]$ the wire density, $d_{wire} = 1[mm]$ the diameter of the wire, $v_{wire} = 8\left[\frac{m}{min}\right]$ the wire feed velocity and $r_{droplet} = 0.5[mm]$ a droplet radius. The speed of the mass flux is assumed to the speed of the wire v_{wire} and the temperature of the droplets as $T_{droplet} = 2300[K]$.

5.1.3.7 Arc heat and current

To model the arc heat, the heat fluxes due to ions and emitted electrons leading to the corresponding heat flux, e.g. Figure 43, and the current density, e.g. Figure 44, are combined and written as a table in dependence of the cathode surface temperature. The tables can be imported into Ansys CFX as a function of temperature.

The heat source and current density are set as sources at the Top surface, limited to a fixed area with radius of the heat source $r_{HS} = 5[mm]$.

This approach is equivalent to setting a constant plasma temperature at $T_{plasma,bulk} = 7000[K]$ and a constant background of iron atoms $n_0 = 2.5 \cdot 10^{22}[m^{-3}]$ for the area covered by the radius r_{HS} and applying the model described by Eq. (6), (7) and (11)-(19).

5.1.3.8 Evaporation

The heat flux due to evaporation is modelled according to the model of [KNI79], see Appendix A, and also written as a table in dependence of temperature and imported in Ansys CFX. The evaporation heat flux is set to act all over the Top surface. Figure 49 shows an example of the heat flux, for a ambient temperature of $T_{amb} = 7000[K]$ and a ambient pressure of $p_{amb} = 1[atm]$ for iron, with $T_{boiling} = 3134[K]$.

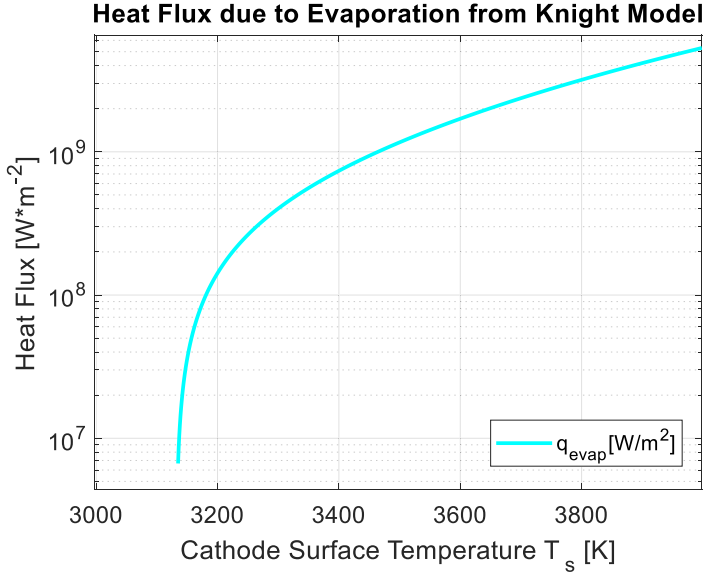


Figure 49: Heat flux due to evaporation, according to Knight model [KNI79]

Abbildung 49: Wärmestromdichte durch Verdampfung, nach dem Knight-Modell [KNI79]

5.2 Sensitivity analysis

In order to give an impression for the interrelations imposed by the presented model for Evaporation-Determined Arc-Cathode Coupling (EDACC) on the welding parameters with the weld pool formation, CFD simulations with varied parameters were performed. The welding parameters that were varied were the radius of the heat source r_{HS} and the welding velocity v_{weld} . Additionally the radius of the droplets r_{droplet} , the droplet temperature T_{droplet} and the wire feed speed v_{wire} , which is equivalent here to the droplet velocity were varied as well. An overview over the varied parameters is found in Table 1.

The analysis is concerned with the surface temperature field in 0, the heat flux and current density distribution as generated by the EDACC model in 5.2.2, the current density vector field on the weld pool melting iso-surface as well as the electromagnetic

force in the weld pool in 5.2.3 and finally also the velocities in the weld pool in 5.2.4. The welding direction is in all cases from left to right.

Table 1: Reference index for the overview of results

Case name	Basic case a) parameters	Case name	Parameter modification compared to basic case:
a)	$r_{HS} = 5[mm]$	b)	Reduced heat source radius $r_{HS} = 3[mm]$
a)	$v_{weld} = 30[\frac{cm}{min}]$	c)	Increase of welding speed $v_{weld} = 60[\frac{cm}{min}]$
a)	$r_{droplet} = 0.5[mm]$	d)	Reduced droplet radius $r_{droplet} = 0.2[mm]$
a)	$T_{droplet} = 2300[K]$	e)	Increase of droplet temperature $T_{droplet} = 3124[K]$
a)	$v_{wire} = 8[\frac{m}{min}]$	f)	Reduced wire feed speed $v_{wire} = 4[\frac{m}{min}]$ (droplet speed)

5.2.1 Analysis of the surface temperature field

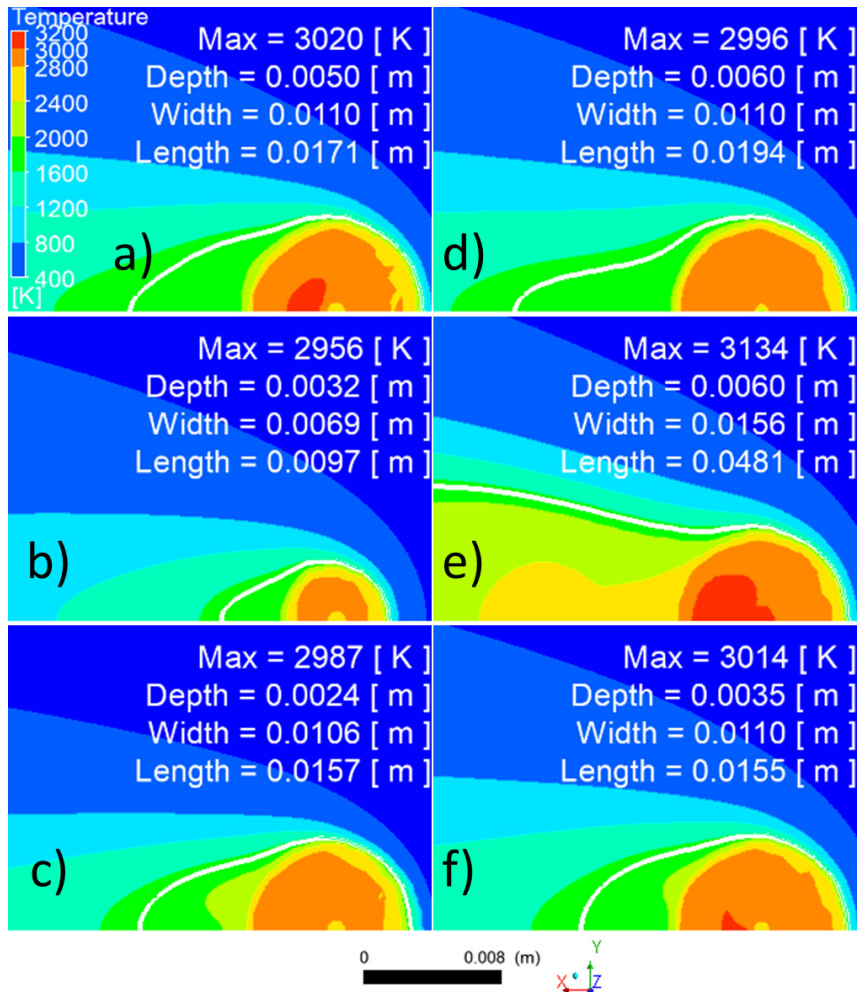


Figure 50: Surface temperature field with weld pool depth, width and length indicated, as well as maximum temperature. The black contour line gives the melting isothermal. a) was published in [MOK20b]

Abbildung 50: Oberflächentemperaturfeld mit angegebener Schmelzbadtiefe, -breite und -länge sowie maximaler Temperatur. Die schwarze Konturlinie gibt die Schmelzisotherme an. a) wurde veröffentlicht in [MOK20b]

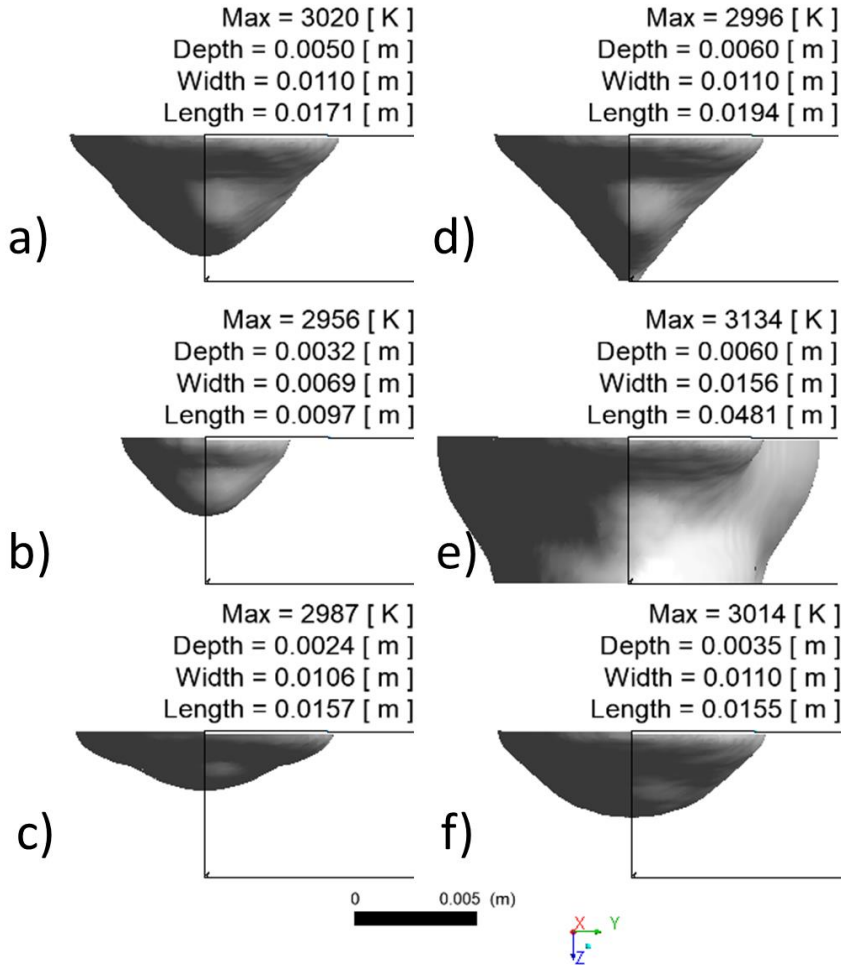


Figure 51: Cross Sections with weld pool depth, width and length indicated, as well as maximum temperature

Abbildung 51: Querschnitte mit Angabe der Schmelzbadtiefe, -breite und -länge sowie der maximalen Temperatur

Figure 50 a) shows the surface temperature field of the basic case, with the contour of the melt pool drawn in black. It can be seen that the maximum temperature remains below boiling temperature and there is a temperature minimum in the centre of the attachment, where the relatively cold droplets stream into the weld pool, with a

maximum of temperature slightly behind it. Also the geometrical parameters of the weld pool are displayed and the cross section can be seen in Figure 51 a). It should be noted that the length of the weld pool is shorter than expected for all parts of the analysis a)-f), which indicates that there might be an unphysical setting in the CFD weld pool calculation, possibly related to the boundary conditions for the magnetic field, as the magnetic permeability was not considered to be temperature dependent, or the lacking of a free surface. However, since in this thesis, the main focus lies on the model for the arc-cathode interaction, only the conditions for the attachment should be studied.

Figure 50 b) shows the surface temperature field and Figure 51 b) the cross section for the case, where the radius for the heat source was reduced to $r_{HS} = 3[mm]$. This leads to an even lower maximum surface temperature and also much smaller weld pool dimensions. Again, no boiling occurs.

Figure 50 c) shows the surface temperature distribution and Figure 51 c) the cross section for the case where the weld speed was increased to $v_{weld} = 60[cm/min]$. It can be seen here, that the maximum temperature decreased in comparison with the equivalent Figure 50 a) and also the depth decreased to about half and the length became a bit shorter.

Figure 50 d) shows the temperature distribution and Figure 51 d) the cross section for the case where the droplet radius was decreased to $r_{droplet} = 0.2[mm]$. It can be seen that the maximum temperature is slightly lower than in Figure 50 a), but the depth and the length of the weld pool are larger, compared to Figure 50 a) and Figure 51 a). The depth of the weld pool actually reaches the limit of the plate thickness $d = 6[mm]$, which means that full penetration was achieved. This is due to the fact, that the same mass flow rate was kept and therefore the droplets were affecting the weld pool with a higher pressure, cutting deep into the weld pool bottom, as seen in Figure 51 a).

Figure 50 e) shows the temperature distribution and Figure 51 e) the cross section for the case where the droplet temperature was increased to $T_{droplet} = 3134[K]$, i.e. to boiling temperature. It can be seen that, again, the whole plate has been burned through and the length of the weld pool was considerably larger, due to the additional heat brought in by the very hot droplets (see 5.2.2). It can be also seen that the maximum temperature of the weld pool is now slightly above boiling temperature, leading to minor losses by evaporation. Also, there is no distinguished area of colder

surface temperature in Figure 50 e), which was present in Figure 50 a). This means the situation can also serve as an example for the surface temperature and the resulting attachment (i.e. heat flux and current density distributions), in the conditions, where the droplets have not considerable influence on the surface temperature field, i.e. in between droplet impingements.

Figure 50 f) shows the temperature distribution and Figure 51 f) the cross section for the case where the wire feed speed was decreased to $v_{wire} = 4[m/min]$, i.e. to half the rate from the basic case. Since the droplet velocity was assumed to equal the wire feed speed, this means not only the droplet mass flow rate but also the droplet speed was changed. It can be seen here, that the depth as well as the length of the melt pool is significantly smaller than in the equivalent from the basic case in Figure 50 a) and Figure 51 a).

5.2.2 Analysis of the heat flux and current density distributions

The analysis of the heat flux and current density distribution reveals the main characteristic feature of the attachment by the EDACC model. While current approaches for GMAW process simulation usually consider a Gaussian distribution for heat flux and current density, the EDACC model predicts distributions which are not axi-symmetric, as is exemplified in Figure 52.

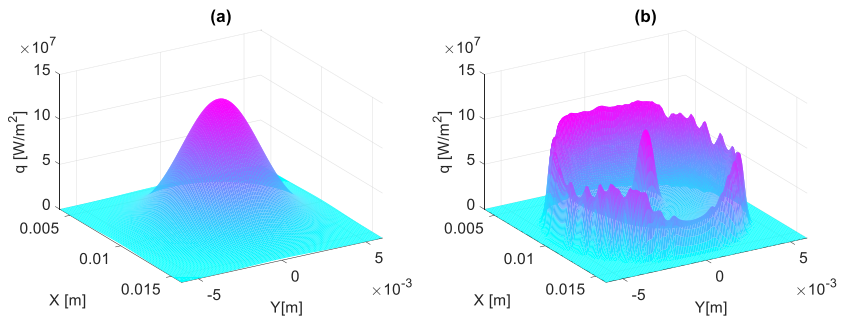


Figure 52: Comparison between Gaussian (a) and EDACC (b) heat flux distribution for basic case

Abbildung 52: Vergleich zwischen Gauß'scher Wärmestromdichteverteilung (a) und der Verteilung aus dem EDACC Modell (b) für den Basisfall

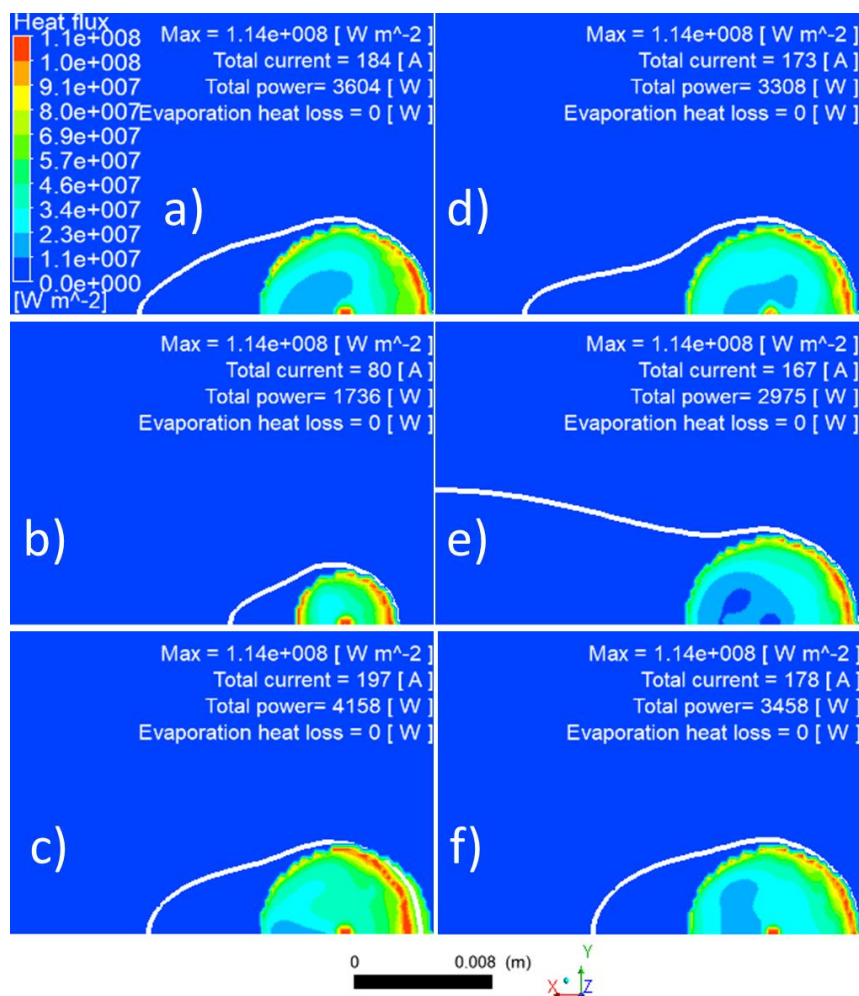


Figure 53: Heat flux distribution due to the EDACC model, with total current, total net heating power as well as total heat losses by evaporation indicated, as well as the maximum heat flux indicated. a) was published in [MOK20b]

Abbildung 53: Wärmestromdichteverteilung aufgrund des EDACC Modells, mit Angabe des Gesamtstroms, der gesamten Nettoheizleistung sowie der gesamten Wärmeverluste durch Verdampfung, mit Hervorhebung der maximalen Wärmestromdichte. a) wurde veröffentlicht in [MOK20b]

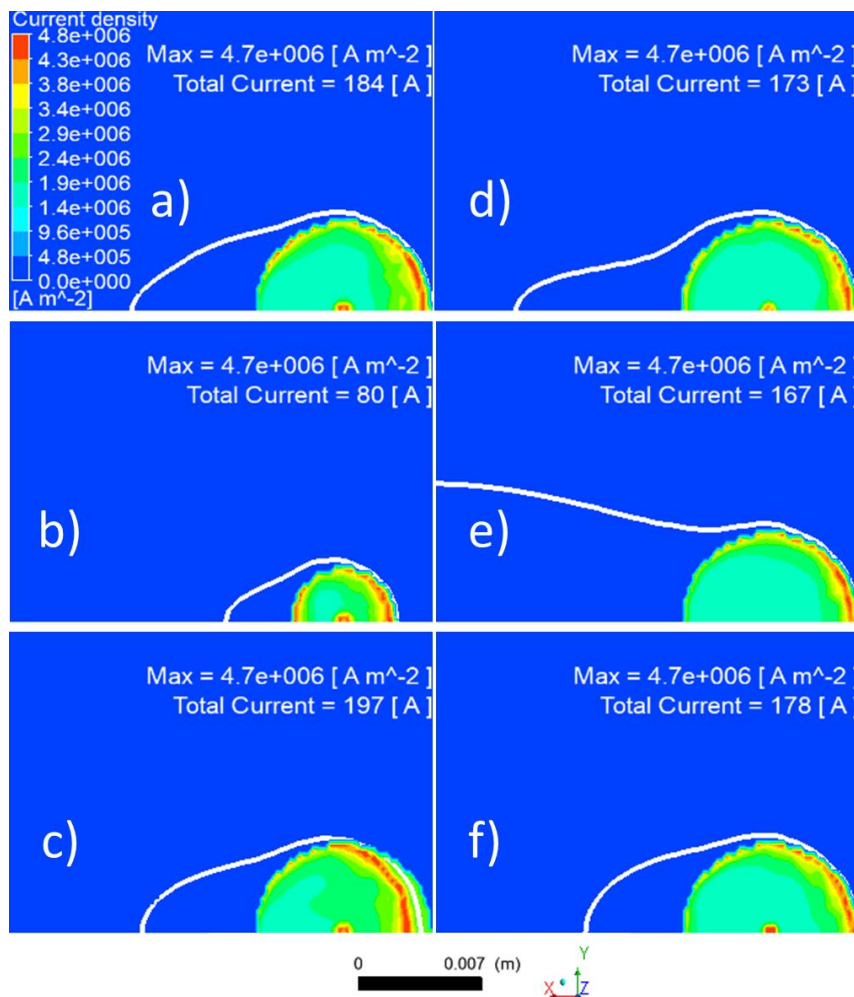


Figure 54: Current density distribution due to the EDACC model, with total current indicated. a) was published in [MOK20b]

Abbildung 54: Die Stromdichteverteilung aufgrund des EDACC Modells, mit Angabe des Gesamtstroms. a) wurde veröffentlicht in [MOK20b]

In Figure 53 the resulting heat flux from the EDACC model for all six considered cases is shown. It can be noted that the main contributions to the heat flux are accumulated along the melting front and also in the area, where the droplet stream impinges and

lowers the surface temperature. Also, it should be noted that as the surface remains below boiling temperature, there are no losses due to evaporation. While the maximum around the melting front is to be expected for the real attachment, the local maximum in the center at the position of the droplet impact requires a deeper discussion. As the model is applied for a steady state (see 5.1), the influx of the droplets is modeled as continuous. In reality the droplet impingement is a highly transient process which is also expected to impact the attachment, be it due to change of the surface temperature or due to increased vaporization or even due to the convex free surface and the resulting inhomogeneity in the electric field. It is therefore not to be concluded that such local maximum will occur in every state of attachment, but rather that this local maximum is to be considered only as a possible tendency of the true process. In Figure 54 the resulting current density distribution is shown. It shows that the current density distribution closely follows the heat flux distribution and the same reasoning applied here as well.

In Figure 53 b) the heat flux distribution is shown for the case of reduced $r_{HS} = 3[mm]$ and it can be seen, that the total current as well as the total power are much lower compared to the equivalent of the basic case shown in Figure 53 a), while the maximum heat flux remains the same. In general, the trends from Figure 53 a) are reproduced except for a higher contribution of heat flux at the back of the designated heat source area. This is due to the fact, that the weld pool is very short and therefore the gradients towards the solidification front are steep and more comparable to the gradients towards the melting front than in the case of Figure 53 a). The current density distribution shown in Figure 54 b) again displays the same behavior as the heat flux distribution in Figure 53 b).

In Figure 53 c) the case with increased welding velocity $v_{weld} = 60[cm/min]$ is shown. It can be seen that the total current as well as the total net heat power decreased, so the decrease in weld pool size is due to the higher throughput of cold material, which will be heated by the arc. It can be also seen that the heat flux extends beyond the melting front, which is due to ion flux from the bulk plasma. None the less, the maximum of the heat flux is still over the melt pool, slightly behind the melting front and also at the location of the droplets. The current density follows the same trend, see Figure 54 c).

From Figure 53 d) the case with reduced droplet radius $r_{droplet} = 0.2[mm]$ can be seen. It becomes apparent that the total net heating power as well as the total current actually decreased in comparison with Figure 53 a), but the general trends remain the same. This might be due to the smaller area of colder surface, where in Figure 50 d) the droplets impinge and the temperature of this area is close to the temperature of maximum heat flux $T_s \approx T_s(q_{max})$ from the EDACC model, see Figure 38. The same holds true for the current density, see Figure 54 d).

It can be seen from Figure 53 e) that the total current and the total net heating power are reduced compared to their equivalent in Figure 53 a), in the case of increased droplet temperature $T_{droplet} = 3134[K]$. This means that the increase in weld pool size, as seen in Figure 50 e) is attributable mainly to the additional heat carried in by the droplets. It should be especially noted that in the case where the droplets have no considerable influence on the surface temperature, that the distribution of the heat flux is now solely around the melting front. The same is true for the current density distribution, which is shown in Figure 54 e).

Figure 53 f) shows the case where the wire feed speed $v_{wire} = 4[m/min]$ was reduced. It shows that both total current as well as total net heating power are slightly reduced in comparison with the basic case Figure 53 a), but that the general trend concerning the distribution is nearly the same. The same is true for the current density distribution in Figure 54 f), but the maximum current density is slightly higher.

5.2.3 Analysis of the current density vector fields on the melting isosurface and the electromagnetic force in the weld pool

In Figure 55 the current density vector field along boundary of the melt pool is shown. It can be deduced, that most of the current goes from the current source shown in Figure 55 a) towards the cold material in front of the weld pool, where the electrical conductivity is higher, than in the hot melt pool.

This general trend holds true for all cases shown in In Figure 55 b)-f) and the current density field only differs slightly. It can be seen the current density is the strongest in Figure 55 f), the case with the decreased wire feed speed $v_{wire} = 4[m/min]$ and in Figure 55 c), the case where the welding speed was increased $v_{weld} = 60[cm/min]$, the strongest contribution to the current density seems to go slightly to the side.

In Figure 56 the vector field of the electromagnetic force in the melt pool is shown. It can be seen that the strongest component of the electro-magnetic force is located in the front of the weld pool and it is directed perpendicular to the main direction of the current density vector fields shown in Figure 55.

In Figure 56 b), which is the case with reduced radius of the heat source $r_{HS} = 3[mm]$, it should be noted that due to the lower total current the maximum electromagnetic force is only half of that from Figure 56 a). This is due to the decrease total current, as was seen in Figure 54 b).

For Figure 56 c), the case with increase welding velocity $v_{weld} = 60[cm/min]$, Figure 56 d) which is the case of reduced droplet radius $r_{droplet} = 0.2[mm]$, Figure 56 e), which is the case with the increased droplet temperature $T_{droplet} = 3134[K]$ and Figure 56 f) which is the case with the decreased wire feed speed $v_{wire} = 4[m/min]$, there is also no principal difference to their equivalent from Figure 56 a).

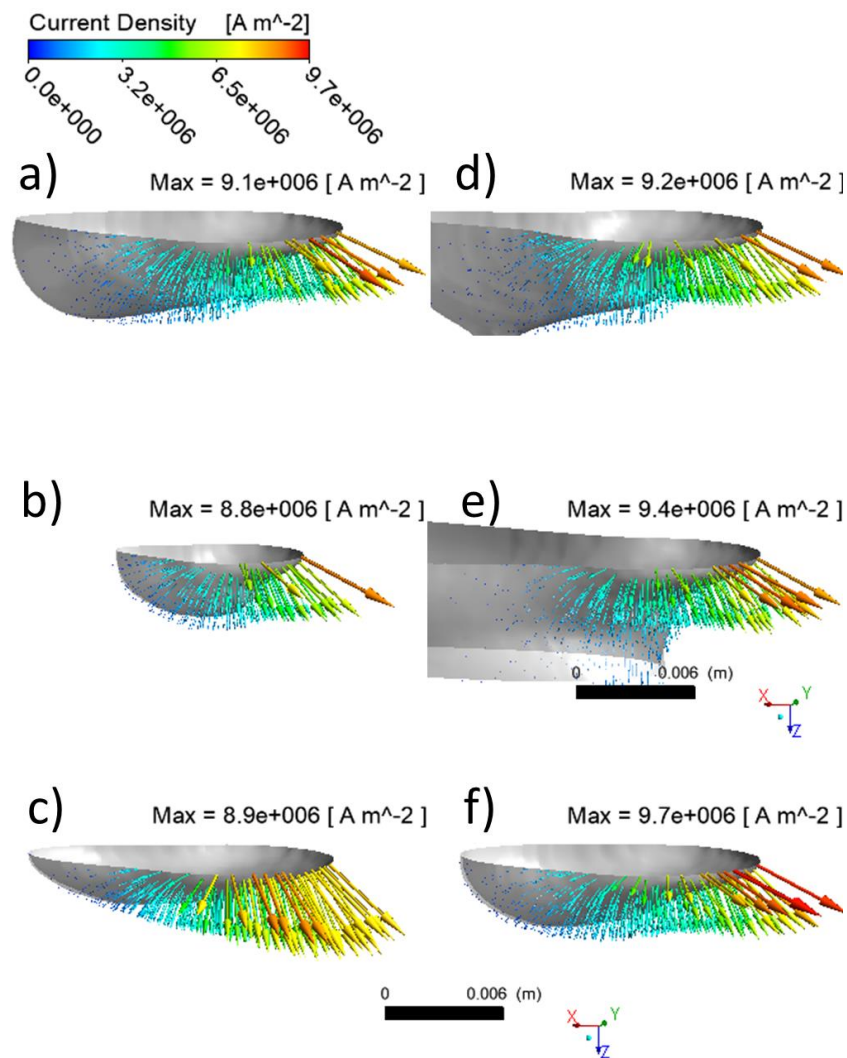


Figure 55: Current density vector field on the melting iso-surface, with the maximum current density indicated. Welding direction from left to right.

Abbildung 55: Stromdichte-Vektorfeld auf der Isofläche der Schmelztemperatur, wobei die maximale Stromdichte angegeben ist. Schweissrichtung von links nach rechts.

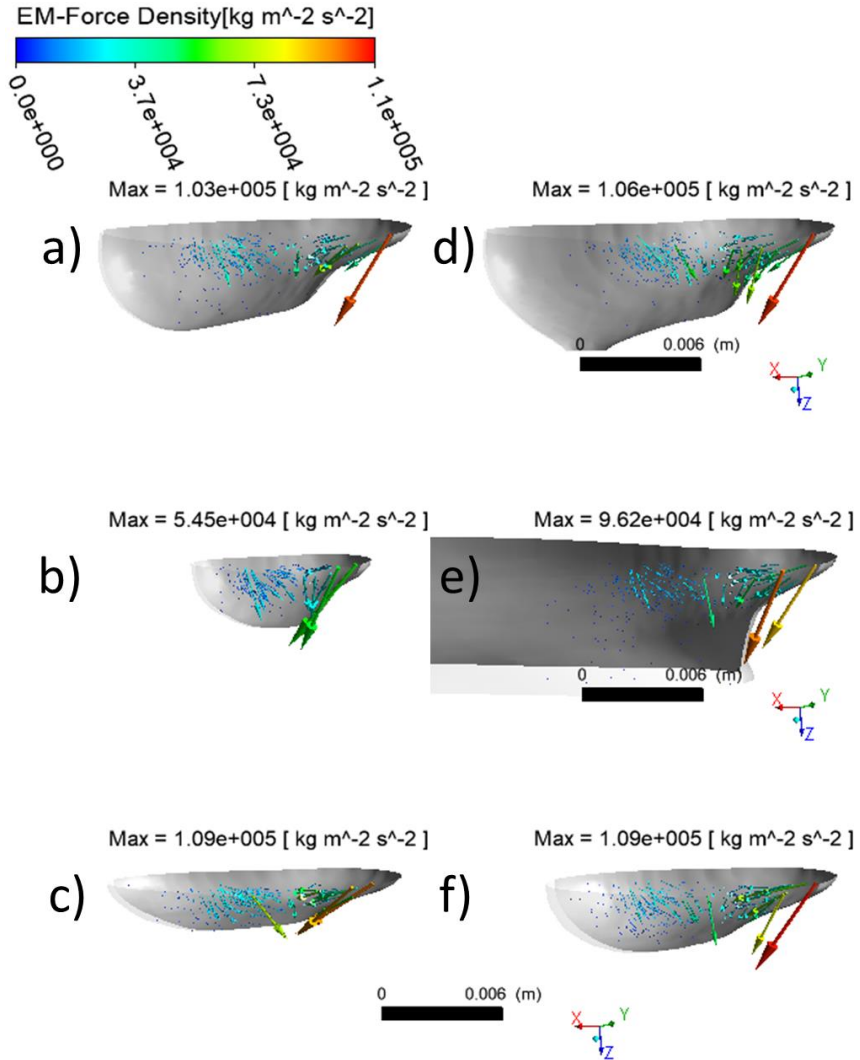


Figure 56: Electromagnetic force density in the melt pool, with the maximum value indicated. Welding direction from left to right.

Abbildung 56: Elektromagnetische Kraftdichte im Schmelzbad, mit Angabe des Maximalwerts. Schweissrichtung von links nach rechts.

5.2.4 Analysis of the velocity vector fields in the weld pool

In Figure 57 and Figure 58 the velocity vector field and stream lines within the melt pool are shown. From Figure 57 it can be seen that the highest velocities are found beneath the droplet source. However, it would be expected that the electromagnetic force has a stronger impact on the velocity vector field, therefore it is suggested that there might be a faulty setting in the magnetic boundary conditions, as was mentioned before in the discussion of Figure 50. Figure 58 shows that the flow field establishes a vortex in the backwards part of the melt pool.

For Figure 57 b) and Figure 58 b), the case of the decreased radius of the heat source $r_{HS} = 3[mm]$, it should be noted that the maximum velocity is slightly larger than in their equivalent Figure 57 a) and Figure 58 a).

For Figure 57 c) and Figure 58 c), the case of the increased welding velocity $v_{weld} = 60[cm/min]$ it should be noted that the maximum velocity is slightly larger than in their equivalent Figure 57 a) and Figure 58 a).

Figure 57 d), the case where the droplet radius was reduced $r_{droplet} = 0.2[mm]$, shows a surprising result with the maximum velocity vector pointed upward. It should also be noted, that the maximum flow velocity in this case is considerably higher than in the base case, in Figure 57 a). For the stream lines in Figure 58 d) the same general trends as in their equivalent in Figure 58 a) can be observed.

For the case with the increased droplet temperature $T_{droplet} = 3134[K]$, the velocity on the melt pool in Figure 57 e) has not much difference to their equivalent from the basic case in Figure 57 a). However, the stream lines in Figure 58 e) are much more disordered than the stream lines in Figure 58 a).

However, for the case with the decreased wire feed rate $v_{wire} = 4[m/min]$, the velocity vector field in the weld pool in Figure 57 f) and the stream lines of the velocity in the weld pool in Figure 58 f) show remarkable deviations from their equivalent from the base case Figure 57 a) and Figure 58 a), as in Figure 57 f) the largest velocity component is directed from the frontal melting temperature iso-surface upwards towards the center of the heat source. In Figure 58 a) it seems like the vortex has changed the direction of rotation.

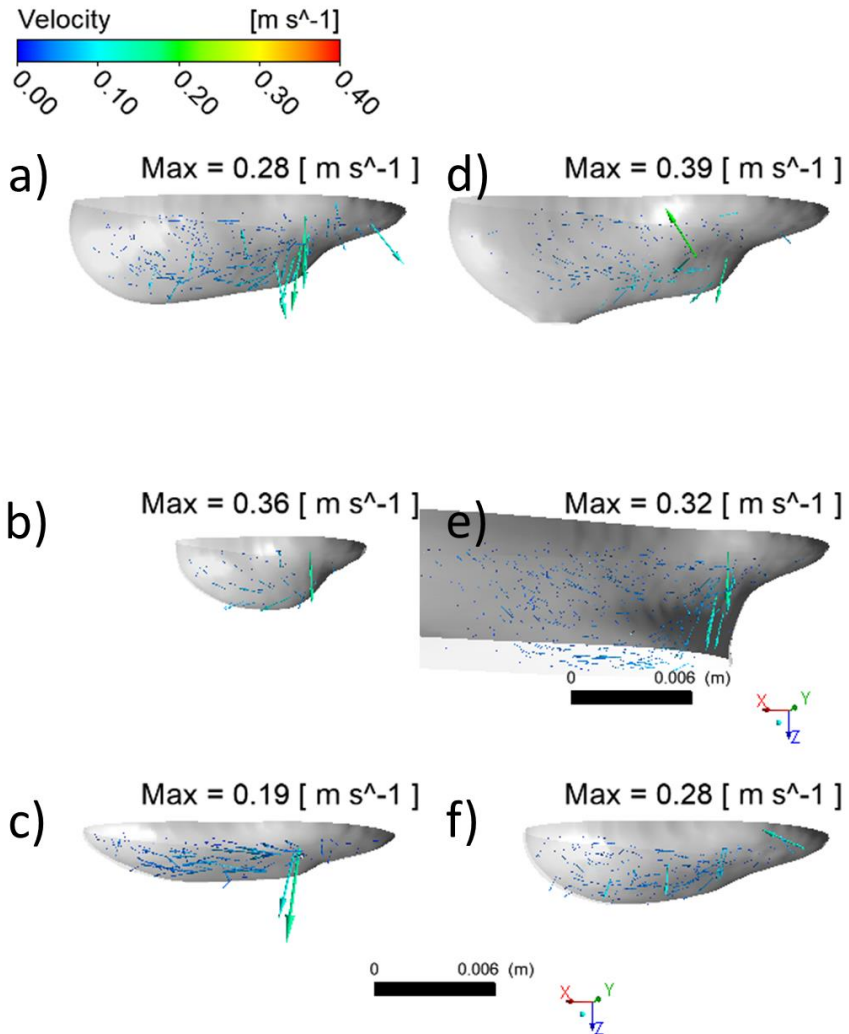


Figure 57: Flow velocity in the melt pool, with the maximum value indicated. Welding direction from left to right.

Abbildung 57: Strömungsgeschwindigkeit im Schmelzbad, wobei der maximale Wert angegeben ist. Schweissrichtung von links nach rechts.

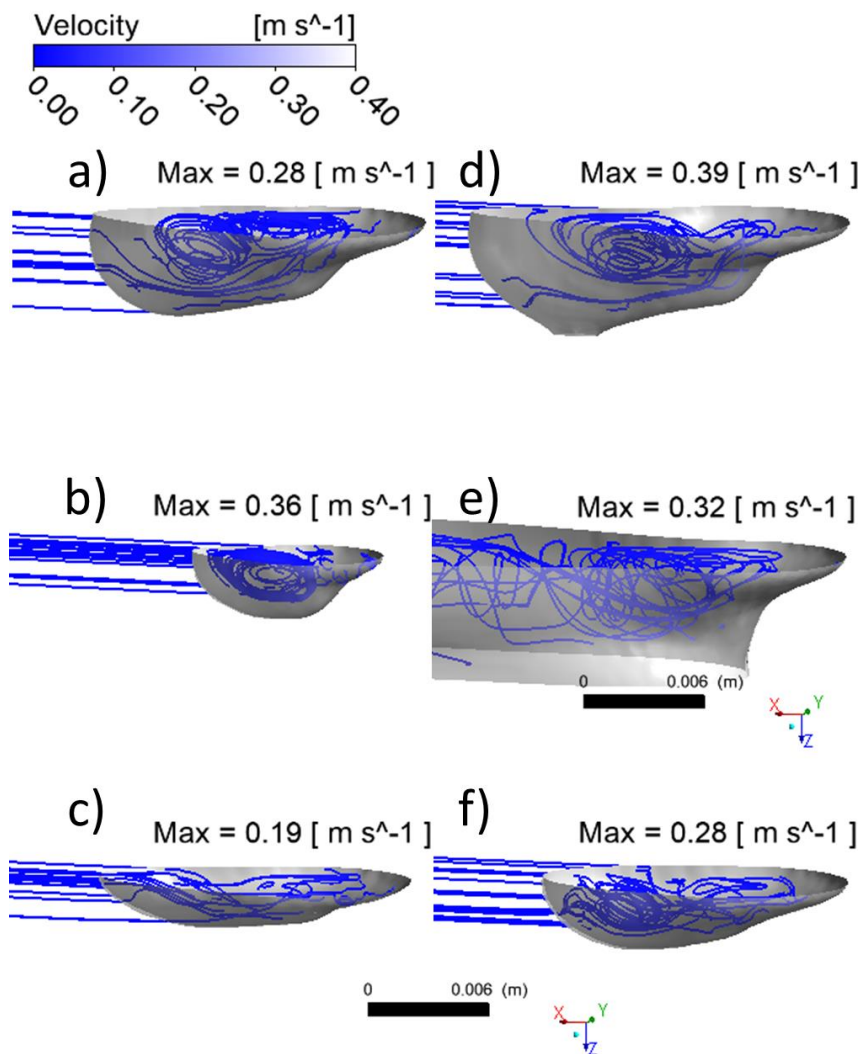


Figure 58: Flow velocity streamlines in the weld pool, with the maximum velocity indicated

Abbildung 58: Strömungslinien der Strömungsgeschwindigkeit im Schweißbad, mit Angabe der Maximalgeschwindigkeit

5.3 Discussion

The sensitivity analysis shows plausibility in accordance with the preliminary experiments as no boiling occurs. The lack of overheating is an advantage over current models. The disadvantage is, that since now power and current are coupled, they are not anymore free parameters, to be set, which renders the model a bit inflexible. Moreover, the total power and the total current depend mainly on the radius of the heat source, which is now a pre-defined parameter. In reality, it is reasonable to assume, that the radius of the heat source would depend on the entire arc column, as it is known from experiments that the weld pool width increases with increasing work piece to wire distance (WTWD).

From the models discussed in 2.2, the total voltage drop over the near-cathode layer is usually assumed as a pre-defined input variable, e.g. [BEN95]. However, it is very likely that there should be a condition, which relates the radius of the arc attachment to the electric field at the cathode layer. Specifically, that there should be a lower bound for the electric field that is necessary to achieve an attachment, in order to give a physical mechanism to constrict the arc radius. Maybe also a cooling of the plasma on the arc fringes, below the level where the ionization degree can cause a sufficient ion flux, could be suggested as a reasoning for the constriction of the arc attachment. However, it would still be needed to be checked, if the power balance over the complete arc-system would hold in these cases.

Also, the flows in the melt pool were sometimes erratic and the electromagnetic force seemed to have little influence. It cannot be excluded that a faulty setting, like a insufficient boundary condition in the CFD simulation, especially for the magnetic vector potential, which runs as a beta-feature, or the lacking consideration of a temperature dependent magnetic permeability are the cause of it. It was attempted to implement a temperature dependent magnetic permeability; however, the resulting simulation was unstable, and no run could be completed. In addition, no free surface was considered, therefore resulting in unusual weld pool shapes. However, the main goal was to investigate the coupling of the arc to the weld pool and for this reason, an approximate effect of the weld pool to the weld pool surface is sufficient as a first step. It needs to be kept in mind, that the deformation of the free surface of the weld pool can be considerable, therefore increasing the distance locally to the electrode tip by a large margin and possibly influencing the electric field and therefore also arc-cathode

attachment as well. Another reason for the detection of only minor influence of the electromagnetic force density could be in the mesh density of the top surface, as with a finer mesh density, also the area of the highest current density would be smaller, therefore requiring a higher current density to achieve the same total current, which could be accomplished by setting a higher plasma temperature $T_{plasma,bulk}$. As the electromagnetic forces scale with the 2nd power of the current density, they could become more dominating.

Finally, it should be noted, that both the welding speed as well as the lack or presence of a thermal influence of the droplets on the weld pool surface have strong influence on the coupling. In the case of higher welding speed, the cathode area is colder and therefore does not couple to the arc as well (compare Figure 53 a), c) and Figure 54 a), c)). With the combination with a model for the arc column, this could explain extinction processes for higher welding speeds v_{weld} . Also, there should be considerable difference in the coupling observable for spray transfer (with a continuously cooling effect on the surface by the droplets) and globular transfer, where for most of the time the arc and the weld pool surface remain unperturbed by the droplets (compare Figure 53 a), e) and Figure 54 a), e)). From the analysis in 5.2 it can be derived that the droplet radius or the droplet speed has only a minor influence on the attachment (compare Figure 53 a), d), f) and Figure 54 a), d) f), however it seems like the influence of the droplets dominates over the electromagnetic influence in the formation of the weld pool.

6 Conclusions and Outlook

The goal of this thesis is to nurture the mutual understanding between the field of theoretical plasma physics and the field of welding research. Therefore, a model for the Evaporation-Determined Arc-Cathode Coupling in GMAW (EDACC) was presented as well as the dialectic argument supporting the model. Theoretical considerations and logical arguments are critical tools to understand the mechanisms and interrelations, as the nature of the cathode layer is intricate, especially for non-refractory materials. Such considerations and arguments are also critical because of the small spatial dimensions of the cathode layer, which are prohibitive for direct measurements of the processes.

So far, the existing models all suffered from the shortcoming of predicting temperatures above boiling temperature for the cathode surface, but the preliminary experiments in this thesis did not show any boiling of the weld pool. Also, the assumption of spot attachment could not be confirmed in the experiments for the conditions of Ar+8%CO₂ shielding gas as discussed in 3.1.2.

These results lead to the development of a model for the arc-cathode coupling that successfully resolves these observations.

The newly developed EDACC model suggests the arc-cathode coupling is the result of an interaction of the metal vapor from the cathode with the bulk plasma of the arc and that the current transfer is mainly determined by the ion flux. The metal vapor provides the atoms for ionization and therefore the substrate of the process. At the same time, it limits the flux of ions by lowering the ionization degree through cooling of the near-cathode plasma. This last suggestion is the core of this thesis, but it must be stressed that this suggestion is based upon the assumption that the electron temperature is affected by the neutral metal vapor as well, which may be considered controversial.

However, even if the electron temperature is not directly affected by the metal vapor, the need for a mechanism that lowers the ion flux still holds, because the density of the neutral metal vapor atoms is exponentially increasing, as deduced in the presented dialectic argument in 3.2. This is evident from the fact that the weld pool remains below boiling temperature.

The developed model allows for qualitative statements about the distributions of heat flux and current density to the weld pool. Therefore, a sensitivity analysis was performed in coupling the model to a simple CFD weld pool simulation.

The distributions of the current density and the heat flux show a characteristic profile which clearly deviates from the axisymmetric Gaussian distribution, which is typically assumed in the current GMAW process simulation approaches. A non-axisymmetric distribution of the current density at the cathode or the molten pool has an effect on the distribution of the Lorentz forces in the weld pool. Although in [MUR11] the influence of the electromagnetic forces due to the electric current density distribution appeared to be rather minor compared to the influence of the droplets on the formation of the weld pool, which was confirmed in [MOK20c] as well as in this thesis, a stronger influence under different conditions cannot be excluded. Increased influences are to

be expected for example at higher plasma temperatures (e.g. submerged arc welding or with other shielding gas) where higher current densities would occur, but also possible if the plasma column is taken into account, due to the changed entry vector of the electric field lines. Another reason could also be an insufficient mesh density at the top surface, which was unable to resolve the temperature gradients of the weld pool surface with sufficient accuracy, and therefore artificially increasing the area of the highest current density, thereby lowering the current density, when the current is assumed as given. Furthermore, it could be concluded, that the cathodic heating mechanism in GMAW is not independent of the process itself and also depends on welding parameters which do not directly affect the power supply by the power source. Parameters like welding velocity, plasma temperature and the presence of droplets affect the distribution of current density and heat flux to the cathode.

Therefore, the understanding about the interdependencies of the process creates an opportunity to define several more trajectories for gaining more control over the process. For example, the strong dependency of the weld pool surface temperature implicates a possibility of control over the process by an additional heat source, such as by a laser (laser assisted-GMAW). By heating specific areas of the weld pool and surrounding, the distribution of the current can be deviated from the distribution of heat and also the area of attachment can be shaped.

Another trajectory for gaining more control could be by defining the weld pool surface temperature, and thereby the attachment, through cooling or heating by the droplets. This could be realized by either adjusting the melting rate of the wire, for example by resistive pre-heating of the wire, or by selecting the shielding gas composition accordingly. Also, an additional hot wire could help to influence the shape of the attachment.

Finally, the strong dependence on the temperature of the plasma bulk could be used as well. This could be done by intentionally controlling the plasma temperature, where the model predicts a more constricted attachment for a higher plasma temperature (with occurrence of boiling, as is the case in the experiments with helium, shown in 3.1.1) and a more wide attachment for lower plasma temperatures. Possibly the addition of elements with a low first ionization energy, like lithium, sodium, aluminum and potassium, either by an electrode wire coating or by the application of a primer on the work piece, could have an effect on the temperature of the plasma bulk $T_{plasma,bulk}$

and therefore the maximum surface temperature of positive heat flux $T_{s,max}(q > 0)$ as well as the temperature of maximum heat flux $T_{s,max}(q_{max})$ could be shifted to lower temperatures, possibly causing less burn-off of allowing elements.

Many questions remain unanswered by the model, such as the influence of the arc column, which was not considered in this thesis. A further development of the model should include the interrelation of the arc column with the radius of the arc-cathode attachment, as the total current and total heat power predicted by this model are strongly dependent on the radius. Therefore, the radius should be related to the arc column and also the current and energy parameters which is set on the power source, as well as the control strategy. This would also take into account transient effects, such as those present in pulsed GMAW processes or short circuits which occur in the widely used regulated short arc processes.

The role of the deformed surface should be investigated as well, because with increasing distance to the wire electrode, the attachment should become weaker, possibly modifying the distributions presented in 5.2.2.

A further development should attempt a self-consistent coupling over the complete arc, including anode layer, plasma column and cathode layer. So far, such coupling proved to be difficult, even if there are a few successful examples, see [KHR18].

Finally, the experimental validation of the model could be more robust, but so far, no experimental method for the direct determination of the heat fluxes and current density distributions is known. A possible way of validation could be the comparison of weld pool geometries, if a more comprehensive CFD model is available.

Zusammenfassung und Ausblick

Die vorliegende Arbeit versteht sich als Beitrag zum gegenseitigen Verständnis zwischen dem Gebiet der theoretischen Niedertemperatur-Plasmaphysik und dem Gebiet der Schweißtechnik. Aus dieser Motivation heraus, wird hier ein Modell für die verdampfungsbestimmte Kopplung von Lichtbogen und Kathode beim MSG-Schweißen vorgestellt, das mit einer dialektischen Argumentation begründet wird. Da die Beschaffenheit der Kathodenschicht komplex ist, insbesondere bei nicht-hitzebeständigen Metallen und da die kleinen räumlichen Dimensionen der Kathodenschicht keine direkten Messungen der Prozesse erlauben, sind theoretische Überlegungen und logische Argumente das wichtigste Werkzeug, um die Mechanismen und Zusammenhänge zu verstehen.

Alle bisher bestehenden Modelle sagen Temperaturen der Kathodenoberfläche oberhalb der Siedetemperatur vorher, jedoch zeigten die Vorversuche kein Sieden des Schweißbades. Auch die Annahme der Anbindung durch kleine Kathodenflecken konnte in den Experimenten für die Bedingungen des Ar+8%CO₂-Schutzgases, wie in 3.1.2 diskutiert, nicht bestätigt werden.

Aus diesen Gründen wurde ein Modell für die Kopplung von Lichtbogen und Kathode entwickelt, das eine Übereinstimmung mit diesen beiden Beobachtungen ermöglicht.

Das neu entwickelte EDACC Modell suggeriert, dass die Kopplung von Lichtbogen und Kathode das Ergebnis einer Wechselwirkung des Metaldampfes von der Kathode mit dem Plasma des Lichtbogens ist und dass die Stromübertragung hauptsächlich durch den Ionenfluss bestimmt wird. Der Metaldampf stellt die Atome für die Ionisation und damit das Substrat des Prozesses zur Verfügung und begrenzt gleichzeitig den Ionenfluss, indem er den Ionisationsgrad durch Kühlung des kathodennahen Plasmas senkt. Diese Hypothese ist der Kern dieser Arbeit, jedoch sollte betont werden, dass diese Hypothese auf der Annahme basiert, dass die Elektronentemperatur auch durch den neutralen Metaldampf beeinflusst wird, was umstritten sein könnte.

Auch wenn die Elektronentemperatur nicht direkt vom Metaldampf beeinflusst wird, so besteht jedoch die Notwendigkeit eines Mechanismus, der den Ionenfluss ab einer bestimmten Oberflächentemperatur senkt, während die Atomdichte exponentiell zunimmt, wie in der vorliegenden dialektischen Argumentation in 3.2 abgeleitet wurde und wie sich aus der Tatsache ergibt, dass das Schweißbad unterhalb der Siedetemperatur bleibt.

Das entwickelte Modell erlaubt nun qualitative Aussagen über die Verteilung von Wärmestrom und elektrischer Stromdichte auf das Schweißbad und wurde daher in einer Sensitivitätsanalyse in der Kopplung mit einer vereinfachten CFD-Schweißbadsimulation untersucht.

Die Verteilungen der elektrischen Stromdichte und der Wärmestromdichte weisen ein charakteristisches Profil auf, welches deutlich von der axisymmetrischen Gaußverteilung abweicht, wie sie in der Regel in den bisherigen Ansätzen der Schweißprozesssimulation des MSG-Prozesses angenommen wird. Eine nicht-axisymmetrische Verteilung der Stromdichte an der Kathode bzw. dem Schmelzbad hat wiederum eine Rückwirkung auf die Verteilung der Lorentzkräfte im Schmelzbad. Obwohl in [MUR11] der Einfluss der elektromagnetischen Kräfte aufgrund der elektrischen Stromdichteverteilung im Vergleich zum Einfluss der Tropfen auf die Bildung des Schweißbades als eher untergeordnet erschien, was in [MOK20c], sowie in dieser Arbeit bestätigt wurde, kann ein stärkerer Einfluss unter anderen Bedingungen nicht ausgeschlossen werden. Verstärkte Einflüsse sind z.B. bei höheren Plasmatemperaturen (z.B. beim Unterpulverschweißen oder mit anderem Schutzgas) zu erwarten wo höhere Stromdichten auftreten, aber möglicherweise auch bei einer Mitberücksichtigung der Plasmasäule durch den veränderten Eintrittswinkel der elektrischen Feldlinien. Außerdem konnte festgestellt werden, dass der kathodische Wärmeumsatz beim MSG-Schweißen nicht unabhängig vom Prozess selbst ist und dass Schweißparameter, welche zunächst unabhängig sind von der Energiezufuhr durch die Schweißstromquelle, wie Schweißgeschwindigkeit, Plasmatemperatur oder die Anwesenheit von Tropfen, die Verteilung der elektrischen Stromdichte und der Wärmestromdichte an der Kathode beeinflussen. Insbesondere, in der Situation, wenn die Tropfen eine niedrigere Temperatur haben als die Schmelzbadoberfläche, würde sich demnach die Anbindung des Lichtbogens beim Eintritt des Tropfens in das Schmelzbad in diesem Bereich konzentrieren, was zu einer Einschnürung des Lichtbogens führen würde. Dies würde zusätzliche elektromagnetische Kräfte im Tropfeneintrittsgebiet verursachen.

Das Verständnis über die Zusammenhänge des Prozesses erlaubt es nun, mehrere weitere Trajektorien zu definieren, die zu einer tieferen Beherrschung des Prozesses führen. Beispielsweise verweist die starke Abhängigkeit der Lichtbogenanbindung von der Oberflächentemperatur des Schweißbades auf eine Steuerung des Prozesses durch eine zusätzliche Wärmequelle, z.B. durch einen Laser (lasergestützte GMAW).

Durch das Erwärmen bestimmter Bereiche des Schweißbades und der Umgebung kann die Stromverteilung unabhängig von der Wärmeverteilung in bestimmten Bereichen unterdrückt oder gefördert werden und so kann auch die Fläche der Anbindung beherrscht und geformt gestaltet werden.

Eine weitere Möglichkeit, mehr Kontrolle über den Prozess zu erlangen, könnte die Steuerung der Oberflächentemperatur des Schweißbades, und damit der Lichtbogenanbindung, durch Kühlung oder Erwärmung mittels der Tropfen sein. Dies könnte entweder aus einer Anpassung der Schmelzrate des Drahtes, z.B. durch resistive Vorwärmung des Drahtes, folgen, oder mit einer entsprechenden Schutzgaszusammensetzung erreicht werden. Auch das Hinzufügen eines zusätzlichen Heißdrahtes kann die Oberflächentemperatur des Schweißbades beeinflussen und somit die Lichtbogenanbindung beherrschbar machen.

Schließlich könnte der Prozess auch über die starke Abhängigkeit von der Plasmatemperatur beherrscht werden, indem die Plasmatemperatur gezielt gesteuert wird. Das Modell sagt demnach eine stärker konzentrierte Lichtbogenanbindung für eine höhere Plasmatemperatur vorher (vgl. mit den in 3.1.1 dargestellten Experimenten mit Helium, in denen Sieden auftritt) und eine verbreiterte Lichtbogenanbindung für niedrigere Plasmatemperaturen. Möglicherweise könnte die Zugabe von Elementen mit einer niedrigen ersten Ionisationsenergie wie Lithium, Natrium, Aluminium und Kalium, entweder über eine Elektroden Drahtbeschichtung oder durch das Aufbringen eines Primers auf das Werkstück, einen Einfluss auf die Temperatur des Plasmas $T_{plasma,bulk}$ und damit auf die maximale Oberflächentemperatur $T_{s,max}(q > 0)$ sowie auf die Temperatur des maximalen Wärmestroms $T_{s,max}(q_{max})$ haben.

Es gibt noch viele Fragen, die weiterer Forschung bedürfen, da z.B. der Einfluss der Lichtbogensäule nicht berücksichtigt wurde. Eine Weiterentwicklung des Modells sollte die Wechselbeziehung der Lichtbogensäule mit dem Radius des Lichtbogenansatzpunktes beinhalten, da der von diesem Modell vorhergesagte Gesamtstrom und die Gesamtwärmeleistung stark vom Radius abhängig sind. Daher sollte der Radius von der Lichtbogensäule und auch von den Strom- und Energieparametern an der Stromquelle als auch der Regelungsstrategie abhängen. Dies würde es dann auch ermöglichen, transiente Effekte zu berücksichtigen, wie sie

in gepulsten MSG-Prozessen oder bei Kurzschlüssen, wie z.B. in den weit verbreiteten geragelten Kurzlichtbogen-Prozessen, auftreten.

Auch der Einfluss der gekrümmten Schweißbadoberfläche sollte eingehender untersucht werden, denn mit zunehmendem Abstand zur Drahtelektrode sollte die Lichtbogenanbindung schwächer werden und möglicherweise die in 5.2.2 dargestellten Verteilungen von Wärmestromdichte und elektrischer Stromdichte verändern.

Eine weitere Entwicklung sollte eine selbstkonsistente Kopplung über den gesamten Lichtbogen, einschließlich Anodenschicht, Plasmasäule und Kathodenschicht, umfassen. Bisher gestaltet sich diese Kopplung schwierig, auch wenn es erfolgreiche Beispiele gibt, siehe [KHR18].

Schließlich könnte die experimentelle Validierung des Modells noch robust sein, allerdings ist eine experimentelle Methode zur direkten Bestimmung der Verteilung der Wärmestromdichte und der elektrischen Stromdichte bisher noch nicht bekannt. Eine mögliche Art der Validierung könnte der Vergleich von Schweißbadgeometrien sein, wenn ein umfassenderes CFD-Modell verfügbar ist.

7 References

- [ABD80] - ABDELHAKIM, H., J.P. DINGUIRARD und S. VACQUIE, 1980. The influence of copper vapour on the transport coefficients in a nitrogen arc plasma [online]. *Journal of Physics D: Applied Physics*, **13**(8), 1427-1438. Available from: doi:10.1088/0022-3727/13/8/012
- [ALM13] - ALMEIDA, N.A., M.S. BENILOV, L.G. BENILOVA, W. HARTMANN und N. WENZEL, 2013. Near-Cathode Plasma Layer on CuCr Contacts of Vacuum Arcs [online]. *IEEE Transactions on Plasma Science*, **41**(8), 1938-1949. Available from: doi:10.1109/TPS.2013.2260832
- [BEN07] - BENILOV, M.S., 2007. Stability of direct current transfer to thermionic cathodes: I. Analytical theory [online]. *Journal of Physics D: Applied Physics*, **40**(5), 1376-1393. Available from: doi:10.1088/0022-3727/40/5/011
- [BEN08] - BENILOV, M.S., 2008. Understanding and modelling plasma–electrode interaction in high-pressure arc discharges: a review [online]. *Journal of Physics D: Applied Physics*, **41**(14), 144001. Available from: doi:10.1088/0022-3727/41/14/144001
- [BEN10] - BENILOV, M.S. und L.G. BENILOVA, 2010. The double sheath on cathodes of discharges burning in cathode vapour [online]. *Journal of Physics D: Applied Physics*, **43**(34), 345204. Available from: doi:10.1088/0022-3727/43/34/345204
- [BEN14] - BENILOV, M.S., 2014. Multiple solutions in the theory of dc glow discharges and cathodic part of arc discharges. Application of these solutions to the modeling of cathode spots and patterns: a review [online]. *Journal of Physics D: Applied Physics*, **23**(5), 54019. Available from: doi:10.1088/0963-0252/23/5/054019
- [BEN15] - BENILOV, M.S. und L.G. BENILOVA, 2015. Physics of Spotless Mode of Current Transfer to Cathodes of Metal Vapor Arcs [online]. *IEEE Transactions on Plasma Science*, **43**(8), 2247-2252. Available from: doi:10.1109/TPS.2015.2445093
- [BEN93] - BENILOV, 1993. Nonlinear heat structures and arc-discharge electrode spots [online]. *Physical review. E, Statistical physics, plasmas, fluids, and related interdisciplinary topics*, **48**(1), 506-515. Available from: doi:10.1103/PhysRevE.48.506

- [BEN95] - BENILOV, M.S. und A. MAROTTA, 1995. A model of the cathode region of atmospheric pressure arcs [online]. *Journal of Physics D: Applied Physics*, **28**(9), 1869-1882. Available from: doi:10.1088/0022-3727/28/9/015
- [CAY08] - CAYLA, F., 2008 - *Modélisation de l'interaction entre un arc électrique et une cathode* [online]. Thesis (PhD). Université Toulouse III – Paul Sabatier. Toulouse [Zugriff am: 20. September 2019]. Available from: http://thesesups.ups-tlse.fr/211/1/Cayla_Francois.pdf
- [COU97] - COULOMBE, S., 1997 - *A model of the electric arc attachment on non-refractory (cold) cathodes. Thesis (PhD)* [online]. MCGILL UNIVERSITY. Montreal, Canada [Zugriff am: 20. September 2019]. Available from: <https://www.collectionscanada.gc.ca/obj/s4/f2/dsk2/ftp02/NQ44393.pdf>
- [CRE13] - CRESSAULT, Y., A.B. MURPHY, P. TEULET, A. GLEIZES und M. SCHNICK, 2013. Thermal plasma properties for Ar–Cu, Ar–Fe and Ar–Al mixtures used in welding plasmas processes: II. Transport coefficients at atmospheric pressure [online]. *Journal of Physics D: Applied Physics*, **46**(41), 415207. Available from: doi:10.1088/0022-3727/46/41/415207
- [CRE15] - CRESSAULT, Y., 2015. Basic knowledge on radiative and transport properties to begin in thermal plasmas modelling [online]. *AIP Advances*, **5**(5), 57112. Available from: doi:10.1063/1.4920939
- [DEL90] - DELALONDRE, C. und O. SIMONIN, 1990. Modelling of high intensity arcs including a non-equilibrium description of the cathode sheath [online]. *Le Journal de Physique Colloques*, **51**(C5), C5-199-C5-206. Available from: doi:10.1051/jphyscol:1990524
- [GLE10] - GLEIZES, A., Y. CRESSAULT und P. TEULET, 2010. Mixing rules for thermal plasma properties in mixtures of argon, air and metallic vapours [online]. *Journal of Physics D: Applied Physics*, **19**(5), 55013. Available from: doi:10.1088/0963-0252/19/5/055013
- [HAI10] - HAIDAR, J., 2010. The dynamic effects of metal vapour in gas metal arc welding [online]. *Journal of Physics D: Applied Physics*, **43**(16), 165204. Available from: doi:10.1088/0022-3727/43/16/165204
- [HER10] - HERTEL, M., M. SCHNICK, U. FÜSSEL, S. GORCHAKOV und D. UHRLANDT, 2010 - *Numerical Simulation of GMAW Process Including Effects of*

Metal Vapour and Sheath Mechanisms at the Electrodes [online]. Proceedings of the International Scientific Colloquium Modelling for Material Processing, MMP, September 16-17 2010. Riga, Latvia [Zugriff am: 20. September 2019]. Available from: <http://www.modlab.lv/publications/mmp2010/pdfs/091-096.pdf>

[HER16] - HERTEL, M., 2016 - *Numerische Simulation des MSG-Prozesses. Thesis (PhD)* [online]. TU Dresden. Dresden. Dresdner fügetechnische Berichte. 37/2016 [Zugriff am: 20. September 2019]. Available from: https://www.researchgate.net/profile/Martin_Hertel/publication/322525800_Numerische_Simulation_des_MSG-Prozesses/links/5a5dfb7faca272d4a3df5daa/Numerische-Simulation-des-MSG-Prozesses.pdf

[HSU83] - HSU, K.C. und E. PFENDER, 1983. Two-temperature modeling of the free-burning, high-intensity arc [online]. *IEEE Transactions on Plasma Science*, **54**(8), 4359-4366. Available from: doi:10.1063/1.332672

[JAV16] - JAVIDI SHIRVAN, A., 2016 - *Modelling of cathode-plasma interaction in short high-intensity electric arc. Application to gas tungsten arc welding*. Gothenburg, Sweden: Chalmers University of Technology. Doktorsavhandlingar vid Chalmers tekniska högskola. Ny serie nr. 4062. ISBN 978-91-7597-381-4.

[JEO18] - JEONG, H., K. PARK, S. BAEK, D.-Y. KIM, M.-J. KANG und J. CHO, 2018. Three-Dimensional Numerical Analysis of Weld Pool in GMAW with Fillet Joint [online]. *International Journal of Precision Engineering and Manufacturing*, **19**(8), 1171-1177. Available from: doi:10.1007/s12541-018-0138-4

[KAD95] - KADDANI, A., 1995 - *Modélisations 2D et 3D des Arcs Electriques dans l'Argon à la Pression Atmosphérique avec la prise en compte du Couplage Thermique et Electrique Arc-Electrodes et de l'Influence des Vapeurs Métalliques*. Thesis (PhD). Pierre & Marie Curie Université Paris 6. Paris, France.

[KHR18] - KHRABRY, A., I.D. KAGANOVICH, V. NEMCHINSKY und A. KHODAK, 2018. Investigation of the short argon arc with hot anode. I. Numerical simulations of non-equilibrium effects in the near-electrode regions [online]. *Physics of Plasmas*, **25**(1), 13521. Available from: doi:10.1063/1.5007082

[KNI79] - KNIGHT, C.J., 1979. Theoretical Modeling of Rapid Surface Vaporization with Back Pressure [online]. *AIAA Journal*, **17**(5), 519-523. Available from: doi:10.2514/3.61164

- [KOZ13] - KOZAKOV, R., G. GÖTT, H. SCHÖPP, D. UHRLANDT, M. SCHNICK, M. HÄßLER, U. FÜSSEL und S. ROSE, 2013. Spatial structure of the arc in a pulsed GMAW process [online]. *Journal of Physics D: Applied Physics*, **46**(22), 224001. Available from: doi:10.1088/0022-3727/46/22/224001
- [KRA] - KRAMIDA, A. und Y. RALCHENKO - *NIST Atomic Spectra Database, NIST Standard Reference Database 78*.
- [KRI10a] - KRIKENT, I.V., I.V. KRIVTSUN und V.F. DEMCHENKO, 2010. Model of the processes of heat, mass and charge transfer in the anode region and column of the welding arc with refractory cathode. *The Paton Welding Journal*, **2010**(6), 2-9. The Paton Welding Journal.
- [KRI10b] - KRIVTSUN, I., V. DEMCHENKO, A. LESNOI, I. KRIKENT, P. PORITSKY, O. MOKROV, U. REISGEN, A. ZABIROV und V. PAVLYK, 2010. Modelling of electromagnetic processes in system 'welding arc – evaporating anode' Part 1 – Model of anode region [online]. *Science and Technology of Welding and Joining*, **15**(6), 457-462. Available from: doi:10.1179/136217110X12665778348506
- [LAN29] - LANGMUIR, I., 1929. The Interaction of Electron and Positive Ion Space Charges in Cathode Sheaths [online]. *Physical Review*, **33**(6), 954-989. Available from: doi:10.1103/PhysRev.33.954
- [LE 19] - LE PHAN, H., S. TASHIRO, H. VAN BUI, T. SUGA, T. SATO und M. TANAKA, 2019. Investigating cathode spot behavior in argon alternating current tungsten inert gas welding of aluminum through experimental observation [online]. *Journal of Physics D: Applied Physics*, **52**(26), 26LT02. Available from: doi:10.1088/1361-6463/ab198a
- [LOW08] - LOWKE, J.J. und M. TANAKA, 2008. The physics of non-thermionic cathodes of electric arcs [online]. In: J.E. JONES, Hg. *Gas discharges and their applications. Proceedings of the Seventeenth International Conference, Cardiff University 7th-12th September 2008*. Cardiff: GD 2008 Local Organizing Committee. ISBN 978-0-9558052-0-2. Available from: <https://ieeexplore.ieee.org/abstract/document/5379308>
- [LOW10] - LOWKE, J.J., A.B. MURPHY und M. TANAKA, 2010. Metal Vapour in MIG Arcs Can Cause (1) Minima in Central Arc Temperatures and (2) Increased Arc

- Voltages [online]. *Welding in the World*, **54**(9-10), R292-R297. Available from: doi:10.1007/BF03266742
- [LOW97a] - LOWKE, J.J. und J.C. QUARTEL, 1997. Use of Transport Coefficients to Calculate Properties of Electrode Sheaths of Electric Arcs [online]. *Australian Journal of Physics*, **50**(3), 539. Available from: doi:10.1071/P96089
- [LOW97b] - LOWKE, J.J., R. MORROW und J. HAIDAR, 1997. A simplified unified theory of arcs and their electrodes [online]. *IEEE Transactions on Plasma Science*, **30**(14), 2033-2042. Available from: doi:10.1088/0022-3727/30/14/011
- [MAC29] - MACKEOWN, S.S., 1929. The Cathode Drop in an Electric Arc [online]. *Physical Review*, **34**(4), 611-614. Available from: doi:10.1103/PhysRev.34.611
- [MES05] - MESYATS, G.A., 2005. Ectons and their role in plasma processes [online]. *Plasma Physics and Controlled Fusion*, **47**(5A), A109-A151. Available from: doi:10.1088/0741-3335/47/5A/010
- [MOK17] - MOKROV, O., O. LYSNYI, M. SIMON, U. REISGEN, G. LASCHET und M. APEL, 2017. Numerical investigation of droplet impact on the welding pool in gas metal arc welding [online]. *Materialwissenschaft und Werkstofftechnik*, **48**(12), 1206-1212. Available from: doi:10.1002/mawe.201700147
- [MOK19] - MOKROV, O., M. SIMON, R. SHARMA und U. REISGEN, 2019. Arc-cathode attachment in GMA welding [online]. *Journal of Physics D: Applied Physics*, **52**(36), 364003. Available from: doi:10.1088/1361-6463/ab2bd9
- [MOK20a] - MOKROV, O., M. SIMON, A. SCHIEBAHN und U. REISGEN, 2020. Concept for the calculation of the distribution of heat input in the cathode area by GMA welding [online]. *Welding in the World*, **34**(3), R103. Available from: doi:10.1007/s40194-020-00929-9
- [MOK20b] - MOKROV, O., M. SIMON, P. LOZANO, D. ARNTZ-SCHROEDER, R. SHARMA und U. REISGEN, 2020. Simulation des Lichtbogenansatzes beim MSG-Schweißen. In: *DVS Congress 2020 (submitted)*.
- [MOK20c] - MOKROV, O., M. SIMON, R. SHARMA und U. REISGEN, 2020. Effects of evaporation-determined model of arc-cathode coupling on weld pool formation in GMAW process simulation [online]. *Welding in the World*, **64**(5), 847-856. Available from: doi:10.1007/s40194-020-00878-3

- [MUR10] - MURPHY, A.B., 2010. The effects of metal vapour in arc welding [online]. *Journal of Physics D: Applied Physics*, **43**(43), 434001. Available from: doi:10.1088/0022-3727/43/43/434001
- [MUR11] - MURPHY, A.B., 2011. A self-consistent three-dimensional model of the arc, electrode and weld pool in gas-metal arc welding [online]. *Journal of Physics D: Applied Physics*, **44**(19), 194009. Available from: doi:10.1088/0022-3727/44/19/194009
- [NOM17] - NOMURA, K., K. YOSHII, K. TODA, K. MIMURA, Y. HIRATA und S. ASAI, 2017. 3D measurement of temperature and metal vapor concentration in MIG arc plasma using a multidirectional spectroscopic method [online]. *Journal of Physics D: Applied Physics*, **50**(42), 425205. Available from: doi:10.1088/1361-6463/aa8793
- [NOT56] - NOTTINGHAM, W.B., 1956. Thermionic Emission. In: S. FLÜGGE, W.B. NOTTINGHAM, R.H. GOOD, E.W. MÜLLER, R. KOLLATH, G.L. WEISSLER, W.P. ALLIS, L.B. LOEB, A. von ENGEL und P.F. LITTLE, Hg. *Electron-Emission Gas Discharges I / Elektronen-Emission Gasentladungen I*. Berlin, Heidelberg: Springer Berlin Heidelberg, S. 1-175. ISBN 978-3-642-45846-0.
- [OGI18] - OGINO, Y., S. ASAI und Y. HIRATA, 2018. Numerical simulation of WAAM process by a GMAW weld pool model [online]. *Welding in the World*, **62**(2), 393-401. Available from: doi:10.1007/s40194-018-0556-z
- [PAT72] - PATON, B.E., 1972. Welding in Space. *Welding Engineer*, **57**(1), 25-29. *Welding Engineer*.
- [PEK17] - PEKKER, L., 2017. A Sheath Collision Model with Thermionic Electron Emission and the Schottky Correction Factor for Work Function of Wall Material [online]. *Plasma Chemistry and Plasma Processing*, **37**(3), 825-840. Available from: doi:10.1007/s11090-016-9765-7
- [PRE76] - PREWETT, P.D. und J.E. ALLEN, 1976. The Double Sheath Associated with a Hot Cathode [online]. *Proceedings of the Royal Society A: Mathematical, Physical and Engineering Sciences*, **348**(1655), 435-446. Available from: doi:10.1098/rspa.1976.0048
- [REI15] - REISGEN, U. und L. STEIN, 2015 - *Grundlagen der Fügetechnik - Schweißen, Löten und Kleben*. Düsseldorf: DVS Media GmbH. Fachbuchreihe Schweißtechnik. Band 161. ISBN 978-3-945023-49-5.

- [RET96] - RETHFELD, B., J. WENDELSTORF, T. KLEIN und G. SIMON, 1996. A self-consistent model for the cathode fall region of an electric arc [online]. *Journal of Physics D: Applied Physics*, **29**(1), 121-128. Available from: doi:10.1088/0022-3727/29/1/021
- [RIC03] - RICHARDSON, O.W., 1903. The Electrical Conductivity Imparted to a Vacuum by Hot Conductors [online]. *Philosophical Transactions of the Royal Society A: Mathematical, Physical and Engineering Sciences*, **201**(331-345), 497-549. Available from: doi:10.1098/rsta.1903.0023
- [ROU10] - ROUFFET, M.E., M. WENDT, G. GOETT, R. KOZAKOV, H. SCHOEPP, K.D. WELTMANN und D. UHRLANDT, 2010. Spectroscopic investigation of the high-current phase of a pulsed GMAW process [online]. *Journal of Physics D: Applied Physics*, **43**(43), 434003. Available from: doi:10.1088/0022-3727/43/43/434003
- [RYK57] - RYKALIN, N.N., 1957 - *Berechnung der Wärmevergänge beim Schweißen*. Übersetzung aus dem Russischen. Berlin: Verlag Technik.
- [SCH10a] - SCHNICK, M., U. FÜSSEL, M. HERTEL, A. SPILLE-KOHOFF und A.B. MURPHY, 2010. Metal vapour causes a central minimum in arc temperature in gas-metal arc welding through increased radiative emission [online]. *Journal of Physics D: Applied Physics*, **43**(2), 22001. Available from: doi:10.1088/0022-3727/43/2/022001
- [SCH10b] - SCHNICK, M., U. FUESSEL, M. HERTEL, M. HAESSLER, A. SPILLE-KOHOFF und A.B. MURPHY, 2010. Modelling of gas-metal arc welding taking into account metal vapour [online]. *Journal of Physics D: Applied Physics*, **43**(43), 434008. Available from: doi:10.1088/0022-3727/43/43/434008
- [SEM16] - SEMENOV, I.L., I.V. KRIVTSUN und U. REISGEN, 2016. Numerical study of the anode boundary layer in atmospheric pressure arc discharges [online]. *Journal of Physics D: Applied Physics*, **49**(10), 105204. Available from: doi:10.1088/0022-3727/49/10/105204
- [VAL10] - VALENSI, F., S. PELLERIN, A. BOUTAGHANE, K. DZIERZEGA, S. ZIELINSKA, N. PELLERIN und F. BRIAND, 2010. Plasma diagnostics in gas metal arc welding by optical emission spectroscopy [online]. *Journal of Physics D: Applied Physics*, **43**(43), 434002. Available from: doi:10.1088/0022-3727/43/43/434002

- [VAL11] - VALENSI, F., S. PELLERIN, A. BOUTAGHANE, K. DZIERZEGA, N. PELLERIN und F. BRIAND, 2011. LTE Experimental Validation in a Gas Metal Arc Welding Plasma Column [online]. *Contributions to Plasma Physics*, **51**(2-3), 293-296. Available from: doi:10.1002/ctpp.201000061
- [VAN89] - VAN DE SANDEN, M.C., SCHRAM, PEETERS, J.A. VAN DER MULLEN und KROESEN, 1989. Thermodynamic generalization of the Saha equation for a two-temperature plasma [online]. *Physical review. A, General physics*, **40**(9), 5273-5276. Available from: doi:10.1103/PhysRevA.40.5273
- [WEN00] - WENDELSTORF, J., 2000 - *Ab initio modelling of thermal plasma gas discharges (electric arcs)*. Thesis (PhD). Braunschweig: Technische Universität Carolo-Wilhelmina.
- [XU09] - XU, G., J. HU und H.L. TSAI, 2009. Three-dimensional modeling of arc plasma and metal transfer in gas metal arc welding [online]. *International Journal of Heat and Mass Transfer*, **52**(7-8), 1709-1724. Available from: doi:10.1016/j.ijheatmasstransfer.2008.09.018
- [ZHO94] - ZHOU, X. und J. HEBERLEIN, 1994. Analysis of the arc-cathode interaction of free-burning arcs [online]. *Plasma Sources Science and Technology*, **3**(4), 564-574. Available from: doi:10.1088/0963-0252/3/4/014
- [ZHU92] - ZHU, P., J.J. LOWKE und R. MORROW, 1992. A unified theory of free burning arcs, cathode sheaths and cathodes [online]. *International Journal of Heat and Mass Transfer*, **25**(8), 1221-1230. Available from: doi:10.1088/0022-3727/25/8/011
- [ZIE07] - ZIELIŃSKA, S., K. MUSIOŁ, K. DZIERŻĘGA, S. PELLERIN, F. VALENSI, C. de IZARRA und F. BRIAND, 2007. Investigations of GMAW plasma by optical emission spectroscopy [online]. *Journal of Physics D: Applied Physics*, **16**(4), 832-838. Available from: doi:10.1088/0963-0252/16/4/019

A Appendix: Model for evaporation by Knight (1979)

For modelling the evaporation in this thesis, the model which was published in [KNI79] was used. The model is concerned with rapid surface vaporization of a metallic surface with back pressure, as is present, for example in laser welding. In the paper, two modes of evaporation are distinguished, the mode of diffusive evaporation and the mode of convective evaporation, where the paper is concerned with the latter one. In the convective mode, the gas-phase distribution function for the velocities consists of a drifting Maxwellian distribution at the outer edge of the Knudsen layer and of a half Maxwellian distribution at the phase interface. This means, that between the liquid and the bulk of the gas, within a distance of several mean free path lengths, there are many more atoms moving away from the liquid than back to the liquid. If both these particle fluxes were the same, the conditions would be called “saturated” and the evaporation mode would be diffusive. Of course, it is only in the mode of convective evaporation that there is a net particle flux away from the liquid-gas interface and that means that only in this mode, heat can be transferred by the particles away from the surface, in a significant way. In order to model this situation, i.e. the convective evaporation against a background pressure gas, the flow is structured into 3 zones, as can be seen in Figure 59.

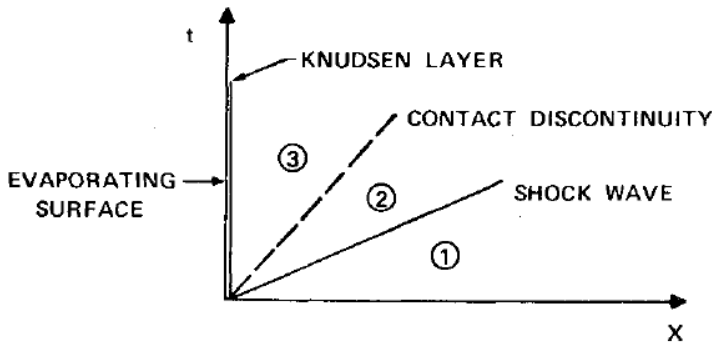


Figure 59: Subsonic flow structure, from [KNI79]

Abbildung 59: Strömungsstruktur unterhalb der Schallgeschwindigkeit, aus [KNI79]

The model then proceeds to calculate the net particle flux away from the surface, in dependence of the saturated vapor pressure of the surface and the temperature and pressure conditions far away from the surface in the static background, indicated with (1) in Figure 59.

The Rankine-Hugoniot relations give the velocity behind the shock wave as

$$u_2 = c_1 \cdot \left(\frac{p_2}{p_1} - 1 \right) / \left(\gamma \cdot \sqrt{1 + \frac{\gamma + 1}{2\gamma} \cdot \left(\frac{p_2}{p_1} - 1 \right)} \right) \quad (28)$$

With c_1 the speed of sound in (1), γ the ratio of specific heats (adiabatic constant), T_1 the temperature in zone (1), p_1 the pressure in zone (1) and p_2 the pressure in zone (2).

It is then stated that across the contact discontinuity $u_2 = u_k$ and $p_2 = p_k$, where u_k and p_k constitute the flow velocity and the pressure at the edge of the Knudsen layer.

Finally the jump conditions across the Knudsen layer are defined a

$$\frac{T_k}{T_s} = \left[\sqrt{1 + \pi \left(\frac{\gamma - 1}{\gamma + 1} \frac{m_k}{2} \right)^2} - \sqrt{\pi} \frac{\gamma - 1}{\gamma + 1} \frac{m_k}{2} \right]^2 \quad (29)$$

$$\begin{aligned} \frac{\rho_k}{\rho_s} = & \sqrt{\frac{T_k}{T_s}} \cdot \left[\left(m_k^2 + \frac{1}{2} \right) \cdot \exp(m_k^2) \cdot \operatorname{erfc}(m_k) - \frac{m_k}{\sqrt{\pi}} \right] + \\ & \frac{1}{2} \frac{T_s}{T_k} \cdot \left[1 - \sqrt{\pi} \cdot m_k \cdot \exp(m_k^2) \cdot \operatorname{erfc}(m_k) \right] \end{aligned} \quad (30)$$

With $m_k = \frac{u_k}{\sqrt{2 \cdot R_{\text{specific}} \cdot T_k}}$, a value which is related to the Mach-Number M_k on the

Knudsen edge via $M_k = m_k \cdot \sqrt{\frac{2}{\gamma}}$, T_k the temperature at the Knudsen edge, T_s the temperature at the evaporating surface and ρ_s the mass density according to the saturated vapor pressure p_s .

The saturated vapor pressure can be calculated by the Clausius-Clayperon equation

$$p_s = p_{\text{amb}} \cdot \exp \left(\frac{H_{\text{vap}}}{R} \cdot \left(\frac{1}{T_{\text{boiling}}} - \frac{1}{T_s} \right) \right) \quad (31)$$

Here, p_s denotes the saturated vapor pressure, $p_{\text{amb}} (= p_1)$ denotes the ambient pressure, H_{vap} denotes the latent heat of evaporation, R denotes the universal gas constant. In this mode, the saturated mass density on the surface can be calculated by

$$\rho_s = \frac{p_s}{R_{\text{specific}} \cdot T_s} \quad (32)$$

With R_{specific} the specific gas constant and the mass density ρ_k and the particle density n_k at the edge of the Knudsen layer can be calculated as

$$\rho_k = \frac{p_k}{R_{\text{specific}} \cdot T_k}; \quad n_k = \frac{\rho_k}{m_{\text{atom}}} \quad (33)$$

The speed of sound in zone one, in the case of a plasma can be calculated as

$$c_1 = \sqrt{\gamma \cdot R_{\text{specific}} \cdot (T_e + T_{\text{ion}})} \quad (34)$$

This constitutes the system of equations that yields the values for u_k and T_k , in dependence of $T_s > T_{boiling}$, $R_{specific}$, γ and the pressure and temperature in the plasma p_{amb} , T_e, T_{ion} . This system can be solved numerically for given initial parameters $\rho_{k,0}$ and $T_{k,0}$.

The flux of particles away from the surface is finally calculated according to Eq.(9).

About the author:

First name: Marek
Middle name: Sebastian
Surname: Simon
Date of birth: March 9th, 1985
Place of birth: Munich, Germany
Nationality: German
ORCID ID: 0000-0003-2426-6754



LinkedIn:

<https://www.linkedin.com/in/marek-sebastian-simon-78716a48>



Researchgate:

<https://www.researchgate.net/profile/Marek-Simon>



